2014

The metallic thread in a patchwork thesis

Emily A. Hull
Iowa State University

The metallic thread in a patchwork thesis

by

Emily A. Hull

A dissertation submitted to the graduate faculty

in partial fulfillment of the requirements for the degree of

DOCTOR OF PHILOSOPHY

Major: Chemistry

Program of Study Committee:
Theresa L. Windus, Major Professor
Mark S. Gordon
William S. Jenks
Aaron D. Sadow
Joseph W. Burnett

Iowa State University

Ames, Iowa

2014

TABLE OF CONTENTS

CHAPTER 1: INTRODUCTION

Historical Perspectives

Any quantum chemistry textbook will begin by explaining the history and development of quantum mechanics and almost universally the first thing that is discussed is the photoelectric effect and quantization of light. One thing that is not often mentioned, though perhaps it should be, is the parallel development of photography, and photochemistry in general. Chemists had long observed that what is now called phosphorescence and fluorescence required an external light source. That is, the substance needed to absorb light from an external source before it could glow. Photosynthesis is, of course, probably the most widely used application of photochemistry. One widely-used photochemical reaction that is important to the history of science is photography.

Silver halide salts are light sensitive, reacting with light to form metallic silver. Different methods can be used to develop and then fix the latent image into a permanent image viewable by the naked eye. The first commercially viable photographic process based on silver halide salts was developed and published with the French Academy of Science by Louis Daguerre in 1839. At the time this thesis was written that communication could be viewed online.[1] Photographic methods were further improved with the introduction of the glass plate negative, improvement in photosensitive paper, introduction of photographic film etc.

While this is all very interesting for artists, it has a practical aspect as well. The discovery of radioactivity, for which Henri Becquerel, Marie Curie and Pierre Curie share the

1903 Nobel Prize in Physics, was facilitated by photography. It has long been known that photographic plates require an exposure time. Since photographic detectors (plates, paper, negatives) developed alongside camera technology, the exact exposure timing was sometimes proprietary and therefore not shared. However, a common observation made in the industry was that photographic plates wouldn't "develop" unless they were exposed to light for a certain amount of time. In other words, a quantity of light was needed to cause the reaction in the photosensitive material. It is interesting that a phenomenon so intuitively understood and widely applied, that light reacted with matter in a quantized fashion, was not fully elucidated until Einstein solved the riddle of the photoelectric effect in 1905. It is partly this feat that earned him the 1921 Nobel Prize in Physics. Photography is just one of many widely used technologies based on quantum principles.

Mathematical Basis of Quantum Mechanics

Quantum mechanics is a field of science that provides a mathematical description of physical effects that occur on a microscopic scale. It had been observed that light seems to propagate as a wave, but interacts with matter as a particle. Louis de Broglie extended this property of light to particles.[2] If light, which everyone thought was a wave, could interact as a particle, could not particles, on a very small scale, act like waves? Apparently they can. There were many brilliant people involved in formulating quantum mechanics, and many books are written on the topic.[3-7] For the purposes of this thesis, only the briefest of introductions will be provided.

There are many postulates of quantum mechanics, of which only several will be mentioned here. One of the postulates of quantum mechanics states that: "The state of a system is described by a function Ψ of the coordinates and the time. This function, called the state function or wave function, contains all the information that can be determined about the system."[5] A second postulate states that "To every physically observable property there corresponds a linear Hermitian operator…"[5] A third postulate states "The only observable values that can result from the measurements of the physically observable property Q are the eigenvalues q_i in the equation $\hat{Q}g_i=q_ig_i$, where $\hat{Q}$ is the operator corresponding to the property Q…"[5] These three postulates, and their dependence on time, are demonstrated in the time dependent Schrödinger equation.

$$i\hbar\frac{\partial}{\partial t}\Psi = \hat{H}\Psi \qquad (1)$$

where Ψ is the wave function, $\hat{H}$ is the Hamiltonian operator whose form varies depending on the physical situation being considered, $\hbar$ is Plank's constant, h, divided by 2π, and t is time. Equation (1) is the time-dependent form of the equation. When considering stationary states, the time-independent equation can be used provided the Hamiltonian isn't also dependent on time. This also, conveniently, takes the form of an eigenvalue problem.

$$\hat{H}\psi = E\psi \qquad (2)$$

where ψ is the time-independent wave function, E is energy and $\hat{H}$ is the Hamiltonian operator whose form varies depending on the situation.

In a very few situations the equation can be solved exactly, but in many others the form of the wave function is yet to be elucidated. The Hamiltonian, however, is well defined. For

chemists, who are generally interested in energy, the Hamiltonian takes the form of the total energy operator. Similar to classical physics, the energy takes two forms, potential and kinetic. The total energy Hamiltonian is, therefore, a sum of these two parts:

$$\hat{H} = \hat{T}+\hat{V} \qquad (3)$$

Where $\hat{T}$ is the kinetic energy operator (written below in one dimension, but can be n dimensional) and $\hat{V}$ is the potential energy operator.

$$\hat{T}= -\frac{\hbar^2}{2m}\frac{d}{dx^2} \qquad (4)$$

Combining equations (2), (3), and (4) this gives

$$\left[-\frac{\hbar^2}{2m}\frac{d^2}{dx^2}+\hat{V}(x)\right]\psi_i=E_i\,\psi_i \qquad (5)$$

for a single particle in one dimension. In three dimensions the differential $\frac{d^2}{dx^2}$ becomes

$$\frac{\partial^2}{\partial x^2}+\frac{\partial^2}{\partial y^2}+\frac{\partial^2}{\partial z^2}=\nabla^2 \qquad (6)$$

For a molecule, there are several interactions to consider when thinking of the form of the Hamiltonian. There are the potential energy terms for the nuclear-nuclear interactions, nuclear-electron interactions, and electron-electron interactions. Together with the kinetic energy terms, the Hamiltonian is complicated and difficult to solve. The general form of the molecular Hamiltonian is therefore[6]:

$$\hat{H}= -\sum_k\frac{\hbar^2}{2m_k}\nabla_k^2-\sum_i\frac{\hbar^2}{2m_e}\nabla_i^2-\sum_i\sum_k\frac{e^2Z_k}{r_{ik}}+\sum_{i<j}\frac{e^2}{r_{ij}}+\sum_{k<l}\frac{Z_kZ_le^2}{r_{kl}} \qquad (7)$$

Where the m_k and m_e are the masses of the nuclei and electrons respectively, $\hbar$ is Planck's constant divided by 2π, i and j run over all electrons, k and l run over all nuclei, Z is the atomic number, r_{ab} is the distance between particles a and b and e is the charge on an electron.

Obviously this is a very complicated equation. Due to the electrons' miniscule mass relative to the nuclei, the electronic motion is much faster than the nuclear motion. Therefore, as a first approximation toward solving the time independent Schrödinger equation, nuclear coordinates are fixed. This makes the nuclear kinetic energy independent from the electrons, and the nuclear-nuclear repulsion term becomes an easily calculated constant[6]. This is the Born-Oppenheimer approximation[8]. It is a very good approximation and makes the solutions much simpler. It is not applicable in all cases, however. While the approximation is perfectly valid when the ground and excited electronic states are energetically well separated, it breaks down when that energy gap narrows to the scale of the nuclear motion. Applying the approximation to the molecular Hamiltonian (7), the electronic Hamiltonian becomes:

$$\hat{H}_{el} = -\sum_i \frac{\hbar^2}{2m_e}\nabla_i^2 - \sum_i \sum_k \frac{e^2 Z_k}{r_{ik}} + \sum_{i<j} \frac{e^2}{r_{ij}} \qquad (8)$$

where the subscript el represents "electronic". Nuclear repulsion, V_{nn}, is added as a constant additive term. When substituted into to equation (2) this becomes the time-independent electronic Schrödinger equation:

$$(\hat{H}_{el} + V_{nn})\,\psi_{el} = E_{el}\psi_{el} \qquad (9)$$

While the Born-Oppenheimer approximation made life considerably simpler by removing terms and allowing a focus on the electronic wave function, there are still issues. The last term of the Hamiltonian involves electron-electron interactions. In any many body problem, the solution to

the equation becomes very complicated due to the coupling of terms, and solving by separation of variables becomes impossible and more approximations are needed.

Commonly Used Approximation Methods

There are several general types of approximation methods commonly used for solving the Schrödinger equation. There are a wide range of methods that all start with the Hartree-Fock[3,9,10] approximation. There are three kinds of Hartree Fock (HF) calculations, Restricted Hartree-Fock[11] (RHF) is for closed shell (no unpaired electrons) calculations, Restricted Open-shell Hartree Fock[12-14] (ROHF) is for open shell calculations and works best for high-spin cases, and Unrestricted Hartree-Fock[15] (UHF) which takes the open–shell species and treats the alpha and beta electrons separately. Hartree-Fock, (abbreviated in general as HF unless a specific HF method is being described) calculations can be performed independently, or they can be integrated with methods that add higher order corrections (post Hartree-Fock methods). Examples of higher order methods are Perturbation Theory which could be Møller-Plesset perturbation theory[6,16-20] (MPn where n is the level of correction) or the more general Many-Body Perturbation Theory[21-23] (MBPT), Coupled Cluster[4,6,23-25] (CC), and Configuration Interaction[4-6,17,26] (CI), which could be full-CI or one of the methods that truncates the CI expansion such as CI-singles and doubles, (CISD) or CI-singles, doubles and triples (CISDT) and so on. Another general approximation method is Density Functional Theory[27-30] (DFT) which seeks to solve a density functional based on the theory that everything chemically interesting can be elucidated from the probability density. DFT can be conventional[27,31] or time-dependent[30,32-37] DFT (TDDFT) for excited states. In all of these approximations (with the

exception of a few DFT methods), orbitals are described by a linear combination of atomic orbitals which themselves are built out of basis functions.

Basis Sets

In most wave function based models, molecular orbitals are constructed from a linear combination of individual atomic orbitals. Those atomic orbitals, in turn, are modeled by basis functions. The set of basis functions used to model a particular atom or molecule is a basis set. Functions are used to model 1s, 2s, 2p etc. atomic orbitals by using, for example, Slater or Gaussian functions. While Slater orbitals do a better job of correctly modeling atomic orbitals, such as the cusp at the nucleus for 1s orbitals, their form makes them difficult to use for large calculations. Slater functions have the general form:

Slater Function: $S(r) = Ne^{-\alpha r}$

where N is a normalization constant, r is the radial distance of the electron to the nucleus and α is a constant related to the size of the orbital.

On the other hand, since the product of two Gaussian functions is another Gaussian function, Gaussians are much easier to work with. Multiple Gaussian functions can be used to approximate a single Slater function with more computational efficiency than using the actual Slater function. While advances in computer hardware makes this less important now than in the past, Gaussian basis sets are the dominant basis sets used in computational chemistry. The general form of a Gaussian function is:

Gaussian Function: $G(r) = Ne^{-\alpha r^2}$

where N is a normalization constant, r is the radial distance of the electron to the nucleus and α is a constant related to the size of the orbital.

A minimal basis set is one that uses a single function for each orbital. That means a single function, or linear combination of functions contracted into a single function, is used to describe each of the 1s, 2s, 2p…, orbitals. Carbon, for instance, would have 5 basis functions for the 1s, 2s, and 2p (p_x, p_y and p_z) orbitals. In a molecular calculation this generates molecular orbitals for each of the core, filled valence, and corresponding virtual valence (unfilled) spaces.

The more functions that are used to model each atomic or molecular orbital, either Slater type or combinations of primitive Gaussian functions, the better the wave function is approximated. Additionally, diffuse and polarization functions can be added. Polarization adds a function of the next higher angular momentum, so a hydrogen atom would get a p-function, carbon would get a d-function and so on. Adding a polarization function allows, for example, a symmetric s orbital to deform asymmetrically in the presence of another body where deformation is essential to the formation of chemical bonds. Diffuse functions are added to better approximate the tail of the Gaussian and are important for systems with longer-range interactions. A more detailed discussion of Gaussian basis sets can be found in any computational chemistry textbook[4-6] and the literature[38].

It is also noted that the core orbitals, while adding a great deal to the overall energy term of a molecule, don't necessarily add significantly to the valence electron interactions. In heavy elements, however, such as third row transition metals, core orbitals also contribute to relativistic effects[39] due to the non-zero probability of finding the 1s electrons at the nucleus. This has led to the development of pseudopotential methods where the core orbitals are treated as a single

potential. This greatly simplifies the overall calculation as a single potential is used to represent, for example, the orbitals containing maybe 10 electrons (in the case of iron). Pseudopotential basis sets also have the added advantage of often including relativistic effects that can significantly affect the overall energy and properties of a heavy element system. A good review of pseuopotential basis sets and their use in computational chemistry can be found in computational chemistry textbooks[4-6], or the literature[38,40].

Hartree-Fock

For molecular systems, the Hartree-Fock (HF) approximation assumes the Born-Oppenheimer approximation and the electronic Schrödinger equation, (9), is solved by approximating the wave function as a Slater determinant, D.

$$E_{HF} = \langle D | \hat{H}_{el} + V_{nn} | D \rangle \qquad (10)$$

The equation is variationally optimized to obtain those orbitals that minimize the energy. Because Hartree-Fock is a variational method, this energy is guaranteed to be higher than the true energy of the system. Electron-electron exchange and same-spin electron correlation are accounted for in Hartree-Fock, but not opposite spin electron correlation. Neglecting the latter means that the Hartree-Fock wavefunction is often used as the zeroth-order wavefunction in post-Hartree-Fock methods.

Despite being a low-level approximation, Hartree-Fock is still useful. Hartree-Fock calculations simulate the vast majority of the energy for a given molecule - perhaps 95%. Hartree-Fock does not take into account relativistic effects (generally) so there can potentially be

problems in using this method in systems containing heavy elements. HF still does a surprisingly good job with geometries. Depending on the level of accuracy desired one might, for instance, optimize a geometry with a quick HF calculation and then use a higher order method just for energy corrections. A more detailed derivation of the method and its extensions can be found in computational chemistry textbooks[3-6,12], and the literature[9,11,13-15].

Electron Correlation

The correlation energy is defined as the energy difference between the true non-relativistic energy of the system minus the contribution from Hartree-Fock with a complete basis set. Correlation energy is generally split into two flavors, static and dynamic. The energy gained by allowing partial occupation of orbitals to better model the quasi-degenerate states is referred to as static or non-dynamical correlation energy[41]. The energy recovered by considering the instantaneous correlation of the electrons (usually obtained by allowing electrons to move between occupied and virtual orbitals) is referred to as dynamical correlation energy.

A multiconfigurational wavefunction, as the name suggests, uses more than one state or configuration to describe a system. There are many systems where a multiconfigurational wavefunction is more qualitatively correct than a single reference (single-state) wavefunction. A qualitatively correct wavefunction for methylene, CH_2, at any bond angle must contain both the singlet bent and triplet linear configurations[41] Many unsaturated transition metal species and molecules with significant diradical character are better modeled by using multi-configurational methods. However these methods are computationally expensive and are, therefore, less frequently used.

Occupied and Virtual Orbitals

Orbitals are constructed mathematically using a combination of basis functions, as previously explained. While the number of electrons determines the number of occupied orbitals, the more complete the basis set the larger the number of unoccupied or virtual orbitals. These virtual orbitals from Hartree-Fock do not necessarily represent the lowest unoccupied molecular orbital (LUMO) or unoccupied orbitals of simple molecular orbital theory. An infinitely large basis set would produce an infinite continuum of states.

Molecular orbitals, in general, and virtual orbitals, in particular, are essentially a mathematical construct. Dealing in probability, as quantum chemists do, it is difficult to definitively say that a particular effect is a direct result of a single electron interaction with a particular orbital. However, molecular orbitals as a whole do seem to have physicality and help to provide an interpretation of chemical processes. Interactions between occupied and low-lying virtual states lead to a multitude of physical effects. The interactions can be stimulated, such as the process leading to LASER light emission, or they can be more indirect, such as sunlight exciting electrons in the large hydrocarbons in a carrot, which our eyes detect as the color orange.

Multi-Configurational Self-Consistent Field

In Multi-Configurational SCF[41-50] (MCSCF), the orbitals are partitioned into core, active, and virtual orbitals. Those orbitals expected to remain both doubly occupied and relatively

unchanged through the course of a reaction are assigned to the core. A complete active space[44,45,50] (CAS-SCF) would contain those orbitals which are (or could be) partially occupied during a reaction, or that represent any bond breaking or forming in the course of a reaction and their counterpart virtual or antibonding orbitals. Other unoccupied orbitals are assigned to the unoccupied virtual space. The active space orbitals are treated by a CI method where not only the CI coefficients, but also the molecular orbitals are optimized.

This has the effect of recovering the non-dynamical correlation energy of a chemical system. The larger the active space in MCSCF, the closer the calculations come to FCI and the more the distinction between static and dynamic correlation blurs. MCSCF, therefore, provides a good qualitative wave function, but the amount of correlation energy recovered depends on the size of the active space. While there is a substantial energy correction by modeling the non-dynamical correlation energy with this method, another energy correction is usually needed for the dynamical correlation. MCSCF is, therefore, often the starting calculation whose wavefunction is used as the zeroth-order wavefunction for other methods. A basic introduction to MCSCF can be found in computational chemistry textbooks[3-6], but a more detailed review by Gordon and Schmidt can be found in the literature[41].

ORMAS

In developing a Slater determinant based direct CI approach, Ruedenberg and Ivanic[51,52] found that approximately 50% of configurations in CISD were non-significant contributors to the energy. The picture was worse for CISDT and CISDTQ with some 90% of configurations being non-significant deadwood[52]. Considering this problem of deadwood, Occupationally Restricted

Multiple Active Space (ORMAS) seeks to eliminate non-significant configurations by partitioning the system into multiple small active spaces with limited electron occupations. In considering a system with several bonding regions, one could separate each bonding region into a unique active space.

As an example, consider the orbitals in CO. Considering only the 2p orbitals of carbon and oxygen, the active space would consist of a set of carbon-oxygen sigma bonding and anti-bonding orbitals, and 2 sets of carbon-oxygen pi bonding and anti-bonding pairs, for a total of 6 orbitals and 6 electrons. Within this active space there is a theoretical probability for any electron from the occupied orbitals to interact with any of the virtual orbitals. Even though all of these excitations are possible, many of them contribute very little to the overall system energy. Using ORMAS, one breaks up the MCSCF active space into multiple active spaces that contain the excitations that contribute the most to the overall energy. Depending on the chemistry one is examining, one could partition the active space for CO by creating two active spaces, one for the sigma bonding and anti-bonding orbitals and another for the pi bonding and antibonding orbitals. In other words a 2x2 (2 electrons in 2 orbitals) space for the sigma bonding and anti bonding and a 4x4 space for the pi bonding and antibonding. This captures the most important sigma-sigma* and pi-pi* transitions but eliminates any sigma-pi* or pi-sigma* transitions.

In another example, if the system consists of two molecules separated by a distance, a benzene dimer for instance, each benzene monomer can have its own active space (or multiple active spaces) rather than using a single active space for the entire system. In this way, ORMAS can be viewed as a potential, if limited, fragmentation method. If the entire active space and the entire virtual space are set as two spaces, then excitations between these spaces is equivalent to

CIS, CISD, CISDT etc. depending on how many electrons are allowed to interact between the spaces. For atomic calculations, one can make separate active spaces for the s, p, d etc. valence orbitals and thereby set the electronic configuration in the calculation. This makes ORMAS a very useful tool for many different applications.

Post Hartree-Fock Methods

Those methods that attempt to recover correlation energy (more specifically dynamic correlation energy) are often termed post Hartree-Fock methods. These methods are those based directly on the HF formalism and usually use the HF or MCSCF solution as the zeroth-order approximation to which corrections are added.

Configuration Interaction (CI)

Full Configuration Interaction (Full-CI) is conceptually simple but practically impossible for large molecular systems with a large basis set. The electronic wave function is approximated by a linear expansion of Slater determinants.[26]

When all possible configurations of the N electrons in the full set of orbitals are considered, it is called Full-CI (FCI). With a sufficiently large basis set, FCI should give the true non-relativistic energy of the system and recover all the electron correlation energy. While improvements in hardware and changes in computing methods (such as replacing the traditional configuration state functions with Slater determinants) have increased the utilizability of FCI, it is still limited to very small systems.

To this end, methods have been developed to recover most of the correlation energy of FCI, but at reduced computational cost. This is done by realizing that every possible configuration of electrons in all molecular orbitals can be broken down into excitations of electrons from the reference determinant(s) (HF for example) and sequentially excited to higher orders of excitations (single, double, triple, quadruple etc. excitations) in the form:

$$|\psi\rangle = c_0|\Phi_0\rangle + \sum_{ia} c_i^a|\Phi_i^a\rangle + \sum_{a<b,i<k} c_{ij}^{ab}|\Phi_{ij}^{ab}\rangle + \sum_{a<b<c,i<j<k} c_{ijk}^{abc}|\Phi_{ijk}^{abc}\rangle + .. \quad (11)$$

Where the c's are the variationally optimized CI coefficient, Φ_0 is the reference wavefunction (HF or MCSCF as discussed above), and Φ_i^a , in the formulation presented, is a configuration state function created when the electron in occupied orbital i is excited to an unoccupied orbital a. For higher order excitations, occupied orbitals ij are excited to unoccupied ab (doubles excitation), or ijk to abc (triples excitation) and so on. CI singles and doubles excitations, CISD, recovers around 90% of the correlation energy of FCI, CISDT (including triples excitations) 95% and CISDTQ (including quadruples excitations) 98% for most systems[26,51,52]. While CI methods are introduced in computational chemistry textbooks previously referenced, the review article by Sherrill and Shaefer[26] is invaluable for gaining a good understanding of the method.

Perturbation Theory

Perturbation methods[3,16,18,20] add a perturbation factor to correct the Hartree-Fock or MCSCF wavefunction. The degree of perturbation, meaning the level of correction, is specified as MBPT2 or MP2 for a second order correction, MBPT4 or MP4 for a fourth order correction and so forth depending on the exact methodology used in applying the perturbation.

Generally speaking, the perturbation method is based on the following equations

$$\hat{H}=\hat{H}_o+\lambda\hat{H}' \quad (12)$$

where $\hat{H}_0$ is the sum of the one-electron Fock operators (the unperturbed Hamiltonian), λ is a perturbation parameter, $\hat{H}$ is the correct Hamiltonian for the perturbed system, which leaves $\hat{H}'$as the perturbation, the difference between the perturbed and unperturbed Hamiltonians.

The Hamiltonian depends on the perturbation parameter λ and therefore the wavefunction and energy do as well. When equation (12) is applied to the zeroth order HF wave function (ψ_0) in the electronic Schrödinger equation, (9), the following expansion is created:

$$\psi=\psi_0+\sum_{i=1}^{n}\lambda^i\psi_i \quad (13)$$

and

$$E=E_0+\sum_{i=1}^{n}\lambda^i E_i \quad (14)$$

where the sum *i* to *n* is the degree of the perturbation correction, so *n*=2 is the second order correction and so forth. Like terms of λ can then be collected from the expansion and equated to gain each of the energy and wavefunction corrections. This is a very general form of the perturbation theory approach, and the reader is referred to several good textbooks and references for more detail.[3,6,16-18,20-23]

Perturbation theory is non-variational so the energy from the perturbations is not necessarily guaranteed to be higher in energy than the true ground state. Higher order corrections, while much more expensive than a second order correction, are not guaranteed to

produce better results[20]. This is in direct contrast to CI based methods where including higher order excitations is a guarantee of improved results, though those results might not be enough to justify the increased computational cost.

When perturbation theory is applied to the MCSCF wavefunction, it is called Multi-Reference Perturbation Theory[53-56]. There are many abbreviations for this depending on the way the perturbation is applied, MR-MP2, MR-PT2 etc. This method is very useful for recovering the dynamical correlation energy of an MCSCF system. Because the MCSCF is solved first, there are real limits to the size of system that can be treated in this manner.

Density Functional Theory (DFT)

In 1964, Pierre Hohenberg and Walter Kohn proved that the ground state molecular energy and all other molecular electronic properties can be determined by the ground-state electronic probability density[27]. This theory was further developed and, in 1965, the Kohn-Sham (KS) formalism of Density Functional Theory (DFT) was born.[31] By utilizing a model, fictitious, system of non-interacting electrons (the ideal electron gas), the method was argued to be analogous to HF and a series of self-consistent equations was presented to solve for the energy and KS orbitals which are the density functional version of molecular orbitals. DFT has become a major method in chemistry, physics and materials science and anyone interested in learning more is referred to one of the many books or review articles written on the subject[4-6,27-29,31,33]. One important thing to note is that DFT is not formally a wavefunction method and is therefore not technically a solution to the Schrödinger equation.

In its most simplified form the DFT ground state energy can be written as a sum of several terms

$$E=T_s+U+V_{nuc}+E_{xc} \quad (15)$$

The energy of the Kohn-Sham orbitals is represented by T_s, the Hartree energy (Coulomb energy) is represented by U and includes the nuclear-nuclear terms, V_{nuc} is the electron-nuclear attraction and E_{xc} is the energy obtained from the exchange correlation functional.

While T_s, U, and V_{nuc} all have derivable and well understood forms, the exchange-correlation functional does not. In fact, because all of the other pieces are well known or relatively easily derived, the E_{xc}, necessarily contains anything else that would be needed to make the sum equal to the exact ground state energy. According to the KS theorem, if E_{xc} is known as a functional of the density, then a closed set of equations exists to solve the electronic structure problem. Unfortunately E_{xc} is not known, and not necessarily derivable, which means there is no systematic improvability for DFT. Many exchange correlation functionals have been developed with varying degrees of success depending on the system for which they were developed. DFT is a large field and a vast amount of literature exists[4-6,19,27-29,31] for better understanding the numerous different functionals, their design, their successes and their failures[33].

There is considerable debate about the nature of DFT, whether it is a truly "first principle", semi-empirical or approximation method. Despite the controversy, and due in no small part to its computational efficiency for large systems, DFT has become the dominant method for calculations involving large systems, systems containing heavy elements, and even many problems in materials science and solid state physics. If we think of computational

chemistry as a tool box with each method being a tool, DFT has shown itself to be a useful tool when used properly.

Time-Dependent Density Functional Theory (TDDFT)

Time-Dependent Density Functional Theory[30,32,34-37] (TDDFT) is an excited state method based on DFT. Within the framework of Hartree-Fock and post Hartree-Fock methods, there is CIS, configuration interaction singles [equation (11)], which allows single excitations from the ground state. TD-HF (Time Dependent Hartree-Fock) with the Tamm-Dancoff[32] approximation is the same as CIS for all practical purposes. While CIS is useful for qualitatively describing excited states and obtaining such properties as vertical excitation energies[6], because it only includes single excitations, it fails to recover much of the correlation energy and is especially bad at predicting the energies of the lowest excited state. Regular DFT was formulated as a ground state method. TDDFT takes that ground state method and extends it to excited states. To do this TDDFT adds linear response equations to the exchange-correlation functional. These equations can be very complicated and the reader is referred to the literature[30,32,34] on the topic for additional information. Since TDDFT, being based on DFT, recovers some correlation energy it generally both qualitatively models the excited states and predicts their energies relatively well compared to experiments. This makes TDDFT useful for modeling optical activity[57], but it does poorly with charge-transfer and charge-resonance interactions.[57-59]

Transition Metal Chemistry

From the point of view of computational chemistry, metals present some special challenges. The first challenge is simply their size. Computational chemistry calculates interactions with electrons, and metals have many more electrons than carbon, oxygen or nitrogen, for example. Transition metals also have more electronic state degeneracy. In small atoms, like carbon, there is enough energy separation between the ground and first excited states that in most circumstances only the ground state requires consideration. This is not necessarily true for transition metals. For many transition metal species relativistic effects also play a role in the chemistry of the system.[39] After taking all of these things into consideration it is understandable that a person would shy away from doing calculations of transition metal species.

After many pages of complex discussion and mathematical equations it is only appropriate to take a break and consider the bigger picture. At the beginning of this lengthy discussion, photochemistry, specifically the art of photography and the photoelectric effect were mentioned. Both of these involve metals. While life is based on organic chemistry, the chemistry of carbon, oxygen, nitrogen and a few other atoms at the top right of the periodic table, life would be incomplete without color. Transition metals give us color. The chemistry of metals is integral to the function of metalloproteins[60-63] which are in turn essential for life. On a more tactile level, metals are the basis of currency and jewelry, and, from the earliest days, mankind has used metal containing pigments to create fine works of art.[64-66] For chemists transition metal species also play an integral role as catalysts, doping agents for semi-conductors, and materials for magnets[67]. On a cost-benefit analysis, while metal species are more difficult to model, the rewards for doing so correctly seem to outweigh the inherent difficulties.

Dissertation Organization

This thesis contains research that is being prepared for publication. Chapter 2 presents research on water and THF solvated macrocyclic Rh and Co compounds and the effects of different axial ligands (NO_2, NO, Cl, CH_3) on their optical activity. Chapter 3 involves the study of gas-phase Nb mono and dications with CO and CO_2. Chapter 4 is a study of reactions of CO and CO_2 with Ta mono and dications. Chapter 5 is a study on virtual orbitals, their usefulness, the use of basis sets in modeling them, and the inclusion of transition metals into the QUasi Atomic Minimal Basis (QUAMBO) method.[68-72] Chapter 6 presents the conclusions drawn from the work presented in this dissertation.

References

(1) Daguerre, L. In *Comptes rendus hebdomadaires des séances de l'Académie des sciences / publiés... par MM. les* 1835-1965 ed.; (Paris), G.-V., Ed.; Académie des sciences (France): Paris, France, 1839.

(2) L. de Broglie, University of Paris, 1924.

(3) Szabo, A.; Ostlund, N. S. *Modern Quantum Chemistry*; Dover Publishing: Mineola, New York, 1996.

(4) Jensen, F. *Introduction to Computational Chemistry* **1999**.

(5) Levine, I. N. *Quantum Chemistry*; 5th ed.; Prentice Hall: Upper Saddle River, NJ, 2000.

(6) Cramer, C. J. *Essentials of Computational Chemistry Theories and Models*; Second ed.; Chichester: John Wiley & Sons, Ltd: Chichester, 2006.

(7) Jammer, M. *The Philosophy of Quantum Mechanics: The Interpretations of Quantum Mechanics in Historical Perspective*; Wiley, 1974.

(8) Born, M.; Oppenheimer, R. *Annalen der Physik* **1927**, *389*, 457.

(9) Plakhutin, B. N. *Journal of Mathematical Chemistry* **1997**, *22*, 203.

(10) Glaesemann, K. R.; Schmidt, M. W. *J. Phys. Chem. A* **2010**, *114*, 8772.

(11) Roothaan, C. C. J. *Reviews of Modern Physics* **1951**, *23*, 69.

(12) Carbo, R.; Riera, J. In *A General SCF Theory*; Springer Berlin Heidelberg: 1978; Vol. 5, p 1.

(13) Glaesemann, K. R.; Schmidt, M. W. *The Journal of Physical Chemistry A* **2010**, *114*, 8772.

(14) Roothaan, C. C. J. *Reviews of Modern Physics* **1960**, *32*, 179.

(15) Pople, J. A.; Nesbet, R. K. *The Journal of Chemical Physics* **1954**, *22*, 571.

(16) Møller, C.; Plesset, M. S. *Physical Review* **1934**, *46*, 618.

(17) Handy, N. C.; Schaefer, H. F. *The Journal of Chemical Physics* **1984**, *81*, 5031.

(18) Head-Gordon, M.; Pople, J. A.; Frisch, M. J. *Chemical Physics Letters* **1988**, *153*, 503.

(19) Wiberg, K. B.; Hadad, C. M.; LePage, T. J.; Breneman, C. M.; Frisch, M. J. *The Journal of Physical Chemistry* **1992**, *96*, 671.

(20) Leininger, M. L.; Allen, W. D.; Schaefer, H. F.; Sherrill, C. D. *The Journal of Chemical Physics* **2000**, *112*, 9213.

(21) Hirata, S.; He, X.; Hermes, M. R.; Willow, S. Y. *The Journal of Physical Chemistry A* **2013**, *118*, 655.

(22) Bartlett, R. J. *Annual Review of Physical Chemistry* **1981**, *32*, 359.

(23) Shavitt, I.; Bartlett, R. J. *Many-Body Methods in Chemistry and Physics: MBPT and Coupled-Cluster Theory*; University Press: Cambridge 2009.

(24) Čížek, J. *The Journal of Chemical Physics* **1966**, *45*, 4256.

(25) Crawford, T. D.; Schaefer, H. F. In *Reviews in Computational Chemistry*; John Wiley & Sons, Inc.: 2007, p 33.

(26) Sherrill, C.; Schaefer, H. I. *Advances in Quantum Chemistry* **1999**, *34*, 143.

(27) Hohenberg, P.; Kohn, W. *Physical Review* **1964**, *136*, B864.

(28) Levy, M. *Proceedings of the National Academy of Sciences* **1979**, *76*, 6062.

(29) Vignale, G.; Rasolt, M. *Physical Review Letters* **1987**, *59*, 2360.

(30) Casida, M. E. *Journal of Molecular Structure: THEOCHEM* **2009**, *914*, 3.

(31) Kohn, W.; Sham, L. J. *Physical Review* **1965**, *140*, A1133.

(32) Hirata, S.; Head-Gordon, M. *Chemical Physics Letters* **1999**, *314*, 291.

(33) Burke, K. *The Journal of Chemical Physics* **2012**, *136*.

(34) Casida, M. E.; Huix-Rotllant, M. *Annual Review of Physical Chemistry* **2012**, *63*, 287.

(35) Runge, E.; Gross, E. K. U. *Phys. Rev. Lett* **1984**, *52*.

(36) Gross, E. K. U.; Kohn, W. *Adv. Quantum Chem* **1990**, *21*.

(37) Petersilka, M.; Gossman, U. J.; Gross, E. K. U. *Phys. Rev. Lett* **1996**, *76*.

(38) Peterson, K. A. *Annual Reports in Computational Chemistry* **2007**, *3*, 195.

(39) Pyykkö, P. *Annual Review of Physical Chemistry* **2012**, *63*, 45.

(40) Cundari, T. R.; Benson, M. T.; Lutz, M. L.; Sommerer, S. O. In *Reviews in Computational Chemistry*; John Wiley & Sons, Inc.: 2007, p 145.

(41) Schmidt, M. W.; Gordon, M. S. *Annual Review of Physical Chemistry* **1998**, *49*, 233.

(42) Cheung LM, S. K., Ruedenberg K *J. Am. Chem. Soc.* **1978**, *100*, 8024.

(43) Cheung LM; Sundberg KR; K, R. *Int. J. Quantum Chem* **1979**, *16*, 1103.

(44) Roos BO, T. P., Siegbahn PEM. *Chem. Phys.* **1980**, *48*, 157.

(45) Siegbahn PEM, A. f. J., Heiberg A, Roos BO *J. Chem. Phys.* **1981**, *74*, 2384.

(46) Feller DF, S. M., Ruedenberg K. *J. Am. Chem. Soc.* **1982**, *104*, 960.

(47) K, R.; MW, S.; Gilbert MM, E. S. *Chem. Phys.* **1982**, *71*, 65.

(48) Ruedenberg K, S. M., Gilbert MM, Elbert ST *Chem. Phys.* **1982**, *71*, 41.

(49) Ruedenberg K, S. M., Gilbert MM *Chem. Phys.* **1982**, *71*, 51.

(50) BO, R. *Adv. Chem. Phys.* **1987**, *69*, 399.

(51) Ivanic, J.; Ruedenber, K. *Theoretical Chemistry Accounts* **2001**, *106*, 339.

(52) Ivanic, J.; Ruedenber, K. *Theoretical Chemistry Accounts* **2002**, *107*, 220.

(53) Andersson K, M. P.-A., Roos BO, Sadlej AJ, Wolinksi K. *J. Phys. Chem. A* **1990**, *94*, 5482.

(54) Andersson K, M. P.-A., Roos BO. *J. Chem. Phys.* **1992**, *96*, 1218.

(55) K., A. *Theor. Chim. Acta* **1995**, *91*, 31.

(56) H-J., W. *Mol. Phys.* **1996**, *89*, 645.

(57) Fabian, J. *Theoretical Chemistry Accounts* **2001**, *106*, 199.

(58) Casida, M. E.; Gutierrez, F.; Guan, J.; Gadea, F.-X.; Salahub, D.; Daudey, J.-P. *The Journal of Chemical Physics* **2000**, *113*, 7062.

(59) Fabian, J.; Diaz, L. A.; Seifert, G.; Niehaus, T. *Journal of Molecular Structure: THEOCHEM* **2002**, *594*, 41.

(60) Pickett, C. J.; Vincent, K. A.; Ibrahim, S. K.; Gormal, C. A.; Smith, B. E.; Fairhurst, S. A.; Best, S. P. *Chem. Eur. J.* **2004**, *10*, 4770.

(61) Spreitzer, R. J. *Annual Rev. Plant Physiol. Plant Mol. Biol.* **1993**, *44*, 411.

(62) Heo, J. S., C. R.; Ludden, P. W. *Biochemistry* **2001**, *40*, 7604.

(63) Oliva, M.; Safont, V. S.; Andre´s, J.; Tapia, O. *Journal of Physical Chemistry A* **2001**, *105*, 9243.

(64) Hradil, D.; Grygar, T.; Hradilová, J.; Bezdička, P. *Applied Clay Science* **2003**, *22*, 223.

(65) Colomban, P. *Journal of Nano Research* **2009**, *8*, 109.

(66) Dik, J.; Janssens, K.; Van Der Snickt, G.; van der Loeff, L.; Rickers, K.; Cotte, M. *Analytical Chemistry* **2008**, *80*, 6436.

(67) Miessler, G. L.; Tarr, D. A. *Inorganic Chemistry*; Fourth ed.; Prentice Hall, 2010.

(68) Lu, W. C.; Wang, C. Z.; Schmidt, M. W.; Bytautas, L.; Ho, K. M.; Ruedenberg, K. *The Journal of Chemical Physics* **2004**, *120*, 2638.

(69) Lu, W. C.; Wang, C. Z.; Schmidt, M. W.; Bytautas, L.; Ho, K. M.; Ruedenberg, K. *The Journal of Chemical Physics* **2004**, *120*, 2629.

(70) Ivanic, J.; Atchity, G.; Ruedenberg, K. *Theor Chem Acc* **2008**, *120*, 281.

(71) Ivanic, J.; Ruedenberg, K. *Theor Chem Acc* **2008**, *120*, 295.

(72) West, A. C.; Schmidt, M. W.; Gordon, M. S.; Ruedenberg, K. *The Journal of Chemical Physics* **2013**, *139*.

CHAPTER 2: UV-VISIBLE SPECTROSCOPY OF MACROCYCLIC NITROSYL COMPLEXES OF COBALT AND RHODIUM. EXPERIMENT AND CALCULATION

Emily A. Hull, Aaron C. West, Oleg Pestovsky, Kathleen E. Kristian, Arkady Ellern, James F. Dunne, Jack M. Carraher, Andreja Bakac* and Theresa L. Windus*

Department of Chemistry and Ames Laboratory, Iowa State University, Ames, Iowa 50011

Abstract

Transition metal complexes $(NH_3)_5CoX^{2+}$ (X = CH_3, Cl) and $L(H_2O)MX^{2+}$, where M = Rh or Co, X = CH_3, NO, or Cl, and L is a macrocyclic N_4 ligand are examined by both experiment and computation to better understand their electronic spectra and associated photochemistry. Specifically, irradiation into weak visible bands of nitrosyl and alkyl complexes $(NH_3)_5CoCH_3^{2+}$ and $L(H_2O)M^{III}X^{2+}$ (X = CH_3 or NO) leads to photohomolysis that generates the divalent metal complex and $^{\bullet}CH_3$ or $^{\bullet}NO$, respectively. On the other hand, when X = halide or NO_2, visible light photolysis leads to dissociation of X^- and/or cis/trans isomerization. Computations show that visible bands for alkyl and nitrosyl complexes involve transitions from M-X bonding orbitals and/or metal d orbitals to M-X antibonding orbitals. In contrast, complexes with X = Cl or NO_2 exhibit only d-d bands in the visible, so that homolytic cleavage of the M-X bond requires UV photolysis. UV-Vis spectra are not significantly dependent on the structure of the

equatorial ligands, as shown by similar spectral features for $(NH_3)_5CoCH_3^{2+}$ and $L^1(H_2O)CoCH_3^{2+}$. Submitted to Dalton Transactions.

Introduction

Recently, we prepared a macrocyclic nitrosyl rhodium complex $L^2(H_2O)Rh(NO)^{2+}$ (L^2 = *meso*-Me_6-[14]aneN_4) with unique chemical and photochemical properties that make it an excellent photochemical precursor of •NO, see Figure 1 (M = Rh, X = NO).[1] [Here and throughout the paper, M is a metal and X is an axial ligand]. The complex is highly soluble in water, thermally stable and resistant toward O_2.[1] The visible spectrum exhibits a weak band (ε = 45 M^{-1} cm^{-1}) at 650 nm. The photolysis at 650 nm cleaves the Rh-NO bond to generate $L^2(H_2O)Rh^{2+}$ and •NO with a quantum yield of unity.[1] The efficient photohomolysis rules out the assignment of this band as a ligand-field transition which would also appear unlikely on the grounds that such transitions in heavy metal complexes normally occur at much shorter wavelengths.[2]

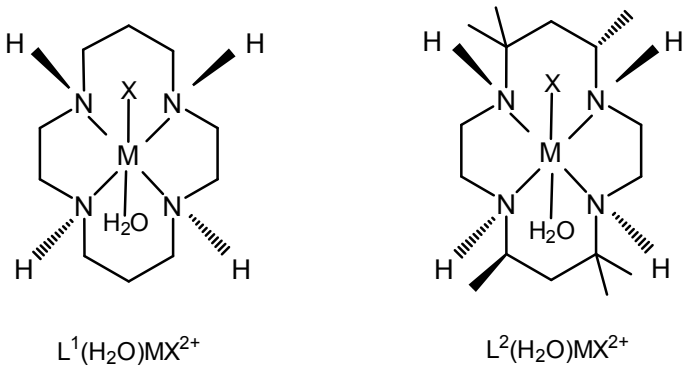

$L^1(H_2O)MX^{2+}$ $L^2(H_2O)MX^{2+}$

Figure 1. Structures of the $L^1(H_2O)MX^{2+}$ (left) and $L^2(H_2O)MX^{2+}$ (right). M is a metal and X is an axial ligand.

In a related case, photochemical excitation of the weakly absorbing $L^1(H_2O)Co(CH_3)^{2+}$ (L^1 = [14]aneN$_4$ as shown in Figure 1) at 478 nm leads to cleavage of the cobalt-carbon bond to yield $L^1(H_2O)Co^{2+}$ and methyl radicals with $\Phi_{478} = 0.3$.[3] The formally related family of complexes, $Co(NH_3)_5X^{2+}$ (X = Cl, Br, I) yield exclusively hydrolysis products, i. e. X^- and $Co(NH_3)_5(H_2O)^{3+}$ under comparable conditions. The homolysis to $Co(NH_3)_5^{2+}$ and X· requires much shorter wavelengths. Similarly, the visible light photolysis of $Rh(NH_3)_5X^{2+}$ complexes[4,5] yields only aquation products, X^- and NH_3, but no X·. The contrasting photochemical behaviors of $L^1(H_2O)CoCH_3^{2+}$ and $Co(NH_3)_5X^{2+}$ were rationalized by invoking the low electron affinity of CH_3[3,6] and large value of the exchange integral for the alkyl complex. Therefore, the 478-nm transition was tentatively assigned[3] as $\Psi_{NB} \rightarrow d_{x^2-y^2}$ rather than a d-d band which would correspond to (d_{xz}, d_{yz}, or d_{xy}) $\rightarrow d_{z^2}$.

In order to gain better insight into the electronic structures and UV-visible spectra of $L^2(H_2O)Rh(NO)^{2+}$ and related complexes, we performed time dependent density functional theory (TDDFT) calculations on several nitrosyl and alkyl complexes of cobalt and rhodium. For comparison, we also examined macrocyclic nitro and hydrido rhodium complexes, as well as $Co(NH_3)_5Cl^{2+}$ and $Co(NH_3)_5CH_3^{2+}$. The latter lacks the macrocyclic ligand but is structurally and electronically closely related to $L^1(H_2O)CoCH_3^{2+}$. If the low electron affinity of CH_3[3,6] is indeed critical for homolysis of $L^1(H_2O)CoCH_3^{2+}$ by visible light, then $Co(NH_3)_5CH_3^{2+}$ should depart from the pattern established for $Co(NH_3)_5X^{2+}$ series (X = Cl, Br, I) and undergo homolytic Co-C bond cleavage. The results are reported herein.

Materials and Methods

Experimental

Preparation and crystal structure of trans-[$L^2Rh(NO_2)_2$]ClO_4. *trans*-[L^2RhCl_2]Cl (0.15 g, 3.5×10^{-4} mol) and $NaNO_2$ (0.70 g, 1.0×10^{-2} mol) were suspended in 25 mL water in a 50 mL round bottom flask. The suspension was refluxed for 20 hours. After cooling to room temperature and the addition of 3 mL of 70% $HClO_4$, a crude white product precipitated. The solid was isolated by filtration, washed with 3 × 5 mL portions of cold water, and re-suspended in 50 mL of water. The suspension was heated until all of the solid dissolved. Slow cooling gave an off-white product. The process was repeated 2 more times to give the pure white product in 25% yield (0.045 g, 8.6×10^{-5} mol). X-ray quality crystals were obtained by slow evaporation of the solvent.

A crystal suitable for X-ray analysis was selected under the microscope and covered with PARATONE oil. Crystal evaluation and data collection were performed on a Bruker Apex II diffractometer with Mo K_α ($\lambda = 0.71073$ Å, graphite monochromator) radiation and a detector-to-crystal distance of 5.03 cm. Three series of ω scans at different starting angles were obtained to analyze the reflection profiles and to estimate the exposure time for data collection. Each series consisted of 30 frames collected at intervals of 0.3º in a 10º range about ω with an exposure time of 10-40 seconds per frame. Data were obtained using a full sphere routine by harvesting four sets of frames with 0.3º scans in ω with an exposure time of 10 seconds per frame. The dataset was corrected for Lorentz and polarization effects. The absorption correction was based on fitting a function to the empirical transmission surface as sampled by multiple equivalent measurements.[7]

The positions of almost all non-hydrogen atoms were found by direct methods. The remaining atoms were located in an alternating series of least-squares cycles and difference Fourier maps. All non-hydrogen atoms were refined in a full-matrix anisotropic approximation. Distances and thermal displacement coefficients of perchlorate anion were restrained to obtain realistically symmetric geometry. Hydrogen atoms were placed in the structure factor calculation at idealized positions and were allowed to ride on the neighboring atoms with relative isotropic displacement coefficients. All calculations were performed with Bruker Apex II Software Suite.[8]

The crystal structure of $[L^2Rh(NO_2)_2]^+$ is depicted in Figure 2. Half of the Rh complex and a perchlorate anion disordered by inversion center were found in an asymmetric unit of triclinic cell. All relevant information is summarized in Table S1. Also, CCDC 1015594 contains the supplementary crystallographic data and can be obtained free of charge from The Cambridge Crystallographic Data Centre via www.ccdc.cam.ac.uk/data_request/cif.

Aqueous solutions of $L^1(H_2O)Rh(NO)^{2+}$ were obtained by passing gaseous $^{\bullet}NO$ through solutions of $L^1(H_2O)Rh^{2+}$, as described previously for the L^2 analog.[1,9] Molar absorptivities were calculated under the assumption that the solution yields of $L^1(H_2O)Rh(NO)^{2+}$ are 100%, as was shown to be the case for the closely related $L^2(H_2O)Rh(NO)^{2+}$ in our earlier work.[10] Solutions of $L(H_2O)Rh^{2+}$ (L = L^1, L^2) were prepared photochemically from the hydrides $L(H_2O)RhH^{2+}$.[10,11] UV-Vis spectral data for $L^2(H_2O)Rh(NO)^{2+}$, $L^2(H_2O)Rh(NO_2)^{2+}$, $L^2(H_2O)RhH^{2+}$, $L^1(H_2O)Co(NO)^{2+}$ and $L^2(H_2O)Co(NO)^{2+}$ were obtained earlier,[9,10] and those for $L^1(H_2O)CoCH_3^{2+}$ were taken from the literature.[12] The UV-Vis spectrum of $Co(NH_3)_5CH_3^{2+}$ prepared in this work exhibited bands at 481 nm (ε 50 M^{-1} cm^{-1}) and 358 nm (ε 118 M^{-1} cm^{-1}), in good agreement with the literature (λ_{max} 481 nm, ε 50 M^{-1} cm^{-1}; λ_{max} 358 nm, ε 128 M^{-1} cm^{-1}).[13]

A third maximum observed in this work at 306 nm (ε 119 M^{-1} cm^{-1}) has not been reported previously. Instead, the absorbance in the published spectrum of $Co(NH_3)_5CH_3^{2+}$ rises sharply below 330 nm,[13] most likely because of the presence of trace amounts of O_2 and formation of strongly absorbing superoxo and peroxo complexes that can obscure the 306 nm band. All of the structural and UV-Vis data are summarized in Tables 1 and 2.

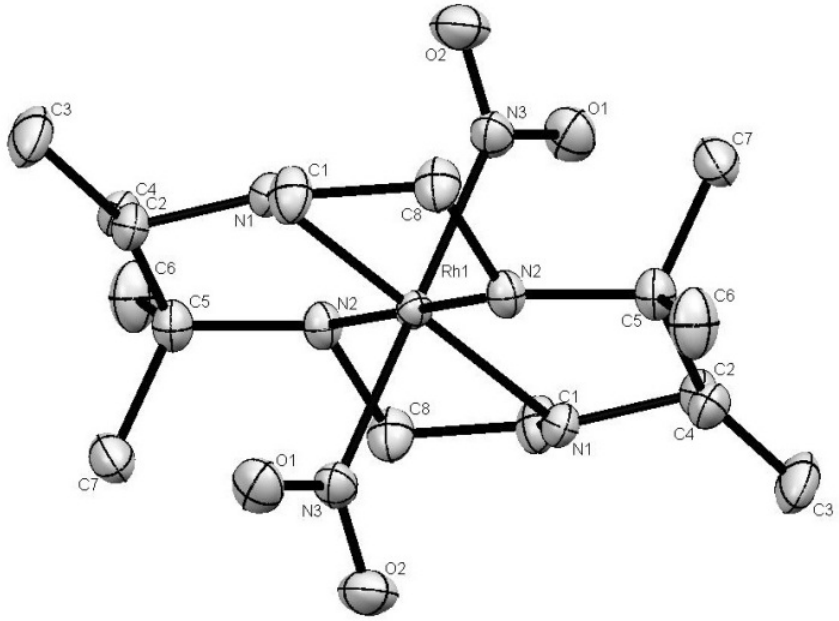

Figure 2. ORTEP drawing of the cation *trans*-$[L^2(H_2O)Rh(NO_2)_2]^+$ at the 50% probability level. Selected bond lengths/Å: Rh1-N1, 2.078(2); Rh1-N2(A), 2.090(2); Rh1-N3, 2.061(2); N3-O1, 1.243(3); N3-O2, 1.240(2). Angles/deg: N1-Rh1-N2, 95.74(8); N1-Rh1-N3, 94.01(8); N2-Rh1-N3, 93.29(8); Rh1-N3-O1, 120.2(2); Rh1-N3-O2, 121.3(2); O1-N3-O2, 118.6(2).

Steady-state photolysis of $Co(NH_3)_5CH_3^{2+}$ was performed in standard 1-cm fluorescence quartz cells at 313 nm (Luzchem LZC-5 photoreactor), 419 nm and 575 nm (Rayonet). Laser flash photolysis utilized a dye laser system[14] and LD490 dye (Exciton). Ethane and methane were analyzed with an Agilent Technologies 7890A gas chromatograph equipped with an FID detector and capillary column (GS-GASPRO, 15 m).[15] The concentration of C_2H_6 generated by

photolysis of $Co(NH_3)_5CH_3^{2+}$ were determined by comparison of the GC areas with those obtained for solutions of known concentrations of C_2H_6.

Computational

Unless stated otherwise, all structures are gas-phase optimized at the B3LYP[16,17] level of density functional theory (DFT) using the cc-pVDZ[18] basis set for non-metals and the relativistic small core Stuttgart effective core potential[19,20] for metals. In addition, Hessians were calculated and frequencies checked to ensure that all optimized structures were minima on the potential energy surface. To understand the UV-Vis spectra, single point TDDFT calculations using the optimized structures were completed. These calculations used the same basis sets as for the optimizations, and B3LYP,[16,17] PBE0,[21] and CAM-B3LYP[22] were used to determine differences with functionals. Since the results did not change significantly with the different functionals, only the B3LYP results are reported here. All values are available in the supporting information. To incorporate solvent effects, single point TDDFT-COSMO[23] and TDDFT-PCM[24] results were also computed. The dielectric constants of 78.15 and 7.85 were used for water and THF, respectively. The TDDFT-COSMO and TDDFT-PCM results were compared with the gas phase results and with each other to understand the effect of solvation and whether the solvation model had a significant impact on the results. All calculations were performed with NWChem[25] with the exception of the TDDFT-PCM calculations which were completed with GAMESS.[26,27] Natural orbitals were calculated using TDDFT-PCM within the Tamm-Dancoff approximation[28-30] and visualized with MacMolPlot[31] to analyze the electronic transitions.

Results and Discussion

Structural considerations

Table 1. Key Bond Distances in Å [a]

Compound	M-N[b]	M-H_2O	M-X
$[L^1(H_2O)RhCl]^{2+}$	2.11	2.24	2.32
$[L^1(H_2O)RhNO]^{2+}$	2.11	2.63	1.97
$[L^2(H_2O)RhH]^{2+}$	2.13	2.43	1.51
$[L^2(H_2O)RhNO]^{2+}$	2.12 [2.087][c]	2.73 [2.36]	1.95 [2.00]
$[L^2(H_2O)RhNO_2]^{2+}$	2.12 [2.081][c]	2.73 [2.12]	1.95 [1.99]
$[L^2Rh(NO_2)_2]^{2+}$	2.09 [2.078(2), 2.090(2)]	-	2.06 [2.061(2)]
$[L^1(H_2O)CoCH_3]^{2+}$	2.06 [1.97]	2.46 [2.15]	1.95 [2.01]
$[L^1(H_2O)CoNO]^{2+}$	2.01	2.68	1.82
$[L^2(H_2O)CoNO]^{2+}$	2.02	2.82	1.80
$[Co(NH_3)_5CH_3]^{2+}$	2.02 [1.97][c]	2.21[d] [2.10][d]	1.97 [1.98]
$[Co(NH_3)_5Cl]^{2+}$	1.97 [1.97][c]	1.98[d] [1.96][d]	2.28 [2.27]

[a] Experimental values (from this work and references [9,32-34]) are given in brackets.
[b] M-N distance in the equatorial ligand.
[c] Average M-N distance in the equatorial ligand.
[d] M-N distance to axial NH_3.

Table 1 shows key bond distances from the computations and experiments where available. In general, the structural agreement is good, giving confidence in the computational approach. The M-N bonds in M-L^2 complexes are only slightly longer (~0.01 Å) than those in M-L^1 complexes. The exceptions to the good agreement are the M-H_2O distances in $[L^2(H_2O)RhNO]^{2+}$ and $[L^2(H_2O)RhNO_2]^{2+}$. In both cases the calculated values are significantly larger than those obtained from crystal structure. It is not clear whether these differences are the result of crystal forces or issues with the computational method. It is possible that neither experimental nor calculated gas phase structures adequately represent solution structures.

However, as will be discussed below, the observed structural differences do not significantly affect overall conclusions regarding electronic transitions in these complexes.

Visible light photolysis

Slow, steady state photolysis of $Co(NH_3)_5CH_3^{2+}$ in 6 M ammonia caused no observable decrease at the 481 nm maximum. Only trace amounts of C_2H_6 were detected by GC. This result is consistent with either a complete lack of reaction, or by an equilibrium situation whereby the photochemical cleavage of the Co-CH_3 bond is reversed in the follow-up dark reaction, as shown in Eq 1. In this frequently encountered situation, the dimerization of low concentrations of the initially formed radicals results in a build-up of small amounts of the metal fragment ($Co(NH_3)_5^{2+}$/ $Co(NH_3)_6^{2+}$/ $Co(NH_3)_5(H_2O)^{2+}$) which prevents further loss of $Co(NH_3)_5CH_3^{2+}$ by pushing the equilibrium in eq 1 to the left.

$$Co(NH_3)_5CH_3^{2+} \underset{\text{?}}{\overset{h\text{?}}{\rightleftharpoons}} Co(NH_3)_5^{2+} + {}^{\bullet}CH_3 \qquad (1)$$

$$\downarrow$$

$$0.5\ C_2H_6$$

In contrast, when a solution of 6 mM $Co(NH_3)_5CH_3^{2+}$ was exposed to 60 successive 490-nm laser shots, there was a significant loss of absorbance in the visible, as shown in Figure 3. Also, large amounts of ethane and traces of methane were observed by GC. This result shows unequivocally that methyl radicals were produced. In addition, the computational results predict an excitation that involves transitions to the Co-C antibonding orbital at a wavelength close to the experimentally observed λ_{max} of 481 nm, as shown later. The large concentration of radicals (1-10 μM)[35] generated in a laser shot makes the second-order dimerization competitive with the ${}^{\bullet}CH_3/Co(NH_3)_5^{2+}$ recombination even when measureable amounts of $Co(NH_3)_5^{2+}$ had accumulated in solution. This is why there is a net loss of $Co(NH_3)_5CH_3^{2+}$ in laser experiments

but not under steady-state irradiation. Taking into account the 2:1 stoichiometric factor in Eq 1, the yields of C_2H_6 (by GC) were identical to the loss of $Co(NH_3)_5CH_3^{2+}$ (by UV-Vis) within reasonable error (± 30%) associated with quantitative determination of C_2H_6.

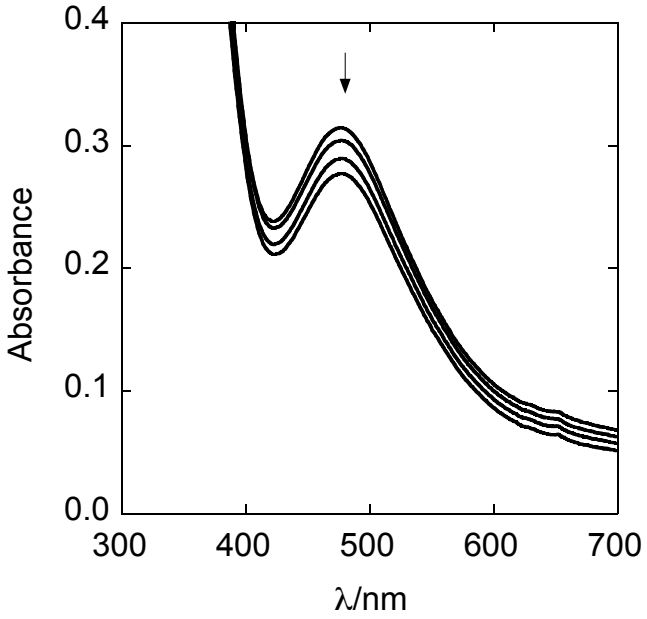

Figure 3. Absorbance decrease caused by laser flash photolysis of $Co(NH_3)_5CH_3^{2+}$. The spectra, in the descending order, were taken after 0, 20, 40, and 60 laser shots.

Computations

Table 2 shows λ_{max} for all of the complexes in this study. Both experimental and computational (gas-phase, COSMO and PCM) data are included. In general, good qualitative agreement is seen between the two. In particular, the large red shifts seen in the NO-containing complexes are reproduced well. Also, inclusion of solvent effects, either through COSMO or PCM models, generally brings the results into better agreement with the experiment. The differences between computed and experimental values range from 13-56 nm for gas phase, 6-48 nm for COSMO and 7-52 nm for PCM.

Table 2. Computational and Experimental λ_{max}/nm.[a, b]

Compound	Gas Phase	COSMO	PCM	Experimental
$[L^1(H_2O)RhCl]^{2+}$	311	302	298	350
$[L^1(H_2O)RhNO]^{2+}$	651	657	671	664
$[L^2(H_2O)RhH]^{2+}$	314	296	297	290
$[L^2(H_2O)RhNO]^{2+}$	622 666[c]	633 685[c]	697[c]	650
$[L^2(H_2O)RhNO_2]^{2+}$	-	-	-	-
$[L^2Rh(NO_2)_2]^{2+}$	-	-	-	-
$[L^1(H_2O)CoCH_3]^{2+}$	498	464	462	476
$[L^1(H_2O)CoNO]^{2+}$	730	736	751	739
$[L^2(H_2O)CoNO]^{2+}$	694	702 743[d]	756[d]	750
$[Co(NH_3)_5CH_3]^{2+}$	522	517	466	481
$[Co(NH_3)_5Cl]^{2+}$	532	498	497	530

[a] Experimental data from this work and references[3,9,10,13,36,37].
[b] Symbol "-" indicates no absorptions in the visible.
[c] Values obtained by use of experimental M-H_2O distance given in Table 1, see text.
[d] Values obtained by use of a Co-N-O bond angle of 127º, see text.

Among the rhodium complexes, one of the larger differences between the observed and gas-phase calculated spectra is found for $[L^2(H_2O)RhNO]^{2+}$ (650 nm vs 622 nm, respectively). The calculated Rh-H_2O bond length (2.73 Å) is significantly greater than the experimental value (2.36 Å), Table 1.

To explore the extent to which the coordinated molecule of water is important to the electronic structure and photochemistry of $[L^2(H_2O)RhNO]^{2+}$, additional calculations were performed in which the Rh-H_2O bond length was changed to the experimental value (2.36 Å) while keeping all of the remaining atoms in their fixed positions. The resulting structure was less than 1 kcal/mol higher in energy than the optimized structure when the COSMO solvation is included. This result suggests that the Rh-H_2O distance can change substantially by environmental effects. As seen in Table 2, changing the bond length alone can have considerable impact on the calculated λ_{max} and it seems reasonable to surmise that the water molecule is complexed to the metal with a bond length in solution lying somewhere between the

gas-phase-optimized and crystal structure values. However, by examining the transitions that occur in the optimized and modified structures with the TDDFT-PCM calculations, it is observed that the general character of the transition (Rh-N bonding to Rh-N antibonding) does not change by changing the Rh-H_2O distance.

Experimental and computed spectra were also obtained for $[L^2(H_2O)RhNO]^{2+}$ in THF as solvent. Since it is not clear whether H_2O is still present after dissolution of the complex in THF, calculations also included the pentacoordinated complex $[L^2RhNO]^{2+}$. The results shown in Table 3 suggest that water is still bound, although at a greater distance than in the water-solvated structure. Just in case a solvent THF molecule has replaced the axial molecule of water, an additional optimization and COSMO TDDFT calculation was performed and yielded λ_{max} of 656 nm and a rather long Rh-THF distance of 2.65 Å. Comparison with the experimental value (630 nm) suggests that the axial water is still bound in THF. In all of these cases, the change of solvent or coordination number does not change the basic nature of the transition, see Table SI2.

Table 3. Effect of Rh-H_2O Distance on COSMO Values of λ_{max} for $[L^2(H_2O)RhNO]^{2+}$ in THF

	COSMO			Experimental
Bond length/ Å	2.73	2.36	∞	N/A
λ_{max}	631	681	583	630

Another complex in Table 2 for which computation and experiment differ significantly is $[L^2(H_2O)CoNO]^{2+}$. The gas-phase optimized geometry predicted a Co-N-O bond angle of 121º, about the same as for the L^1 complex. The use of this angle yields λ_{max} = 702 nm (COSMO, Table 2). However, a review of literature on similar Co complexes[38-41] revealed significant variations in this bond angle, from 120-128º. By adjusting the Co-N-O bond angle to 127º, the calculations gave λ_{max} = 743 nm, in much better alignment with experimental λ_{max} = 750 nm

(Table 2). Also, the resulting structure is less than 1 kcal/mol higher in energy than the fully optimized structure when the COSMO solvation model is used. These results suggest that the Co-N-O angle may be larger in solution than in the gas phase. Again, the character of the transitions, Co-NO bonding to antibonding, did not change with changes in the Co-N-O angle.

For all complexes with X = H, CH_3, and NO, the visible spectra involve transitions into an anti-bonding M-X orbital, in agreement with the homolytic cleavage seen experimentally. In nitrosyl complexes (which exhibit the largest λ_{max}) of both cobalt and rhodium, the transition is from an orbital that is mostly metal-NO bonding (d_{z2} and p_z atomic orbitals on the metal and a mixture of p atomic orbitals on nitrogen). However, there is a small contribution from d-orbitals as well. These are often the HOMO for the system. In $L^1(H_2O)CoCH_3^{2+}$, the Co-CH_3 bonding orbital and d orbitals are closer in energy, so that the donor orbitals associated with λ_{max} are a stronger mixture of the two. This is similar to the description by Mok and Endicott.[3] However, the three center model is not as clear in the molecular orbital calculations of this study which shows that the donor orbital is more of an M-C bonding type. In agreement with experiment, λ_{max} is shorter for $L^1(H_2O)CoCH_3^{2+}$ (464 nm for the COSMO calculations) than for $L^1(H_2O)CoNO^{2+}$ (736 nm). For M = Rh and X = H, λ_{max} is shorter yet (296 nm). The Rh-H bonding orbital is much lower in energy compared to the HOMO and does not contribute to the transition, whereas the highest occupied orbitals are metal non-bonding d orbitals that do contribute.

For the X = Cl and NO_2 compounds, any UV spectra involve metal-to-ligand and weak d-d transitions. The spectral lines that involve a bonding-to-antibonding transition are much higher in energy and are a mixture of many orbital contributions. The M-X bonding orbitals are much lower in energy than the HOMO.

Conclusions

Visible light photolysis of transition metal complexes of the type $L(H_2O)M\text{-}X$ where L is a saturated N_4 macrocyclic equatorial ligand (L^1, L^2) and M = Co or Rh, has been shown previously[1,3,6] to lead to homolytic M-X cleavage for X = NO, O_2, and R, but not for X = Br, Cl, SO_4, NO_3, etc.[2] In this work we have shown that visible light also causes photodissociation of the Co-C bond in $(NH_3)_5CoCH_3^{2+}$.

Experiment and computation agree that for compounds having X = CH_3 and NO the observed bands in the visible involve an M-X bonding to antibonding transition. This is also true for the near-UV bands in the spectra of rhodium hydrides $L(H_2O)RhH^{2+}$ (L = L^1, L^2). On the other hand, the related complexes with X = Cl or NO_2 show these transitions at much shorter wavelengths. The findings for macrocyclic complexes and for $(NH_3)_5CoCH_3^{2+}$ are similar, showing that UV-Vis spectra are not significantly dependent on the structure of the equatorial ligands.

Acknowledgements

This research was supported by the U.S. Department of Energy, Office of Science, Office of Basic Energy Sciences, Division of Chemical Sciences, Geosciences, and Biosciences through the Ames Laboratory Catalysis and Chemical Physics programs. The Ames Laboratory is operated for the U.S. Department of Energy by Iowa State University under Contract No. DE-AC02-07CH11358. This research (EAH) was also supported by the National Science Foundation under Grant No. OISE-0730114 for the Partnerships in International Research and Education (PIRE).

References

(1) Song, W.; Kristian, K.; Bakac, A. *Chem. Eur. J.* **2011**, *17*, 4513-4517.

(2) Zinato, E. In *Concepts of Inorganic Photochemistry*; Adamson, A. W., Fleischauer, P. D., Eds.; Wiley: New York, 1975.

(3) Mok, C. Y.; Endicott, J. F. *J. Am. Chem. Soc.* **1978**, *100*, 123-129.

(4) Bergkamp, M. A.; Brannon, J.; Magde, D.; Watts, R. J.; Ford, P. C. *J. Am. Chem. Soc.* **1979**, *101*, 4549-4554.

(5) Kelly, T. L.; Endicott, J. F. *J. Phys. Chem.* **1972**, *76*, 1937-1946.

(6) Mok, C. Y.; Endicott, J. F. *J. Am. Chem. Soc.* **1977**, *99*, 1276-1277.

(7) Blessing, R. H. *Acta Cryst.* **1995**, *A51*, 33-38.

(8) Bruker *Bruker APEX II Suite. Ver.2014.5-0. Bruker AXS Inc., Madison, Wisconsin, USA. 2014***.**

(9) Kristian, K.; Song, W.; Ellern, A.; Guzei, I. A.; Bakac, A. *Inorg. Chem.* **2010**, *49*, 7182-7187.

(10) Bakac, A.; Pestovsky, O.; Durfey, B. L.; Kristian, K. E. *Chem. Sci.* **2013**, *4*, 2185-2192.

(11) Bakac, A.; Thomas, L. M. *Inorg. Chem.* **1996**, *35*, 5880-5884.

(12) Roche, T. S.; Endicott, J. F. *Inorg. Chem.* **1974**, *13*, 1575-1580.

(13) Kofod, P. *Inorg. Chem.* **1995**, *34*, 2768-2770.

(14) Melton, J. D.; Bakac, A.; Espenson, J. H. *Inorg. Chem.* **1986**, *25*, 4104-4108.

(15) Carraher, J. M.; Pestovsky, O.; Bakac, A. *Dalton Trans.* **2012**, *41*, 5974-5980.

(16) Becke, A. D. *J. Chem. Phys.* **1993**, *98*, 5648-5652.

(17) Becke, A. D. *J. Chem. Phys.* **1992**, *96*, 2155-2160.

(18) Dunning, T.H., Jr. *J. Chem. Phys.* **1989**, 1007-1023.

(19) Dolg, M.; Stoll, H.; Preuss, H.; Pitzer, R. M. *J. Phys. Chem.* **1993**, *97,* 5852-5859.

(20) Bergner, A.; Dolg, M.; Kuechle, W.; Stoll, H.; Preuss, H. *Mol. Phys.* **1993**, *80,* 1431-1441.

(21) Adamo, C.; Barone, V. *J. Chem. Phys.* **1998**, *110*, 6158-6170.

(22) Yanai, T.; Tew, D.; Handy, N. *Chem. Phys. Lett.* **2004**, *393*, 51-57.

(23) Klamt, A.; Schuurmann, G. *J. Chem. Soc., Perkin Trans.* **1993**, *2*, 799-805.

(24) Cossi, M.; Rega, N.; Scalmani, G.; Barone, V. *J Comput Chem* **2003**, *24*, 669-681.

(25) Valiev, M.; Bylaska, E. J.; Govind, N.; Kowalski, K.; Straatsma, T. P.; Van Dam, H. J. J.; Wang, D.; Nieplocha, J.; Apra, E.; Windus, T. L.; de Jong, W. A. *Computer Physics Communications* **2010**, *181*, 1477-1489.

(26) Schmidt, M. W.; Baldridge, K. K.; Boatz, J. A.; Elbert, S. T.; Gordon, M. S.; Jensen, J. H.; Koseki, S.; Matsunaga, N.; Nguyen, K. A.; Su, S. J.; Windus, T. L.; Dupuis, M. M., J. A. *J. Comput. Chem.* **1993**, *14*, 1347−1363.

(27) Gordon, M. S.; Schmidt, M. W. *Theory and Applications of Computational Chemistry: The First Forty Years*; Elsevier: The Netherlands, 2005.

(28) Dancoff, S. M. *Physical Review* **1950**, *78,* 382-385.

(29) Tamm, I. *J. Phys. (USSR)* **1945**, *9*, 449.

(30) Hirata, S.; Head-Gordon, M. *Chem. Phys. Letters* **1999**, *314*, 291-299.

(31) Bode, B. M.; Gordon, M. S. *Journal of Molecular Graphics and Modelling* **1998**, *16*, 133-138.

(32) Endicott, J. F.; Halko, D.; Roche, T. S.; Glick, M. D.; Butler, W. In *International conference on coordination chemistry*; Davis, W. J., Ed. Dublin, 1974, p 343.

(33) Kofod, P.; Harris, P.; Larsen, S. *Inorg. Chem.* **1997**, *36*, 2258-2266.

(34) Messmer, G. G.; Amma, E. L. *Acta Cryst.* **1968**, *B24*, 417-422.

(35) Bakac, A.; Espenson, J. H. *Inorg. Chem.* **1989**, *28*, 3901-3904.

(36) Bakac, A. *J. Am. Chem. Soc.* **1997**, *119*, 10726-10731.

(37) Bakac, A.; Espenson, J. H. *Inorg. Chem.* **1987**, *26*, 4353-4355.

(38) Groombridge, C. J.; Larkworthy, L. F.; Mason, J. *Inorg. Chem.* **1993**, *32*, 379-380.

(39) Scheidt, W. R.; Hoard, J. L. *J. Am. Chem. Soc.***1973**, *95*, 8281-8288.

(40) Dios, A. C. d.; Roach, J. L. *J. Phys. Chem. A* **1999**, *103*, 3062-3065.

(41) Wyllie, G. R. A.; Scheidt, W. R. *Chem. Rev.* **2002,**, *102*, 1067-1089.

CHAPTER 3: REACTIONS OF NIOBIUM MONO AND DICATIONS WITH CO AND CO_2

Emily Hull*, Gustavo Davico+, Theresa L. Windus*

*Department of Chemistry and Ames Laboratory USDOE, Iowa State University, Ames, Iowa 50011, USA
+Deceased

Abstract

Niobium mono- and dications were created and reacted with CO and CO_2 in a flowing afterglow instrument and points on the potential energy surfaces for the reactions were calculated using Density Functional Theory (DFT), Multi-Configurational Self-Consistant Field (MCSCF) and Multi-Reference Perturbation Theory (MRPT2). Nb mono and dications react with CO in clustering reactions. Only the mono cluster of Nb^+-CO was observed for monocations, but higher order clusters, $Nb(CO)_n^{2+}$, were observed for dications. DFT calculations indicate that higher order complexes are favorable for both mono and dications. Reactions with CO_2 activate the C-O bond to form the metal oxide and carbon monoxide with monocations activating the C-O bond more efficiently. Charge transfer reactions were not observed for Nb^{2+} reactions with CO_2. DFT and MRPT2 calculations indicate that the difference in observed reaction efficiency between the mono and dications is due to the barrier height for a spin crossing and the exothermicity of the mono and dication products. Submitted to the Journal of Physical Chemistry A.

Introduction

The chemistry of transition metals is a large diverse field full of unique and sometimes surprising species. While understanding the chemistry of transition metal species is of interest to many fields of science and engineering, very little is known about the gas phase chemistry of transition metals, particularly transition metal ions. In many transition metals, the ground and excited states are very close in energy, meaning that even at room temperature the exited states can be significantly populated. It is therefore important when vaporizing and ionizing solid metal species to ensure that one has achieved the state of interest. Care must also be taken to dissipate the excess energy of vaporization and ionization to ensure that endothermic products are not observed. The use of flowing afterglow instrumentation has been shown to help minimize these issues[1].

There is interest in the application of transition metal chemistry to the field of CO_2 sequestration and conversion. For example, in nature plants can reduce CO_2 into simple sugars by utilizing the octahedrally coordinated Mg^{2+} center of the Rubisco protein[2]. This protein, present in nearly every photosynthesizing organism, is considered by many as the most abundant protein on earth[3]. Humans have sought to understand and create synthetic methods for conversions of CO_2 to chemicals less damaging to our environment[4-6]. Transition metals, with their known catalytic uses, makes them ideal candidates to better understand the process of C-O activation in CO_2 and its applications for carbon sequestration[7].

Another atmospheric gas whose concentration has increased due to combustion is CO. While CO concentrations are not nearly as alarming as those of CO_2, it is curiously present at the active site of many metalloproteins, and is often required for enzymatic activity[8]. The presence

of a CO ligand in the nickel-iron containing enzyme carbon monoxide dehydrogenase from *Rhodospirillum Rubrum*[9] is one such example. This molecule reversibly oxidizes CO to CO_2, which can then be utilized by the organism for the production of simple sugars. Therefore, understanding the fundamental interactions of metal ions with CO and CO_2 are of basic scientific interest.

Previous studies of transition metals reacting with CO and CO_2 have used different experimental apparatus[10,11], different computational methods[12-14], and have focused mainly on monocation reactions[15]. This paper adds to those studies by specifically exploring the reactions of Nb cations with CO and CO_2. Our previously published work[15] included the reaction of vanadium monocation with CO and CO_2 - these reactions showed that vanadium will cluster with both gases, but not activate the C-O bond in CO_2. This work continues to explore the gas phase reactions of group 5 elements, specifically Nb, with CO and CO_2.

Materials and Methods

Study of gas phase Nb-ligand reactions was accomplished by utilization of a flowing afterglow instrument. The basic instrumentation was described in our previously paper, and is not discussed in detail here[1,15,16]. The instrument was modified by addition of an ion glow discharge sputter source for the generation of metal ions. The sputter ion source is similar to the one described by Lineberger for the production of negative ions, and was placed upstream and on the side of the flowing afterglow tube[17,18]. Sputtering was accomplished by the addition of a small amount of Ar to the He buffer gas. Experimental conditions were typically 13 SLM of He flow and Ar flow ranging between 0.5-1.6%, adjusted to optimize the dication ion signal. The system had a mass flow sensor only on the He line. Ar flow was determined by noting the flow

tube pressure prior to and after closing the inlet valve on the Ar line. After the Ar was removed, the prior pressure (Ar + He) was matched by increasing the He flow. The change in the He flow was recorded as the Ar flow and the total gas flow (Ar + He) was used to determine the rate constants. Gases utilized were of the following purities: Ar (99.95%), He (99.95%), carbon dioxide (99.99%) and carbon monoxide (99.0%).

Purities of Nb were (99.8+%). The metal was placed in the sputter chamber and its cations introduced to the flow tube 50.0 centimeters from the first neutral inlet. The neutral reactants (CO or CO_2) were added to the flow tube through one of seven additional shower type nozzles located at different points along the flow tube. Mass spectra were then collected and peaks identified. Fast rate constants (10^{-11} cm^3 $molecule^{-1}$ s^{-1}) enabled determination of the reaction rate by monitoring disappearance of the reactant ion. When reactions were slower, rates were determined by following the appearance of the product ion. Extraction of reaction rate constants was accomplished utilizing pseudo first order conditions and statistical means previously reported[15]. Rate constants were determined at 298±2 K after running the experiment in triplicate and the reported errors are one standard deviation of the final rate constant value or the fitting procedure, whichever is greater.

Density Functional Theory (DFT) calculations were performed with the NWChem[19] program suite at the B3LYP[20,21] level using the UDFT methodology for open shell systems. The LANL2dz effective core potential (ECP)[22] and associated valence orbital basis set was used for Nb and the 6-311+G* Pople[23] basis set was used for C and O. Geometries were optimized under tight grid convergence criteria utilizing symmetry where possible and Hessians were used to ascertain whether a structure was a minimum, a transition state, or higher order saddle point. A temperature of 298 K is used to maintain consistency with the rate constants for calculation of

Gibbs free energies. Due to the possibility of near degeneracies and changes in spin states as reactions progress, two spin states for each species were studied in this work. Structures were optimized for each state.

For reactions involving Nb mono and dications with CO_2, geometries were re-optimized with Multi-Configurational Self-Consistent Field[24-33] (MCSCF) and single point second order Multi-Reference Perturbation Theory[34-37] (MRPT2) calculations were performed at the MCSCF geometries using GAMESS[38,39] to understand any discrepancies between the DFT and experimental results. For the MCSCF and MRPT2 calculations, a LANL2TZf ECP[22] and valence basis set was used for Nb and aug-cc-pVTZ[40] was used for the C and O. Where possible Hessians were calculated for the MCSCF optimized geometries to ensure that each geometry represented the lowest energy minima with no imaginary frequencies for the reaction coordinate, or one and only one imaginary frequency for the transition state. Where the size of the active space made a Hessian prohibitively expensive, the Hessian of a reduced active space was used. Zero-point energies of the MCSCF calculations were compared with those found in DFT calculations to ensure the validity of this approximation.

While the actual reactions will be discussed below, the active spaces for the reactions are discussed here. The active space for the MCSCF and MRMP2 calculations for the reactant side (reactants, reaction side complex) consisted of the 5 metal d orbitals, and the complete valence active space for CO_2. The transition state, product side complex and products involve NbO and CO. The active space for those complexes include the CO σ and σ*orbitals, π and π* orbitals, and an additional carbon 2s orbital, and include the Nb-O bonding and anti-bonding orbitals and any Nb non-bonding orbitals. When combined, all actives spaces for every reaction complex combine for a 16 electrons in 15 orbital space for the monocation, and 15 electrons in 15 orbitals

for the dications. This was deemed computationally sufficient in addition to being at the limit of computational feasibility for these systems. More detail on the calculation will be given in the following sections. All geometries and absolute energies are available in the supporting information.

Results and Discussion

Reactions of Nb ions with CO

Gas-phase reactions of Nb ions with CO under the conditions described above involve a three-bodies. As the metal ion collides with the CO there is a competition between the kinetic energy of collision and the free energy gained by forming a complex. The kinetic energy of the collision must be transferred to internal energy for complexation to occur, thus requiring a collision with another body (such as the buffer gas) to add collisional deactivation and stabilization. The formation of $Nb(CO)_n^{x+}$ (where x = 1 or 2 and n = 1 to 8) is, therefore, a stepwise process with the formation of the monocluster (n=1) being the primary reaction product and rate limiting step. It is expected that if the formation of the monocomplex is observed, higher order complexes ($n \geq 2$) should also be favorable because the addition of each CO spreads the complexation energy over more degrees of freedom. The addition of CO is not likely to be infinite, but will have some limit. Thinking qualitatively about the process of complexation, there are multiple reactants going to a single product and the entropy of the system is therefore reducing with the magnitude of ΔS increasing with the increasing order of complexation. This entropic effect could therefore become significant in limiting the spontaneity of higher order complexes in addition to simple size-based steric hindrance.

Monocations

Table 1: Experimental results of the reactions of Nb^{x+} with CO. NR= No reaction NC= Not calculated

Metal	Rate[a]	Product	Eff[b]	Secondary product	Rate	k_{col} CO
Nb^+	$1.1 \pm 0.1 \times 10^{-13}$	$NbCO^+$	0.0002	NR	NR	7.29×10^{-10}
Nb^{2+}	$4.5 \pm 0.4 \times 10^{-12c}$	$Nb(CO)^{2+}$	0.003	$Nb(CO)_n^{2+}$ [n = 4-6]	NC	1.46×10^{-9}

[a] Observed rate constant, k_{obs}, in units cm^3 $molecules^{-1}s^{-1}$ [b] Reaction efficiency, k_{obs}/k_{col}, where the rate of collisions, k_{col}, is calculated according to literature[41] [c] High error due to utilization of all $Nb(CO)_n^{2+}$ [n=4-6] ion product to calculate the rate constant.

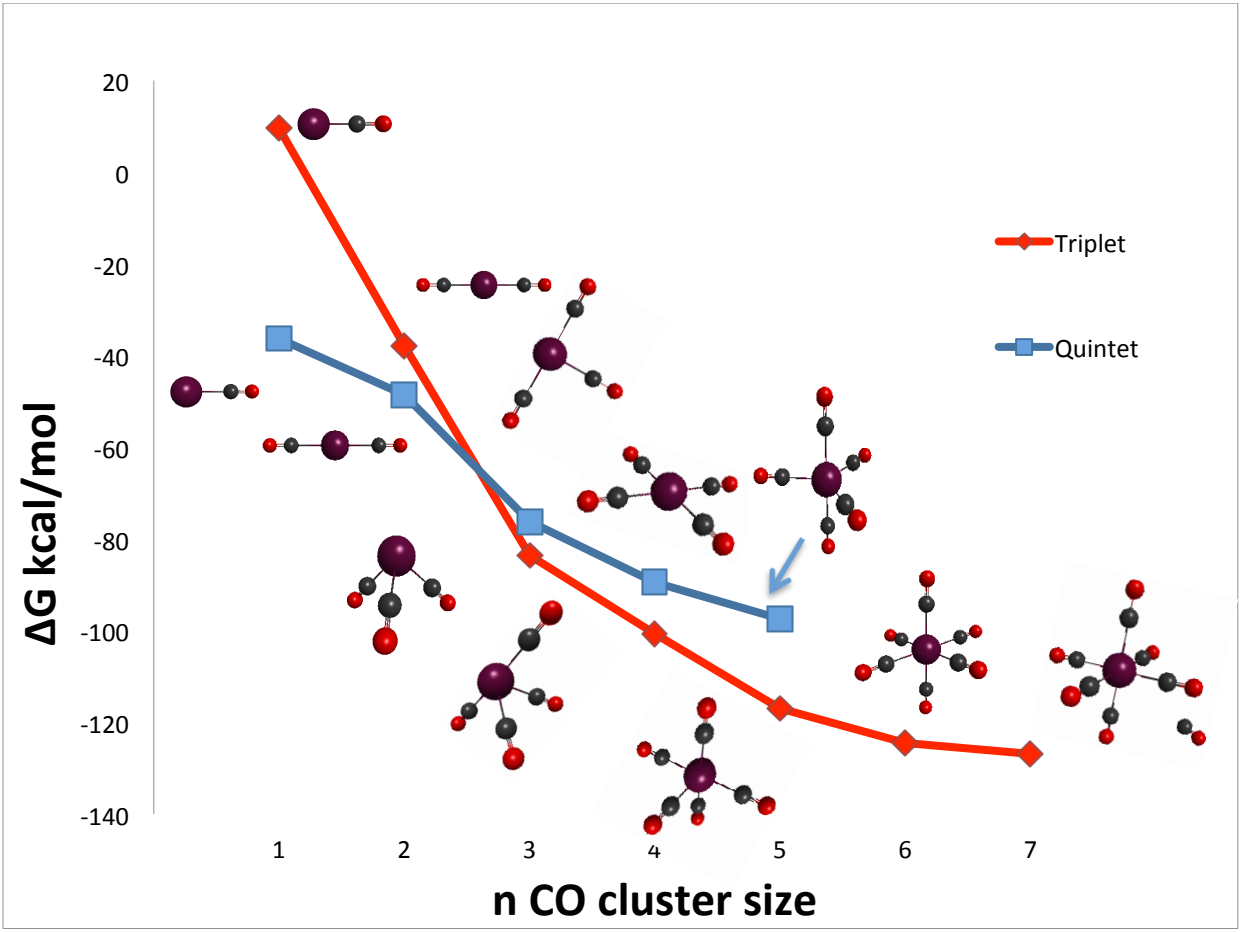

Figure 1: Calculated free energies for each of the potential products of the reaction of Nb^+ and nCO. The red points represent the quintet spin states and the blue points are the triplet spin states. For a given sized complex with n COs, the lowest energy structure between the two electronic states is shown as lower in the figure. The large ruby spheres are the Nb, small black spheres are C and the red spheres are O. The same coloring is used for all figures throughout this work.

Table 2: DFT calculated free energies for the reactions of Nb^+ and CO where $\Delta G_{rxn} = \Sigma\Delta G_{products} - \Sigma\Delta G_{reactants}$ and free energies of per CO complexation defined as the free energy for $Nb(CO)_{n-1}^+ + CO \rightarrow Nb(CO)_n^+$. All energies are in kcal/mol.

	ΔG_{rxn}		Complexation	
Species	Quintet	Triplet	Quintet	Triplet
$Nb(CO)_1^+$	-36.3	9.6	-36.3	9.6
$Nb(CO)_2^+$	-48.6	-37.8	-12.3	-47.4
$Nb(CO)_3^+$	-76.2	-83.6	-27.6	-45.8
$Nb(CO)_4^+$	-89.4	-100.6	-13.3	-17.0
$Nb(CO)_5^+$	-97.4	-116.9	-8.0	-16.4
$Nb(CO)_6^+$	***	-124.5	***	-7.5
$Nb(CO)_7^+$	***	-126.9	***	-2.4

For reactions of Nb^+ and nCO only formation of the monocomplex was observed experimentally. Table 1 shows that the reaction efficiency is very low, with only 0.02% of collisions resulting in reactions. Figure 1 shows the DFT free energies of the quintet and triplet states as a function of the number of CO molecules in the complex. The lowest energy structures for each value of n for both the quintet and triplet states are also shown in Figure 1. Formation of the monocluster, $Nb(CO)^+$ is favorable with a calculated ΔG of -36.3 kcal/mol for the quintet spin state, which is the ground state for this cluster as seen in Figure 1 and Table 2. While many different calculations were attempted for clusters larger than n=5 in the quintet state, none resulted in a minimum energy species with all COs at a reasonable bond length from the central Nb without imaginary frequencies. The results in Figure 1 show that for complexes larger than n=3 the triplet spin state becomes the lowest energy state, indicating a spin-crossing around n=3.

Analysis of the per-CO complexation energy in Table 2 shows that addition of each CO is favorable to a limit. Addition of a 7th CO to $Nb(CO)_6^+$ in the triplet state is nearly

thermoneutral and the 7th CO is at too far a distance to be considered bonded to the central Nb. This indicates that the $Nb(CO)_7^+$ calculated species is probably sterically hindered and unstable under the experimental conditions. If formed it would fall apart quickly. Therefore we surmise that the absolute complexation limit is probably $Nb(CO)_6^+$.

There are several possible explanations for the experimental observation of only the mono cluster but no higher order complexes. Part of it could be due to the order of magnitude difference between the mono and dication reaction rates, as seen in Table 1. Since the reaction efficiency is low to begin with, the rate of collision is too low for the formation of higher order complexes within the timescale of the experiment. Examining the computational data in Table 2 it is also observed that there is not a large gain in energy for forming the n=2 cluster. The three-body collision mechanism combined with the relatively small energy gain from adding the second CO may be another reason why nothing larger than the monocomplex was observed.

Dications

Table 1 shows that the major experimental product of the reaction of Nb^{2+} with CO is the monocluster, but higher order clusters of $Nb(CO)_n^{2+}$ where n=4-6 were observed in trace amounts. As reported in Table 3, all complexation energies between n=1 and n=6 are exoergic. In general, the exorgicity is larger for the dication complexes than that for the monocation complexes, which likely explains the formation of the larger clusters with the dications. The n=7 complexation energy is nearly thermoneutral for both the quartet and doublet spin states. While the doublet does indicate that all 7 are complexing directly to the central Nb, for the quartet spin state the addition of the 7th CO happens at too long a distance for direct complexation. While a doublet $Nb(CO)_8^{2+}$ structure was found in which all of the carbonyls are complexed directly with the Nb, addition of the 8th CO is endoergic. There is also a possible spin crossing between n=6

and n=8. The combination of low exoergicity with the addition of a 7th CO to $Nb(CO)_6^{2+}$, a possible spin crossing between $Nb(CO)_6^{2+}$ and $Nb(CO)_7^{2+}$ and the endoergic nature of the $Nb(CO)_8^{2+}$ combine to suggest that $Nb(CO)_6^{2+}$ is the complexation limit. The experimental detection of n=4-6 is supported by calculations reported in Figure 2 and Table 3 that show a flattening of the per CO complexation energy for the formation of complexes larger than n=3.

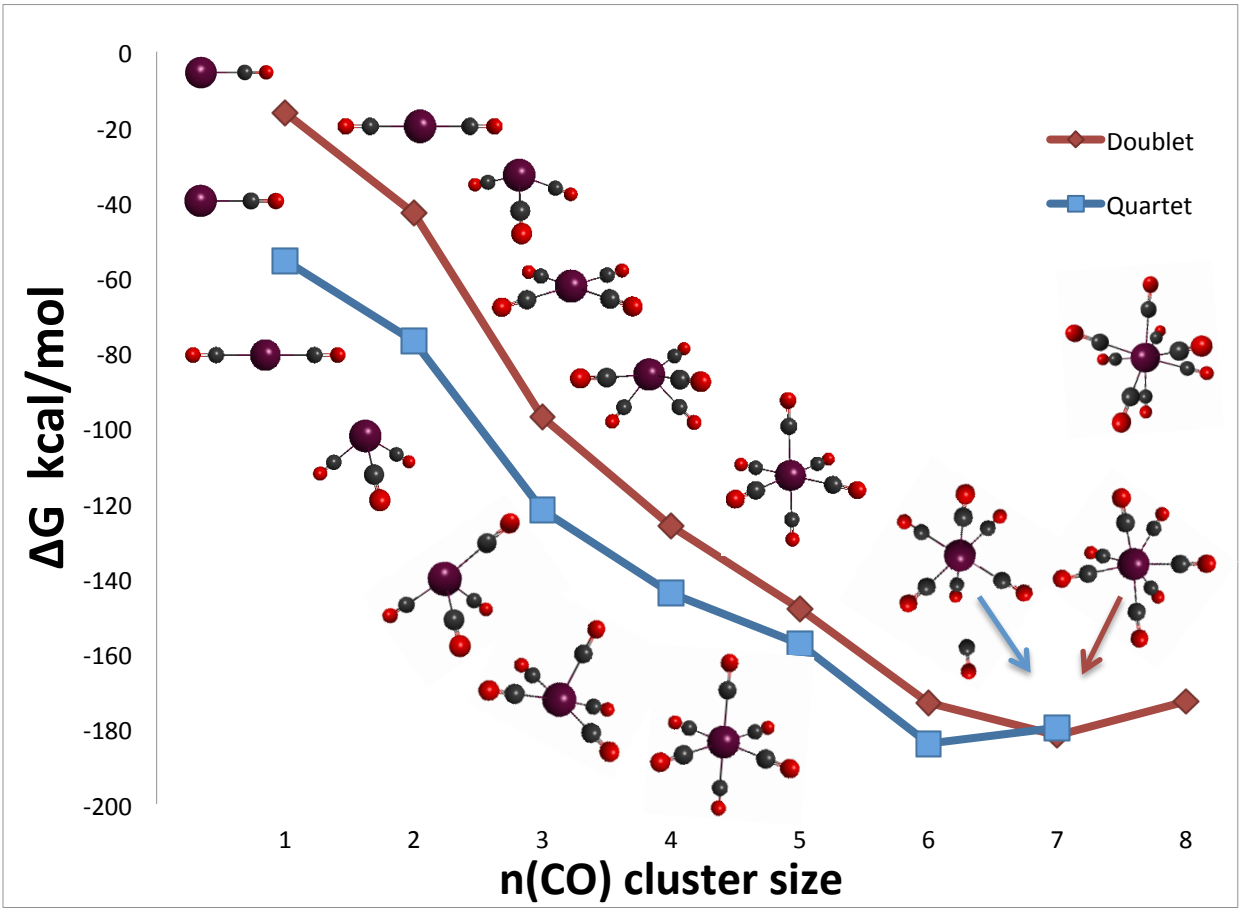

Figure 2: The DFT calculated free energies for the reaction of Nb^{2+} and nCO → $Nb(CO)_n^{2+}$. The red points represent the quartet spin states and the blue points are the doublet spin states. For a given sized complex with n COs, the lowest energy structure between the two electronic states is shown as lower in the figure. In the case of n=7 the CO dissociated structure is a quartet structure and the associated is the doublet. The structure shown as n=8 is only a doublet structure, and is above the doublet n=7 structure.

Table 3: DFT calculated Gibbs Free Energies for the reactions of Nb^{2+} and CO where $\Delta G_{rxn} = \Sigma\Delta G_{products} - \Sigma\Delta G_{reactants}$ and free energies of per CO complexation defined as the free energy for $Nb(CO)_{n-1}^{2+} + CO \rightarrow Nb(CO)_n^{+}$. All energies are in kcal/mol.

	ΔG_{rxn}		Complexation	
Species	Quartet	Doublet	Quartet	Doublet
$Nb(CO)_1^{2+}$	-55.5	-16.2	-55.5	-16.2
$Nb(CO)_2^{2+}$	-77.0	-43.0	-21.5	-26.8
$Nb(CO)_3^{2+}$	-121.9	-97.3	-44.9	-54.3
$Nb(CO)_4^{2+}$	-144.0	-126.1	-22.0	-28.8
$Nb(CO)_5^{2+}$	-157.5	-148.1	-13.5	-22.0
$Nb(CO)_6^{2+}$	-183.9	-173.1	-26.5	-25.0
$Nb(CO)_7^{2+}$	-179.7	-181.8	4.3	-8.7
$Nb(CO)_8^{2+}$	***	-172.8	**	8.9

Comparing the experimental results of the mono and dication in Tables 1, it can be seen that the collisional rate for the dication is twice that of the monocation. This is most likely due to the double charge, which makes the metal more attractive. The dication reactions were also observed to be many times faster and more efficient than the monocation. Part of that is again the double charge which makes the mechanism of collisional deactivation more likely simply because the double charge makes it more attractive and reactive. Examining the computational data in Tables 2 and 3, this difference in reaction rates is even clearer. Comparing the free energies of formation for the dication and monocation monoclusters it can be seen that the dication monocluster is roughly 1.5 times more exoergic than the monocluster.

Reactions of Nb ions with CO_2

Possible reactions of $Nb^{x+} + CO_2$ are complexation [formation of $Nb(CO_2)^{x+}$] or activation of the C-O bond to form metal oxide and carbon monoxide:

$Nb^{x+} + CO_2 \rightarrow NbO^{x+} + CO$ x=1,2 primary (1)

In these ion-neutral reactions there are five main reaction coordinates, the reactants, reactant side complex, transition state, product side complex, and products. The reactant side complex occurs when the neutral approaches the metal ion at a short enough distance for strong electrostatic or bonding interactions before the transition state (Nb^{x+} --- O-C-O). The product side complex occurs after the transition state when the neutral product is still attracted to, but not strongly bonded to the ion product (O-Nb^{x+} --- C-O).

In the case of the dication, charge transfer can also occur. Primary charge transfer could, occur on the reactants side near the reactant side complex:

Nb^{2+} --- O-C-O → Nb^{+} + OCO^{+} primary (2)

and Nb^{+} could then go on to react with another CO_2:

$Nb^{+} + CO_2 \rightarrow NbO^{+} + CO$ secondary (3)

Charge transfer could also occur around the product side complex as the products are dissociating:

O-Nb^{2+} --- CO → O-Nb^{+} + CO^{+} primary (4)

It can be expected then that only complexation and reaction 1 will occur in Nb^{+} reactions with CO_2. However in the case of dications, complexation and reactions 1 through 4 can occur. Because reactions 3 and 4 create the same metal oxide cation it is important to try and distinguish the mechanism of charge transfer.

Monocations

Table 4: Experimental results of the reactions of Nb^{x+} with CO_2. NR=no reaction.

Metal	Rate[a]	Product	Eff[b]	Secondary product	Rate	k_{col} CO_2
Nb^{+}	$3.40 \pm 0.04 \times 10^{-10}$	NbO^{+}	0.47	NbO_2^{+}	Trace	7.31×10^{-10}
Nb^{2+}	$2.35 \pm 0.05 \times 10^{-10}$	NbO^{2+}	0.16	NR	NR	1.46×10^{-9}

[a] Observed rate constant, k_{obs}, in units cm^3 $molecules^{-1}s^{-1}$ [b] Reaction efficiency, k_{obs}/k_{col}, where the rate of collision, k_{col}, is calculated according to literature.[41]

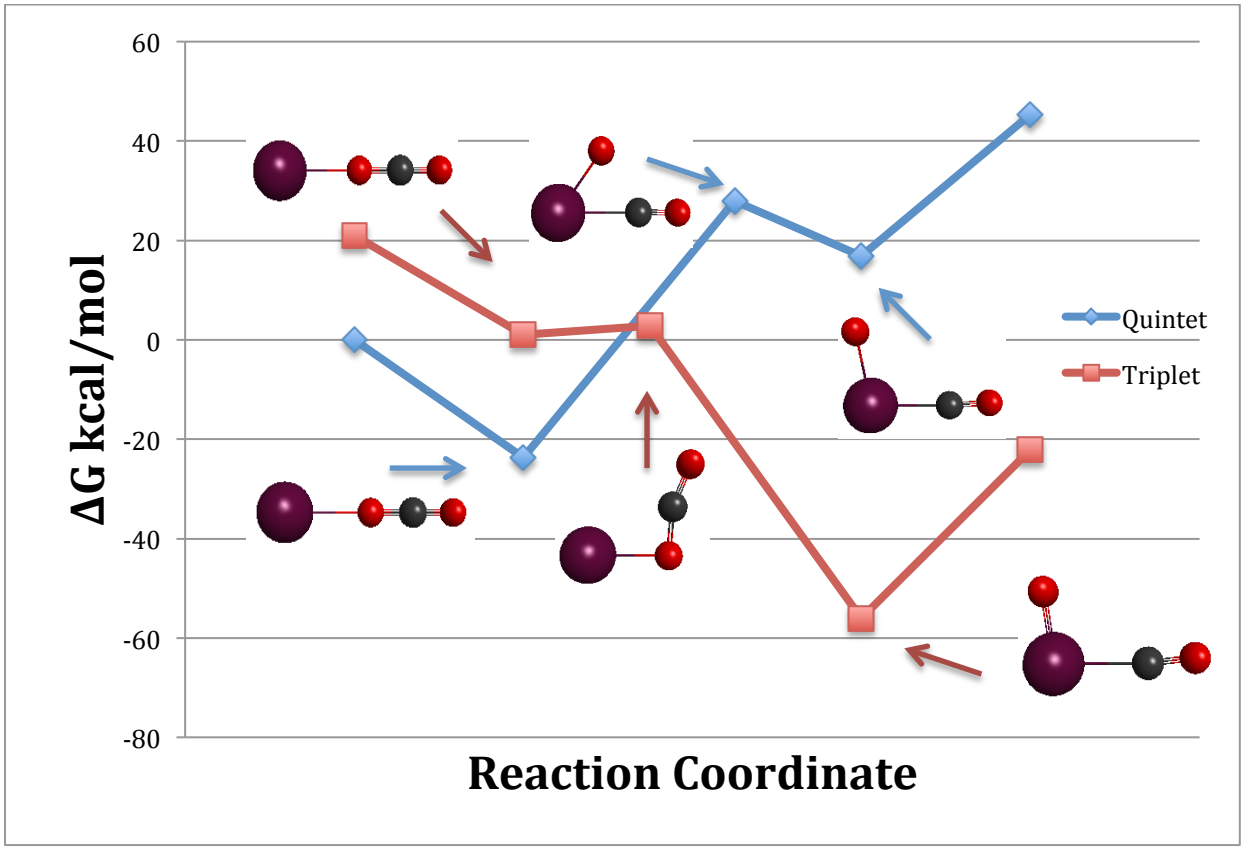

Figure 3: The DFT calculated potential energy surface points for the reaction of Nb^+ and CO_2 The red line is the adiabatic surface of the triplet spin state and the blue line is the adiabatic surface of the quintet spin state. For a given point on the reaction coordinate, the lowest energy structure between the two electronic states is shown as lower in the figure for the interior stationary points.

Table 5: DFT calculated free energies for the reaction of Nb^{x+} and CO_2. The energies are relative to the quintet (Nb^+) or quartet (Nb^{2+}) reactants. The charge transfer products are reported for the Nb^{2+} reactions and are taken to be quintet Nb^+ and CO^+ or triplet NbO^+ and CO_2^+.

ΔG_{rxn}	Nb^+		Nb^{2+}	
Species	Quintet	Triplet	Quartet	Doublet
Reactants	0.0	21.0	0.0	35.2
Reaction Side Complex	-23.7	1.0	-47.1	-37.4
Transition State	27.9	2.8	20.3	13.0
Product Side Complex	16.8	-56.0	17.7	-46.9
Products	45.3	-22.2	149.5	-12.8

Charge Transfer	ΔG_{rxn}
Nb^+ and CO_2^+	2.9
NbO^+ and CO^+	-1.7

Experimentally, reactions of the monocations with CO_2 activated a C-O bond yielding metal oxide as the major product as seen in Table 4. Reactions of Nb^+ with CO_2 yielded NbO^+ with a reaction efficiency of 47%. While NbO_2^+ has been reported by previous researchers,[28,29] it was only observed in very trace amounts and its rate constant was not measured. The efficiency of the primary reaction is consistent with that reported elsewhere[29]. Guided by these results, only the C-O bond activation ereactions were examined computationally.

It is not sufficient simply to calculate the relative energies of the products and the reactants when examining reactions of this type. It is important to calculate all stationary points along the potential energy surface for multiple spin states because at times a simple ΔG_{rxn} may indicate that the product should form, but experimentally it is not observed. The ground state reactants are a quintet Nb^+ and neutral CO_2 while the lowest energy product was calculated as a triplet NbO^+. Upon calculating the DFT stationary points on the PES for the reaction of Nb^+ and CO_2 for both quintet and triplet states, as seen in Figure 3 and Table 5, a spin crossing is seen and is probably located around the triplet transition state. The triplet transition state is only 2.8 kcal/mol higher than the reactants. In addition a single point energy of the quintet state at the triplet transition state geometry reveals that the quintet state is 12.2 kcal/mol *lower* in energy than the triplet transition state (this is only electronic energy and not free energy). Therefore, it is proposed that the barrier for the spin crossing is likely thermoneutral or possibly slightly exoergic.

Table 5 also shows the triplet product to be exoergic by 22.2 kcal/mol relative to the quintet reactants, indicating a good driving force for product formation. The probable thermoneutral reaction barrier height and the exothermic nature of the reaction would suggest that a reaction of this type should be very favorable, which agrees with the experimentally

observed results of product formation with a high reaction efficiency. Other than some slight differences in density functionals and basis sets, these calculations closely match those reported by other recent publications on this system[13,14]. NbO_2^+ being found in only very trace quantities, while seeming contradictory to previous experimental reports[10,11] is perfectly consistent with other published computational data for this reaction[13]. The MRPT2 energetics give very similar results to those of the DFT for this reaction and are available in the supporting information.

Dications

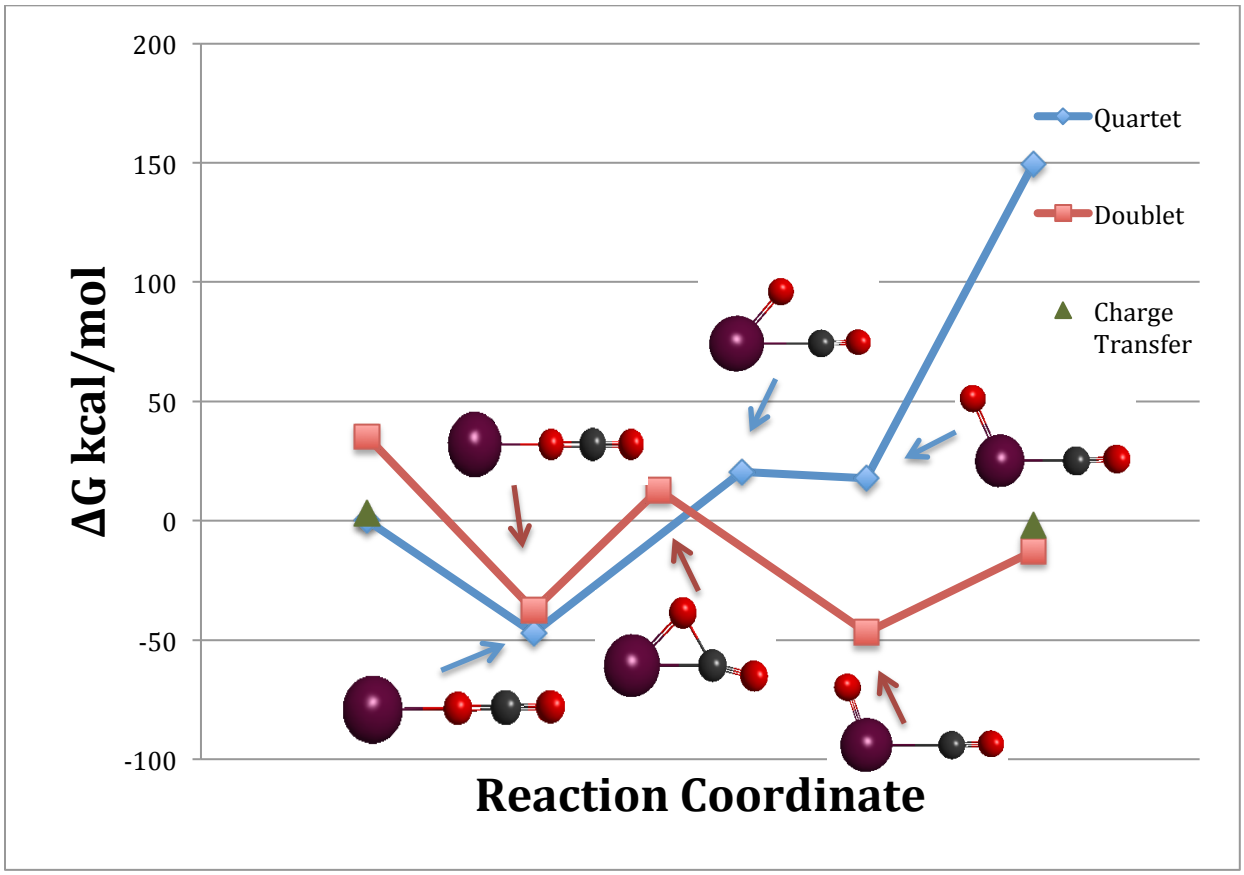

Figure 4: The DFT calculated potential energy surface for the reaction of Nb^{2+} and CO_2. The red line is the adiabatic surface of the doublet spin state and the blue line is the adiabatic surface of the quartet spin state. The green triangular points indicate the quintet Nb^+ and triplet NbO^+ charge transfer products. For a given point on the reaction coordinate, the lowest energy structure between the two electronic states is shown as lower in the figure for the interior stationary points.

Experimentally reactions of Nb^{2+} and CO_2 yield NbO^{2+} in 16% of collisions as seen in Table 4. No charge transfer products were noted experimentally. The ground state reactants are a quartet spin state Nb^{2+} and CO_2 while the lowest energy product was calculated to be the doublet NbO^{2+} and CO. As with the monocation, calculations indicate that a spin crossing occurs, most likely around the doublet transition state. The barrier height for the doublet transition state is 13.0 kcal/mol relative to the reactants as shown in Figure 4 and Table 5, which is not insignificant. A quartet single point energy at the doublet transition state geometry is 9.7 kcal/mol higher than the doublet transition state energy (again this is only electronic energy) suggesting an endoergic barrier height for the spin crossing. While the lowest energy doublet spin state product is exoergic by 12.8 kcal/mol (Table 5), the endoergic barrier height would suggest a significant impediment for the reaction. The calculations at the DFT level do not seem to provide an adequate driving force for the experimentally observed 16% reaction efficiency. The charge transfer energy was estimated by comparing the single point energies for the charge transfer complexes, which were taken to be the quintet Nb^+ and CO_2^+ on the reactant side and the triplet NbO^+ and CO^+ on the product side, relative to the ground state quartet Nb^{2+} and CO_2 reactants. The formation of both charge transfer products is essentially thermoneutral (Table 5 and Figure 4). Using the DFT model, there is no significant thermodynamic barrier for charge transfer, which contradicts the observed lack of charge transfer in the experiments.

Therefore, MCSCF and MRPT2 calculations were undertaken for the Nb^{2+} with CO_2 to explore the inconsistencies between the experiments and the calculations. For the reactants, bare Nb^{2+} was separated from CO_2 by a distance of 15 Å. A progressive energy scan of these complexes, taken by doing a single point energy calculation at various distances, deemed 15 Å

sufficient to eliminate interactions between the two species. Similarly for the products NbO^{2+} was separated from CO by 15 Å.

The reactants presented some obstacles for the calculations. Nb cations are unsaturated which creates a higher potential for degeneracy and unoccupied states in the active space. When the Nb^{2+} was combined with the CO_2 in the same active space, there were difficulties in keeping the active spaces consistent and correct between the MCSCF and MRPT2 calculations. This was especially problematic for the Nb^{2+} quartet state in the reactants. To overcome this it was necessary to either reduce the active space by eliminating some of the Nb d orbitals or to run the reactants separately as two separate calculations and add them together at that point. Fortunately, both approaches gave consistent results. For example, the Nb^{2+} doublet showed less than 1 kcal/mol difference between an all-species 15x15 MCSCF energy calculation and the energy obtained by adding an Nb^{2+} doublet with a CO_2 calculation, and the MRPT2 energy differences were similarly small. The results from the separated systems with the full active spaces are reported here.

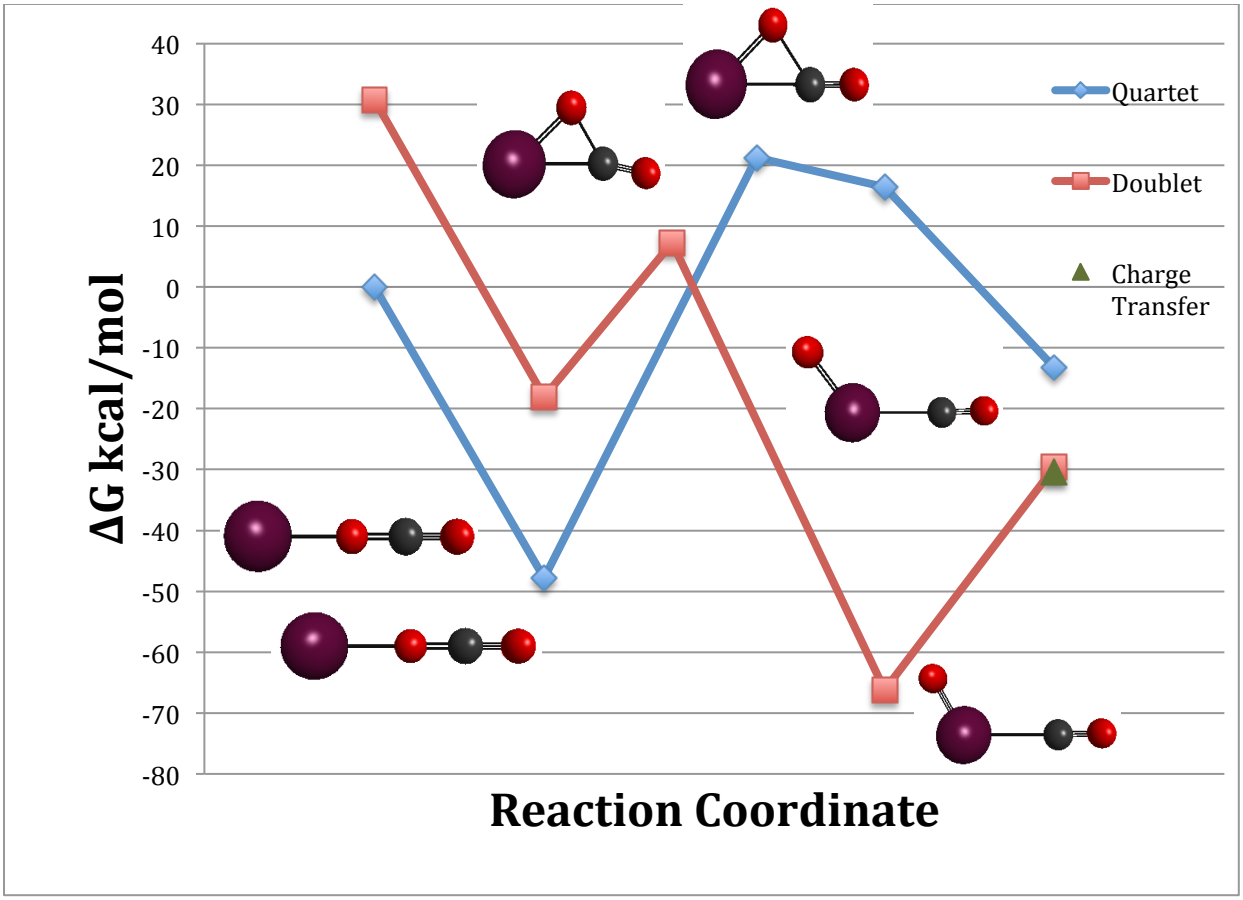

Figure 5: Graph of the MRPT2 calculated potential energy surface for the reaction of Nb^{2+} and CO_2. The red line is the adiabatic surface of the doublet spin state and the blue line is the adiabatic surface of the quartet spin state. The green triangular points indicate the triplet NbO^+ charge transfer products. For a given point on the reaction coordinate, the lowest energy structure between the two electronic states is shown as lower in the figure for the interior stationary points.

Table 6: MRPT2 calculated free energy for the reaction of Nb^{2+} and CO_2. The charge transfer products are taken to be the triplet NbO^+ and CO^+. All energies are in kcal/mol.

	ΔG_{rxn}	
Species	Quartet	Doublet
Reactants	0.0	30.7
Reactant Side Complex	-47.8	-18.1
Transition State	21.3	7.3
Product Side Complex	16.4	-66.2
Products	-13.2	-29.6

Charge Transfer	ΔG_{rxn}
NbO^+ And CO^+	-30.4

The results of the MRPT2 calculations for the quartet and doublet surfaces are given in Table 6 and Figure 5. The use of the multiconfigurational method does seem to clarify the experimental data somewhat. While the PES has the same basic shape for both calculations and the geometries did not change significantly when reoptimized with MCSCF, the energetics are more favorable for the Nb^{2+} activating the CO_2 bond for the multiconfigurational methods. Whereas the DFT indicated improbably high activation energy relative to the experimental results, the MRPT2 results reduced the barrier height for the doublet transition state, and the MRPT2 calculated products are more strongly exoergic than those calculated with DFT. As before a spin crossing occurs, likely around the doublet transition state. It is interesting to note that the doublet and quartet transition state structures are more similar geometrically than the DFT calculated structures. It is possible that the true surface crossing barrier for this reaction is very close to thermoneutral, as calculated with MRPT2. A near thermoneutral barrier height and the more strongly exoergic products are more in line with the experimentally observed reaction efficiency. As for charge transfer, on the product side the charge transfer product of the triplet NbO^+ and CO^+ has nearly identical energy as the doublet dication product. This again contradicts the lack of charge transfer products in the experiments and warrants further exploration in future work.

Conclusions

Reactions of gas phase Nb^+, Nb^{2+} with CO and CO_2 using flowing afterglow were observed and kinetic data was calculated. DFT, MCSCF and MRPT2 calculations were performed to better understand possible pathways and reaction mechanisms. Experiments reveal

that the reaction of Nb^+ with CO is slow, inefficient and yields only $Nb(CO)^+$ products. DFT calculations show that higher order clusters are very stable and and suggest their experimental absence may have to do with the inefficiency of the collisional mechanism relative to the timescale of the experiment. Higher order clusters were observed for Nb^{2+}. Reactions are faster for the metal dication than for the metal monocation, but not significantly. Computationally, while formation for higher order complexes is favorable for both mono and dications, it is much more so for dications. The combination of a higher reaction rate and the higher exothermicity may explain why higher order complexes were seen with the dication but not the monocation.

Reactions of Nb^+ and Nb^{2+} with CO_2 effectively activate the C-O bond, resulting in metal oxide formation. Reactions of the monocation were more efficient and the DFT calculated PES predicts a near thermoneutral activation energy and exothermic products, which supports the observed experimental efficiency. The dication, while activating the C-O bond, was much less efficient. MRPT2 calculations indicated a near thermoneutral barrier height (although higher than that for the monocation) and exoergic products for this reaction, modifying the DFT resutls. The difference in the energies of the barriers and the products could explain the differences in efficiency for the mono and dication reactions. No charge transfer was experimentally observed in the dication reaction, while computation suggests that there should be. The question of charge transfer deserves further investigation.

Acknowledgements

This material is based upon work supported by the National Science Foundation under Grant No. OISE-0730114 for the Partnerships in International Research and Education (PIRE) and also by support to TLW by the U.S. Department of Energy, Office of Basic Energy Sciences,

Division of Chemical Sciences, Geosciences, and Biosciences through the Ames Laboratory Chemical Physics project. The Ames Laboratory is operated for the U.S. Department of Energy by Iowa State University under Contract No. DE-AC02-07CH11358. This research was also supported by an allocation of advance computing resources provided by the National Science Foundation. The computations were performed on Kraken at the National Institute for Computational Sciences.

Supporting Information Available: All geometries and energies at various levels of theory are included. This material is available free of charge via the Internet at http://pubs.acs.org.

References

(1) Ferguson, E. E.; Fehsenfeld, F. C.; Schmeltekopf, A. L., Flowing Afterglow Measurements of Ion-Neutral Reactions. *Adv. At. Mol. Phys.* **1969**, *5*, 1-56.

(2) Oliva, M.; Safont, V. S.; Andre´s, J.; Tapia, O., Transition State Structures and Intermediates Modeling Carboxylation Reactions Catalyzed by Rubisco. A Quantum Chemical Study of the Role of Magnesium and Its Coordination Sphere. *J. Phys. Chem. A* **2001**, *105*, 9243-9251.

(3) Spreitzer, R. J., Genetic Dissection of Rubisco Structure and Function. *Annual Rev. Plant Physiol. Plant Mol. Biol.* **1993**, *44*, 411-434.

(4) Khoo, H. H. T., Reginald B. H, Environmental Impact Evaluation of Conventional Fossil Fuel Production (Oil and Natural Gas) and Enhanced Resource Recovery with Potential CO2 Sequestration. . *Energy Fuels* **2006**, *20*, 1914-1924.

(5) Yu, H. Z., Guangzhu; Fan, Weitang; Ye, Jianping., Predicted CO2 enhanced coalbed methane recovery and CO2 sequestration in China. *Int. J. Coal Geol.* **2007**, *71*, 345-357.

(6) D. Golomb , S. P., D . Ryan, E. Barry, P. Swett, Ocean Sequestration of Carbon Dioxide: Modeling the Deep Ocean Release of a Dense Emulsion of Liquid CO2-in-Water Stabilized by Pulverized Limestone Particles. *Environ. Sci. Technol.* **2007**, *41*, 4698-4704.

(7) Behr, A. *Carbon Dioxide Activation by Metal Complexes*; VCH: New York, 1998.

(8) Pickett, C. J.; Vincent, K. A.; Ibrahim, S. K.; Gormal, C. A.; Smith, B. E.; Fairhurst, S. A.; Best, S. P., Synergic binding of carbon monoxide and cyanide to the FeMo cofactor of nitrogenase: Relic chemistry of an ancient enzyme? *Chem. Eur. J.* **2004**, *10*, 4770-4776.

(9) Heo, J. S., C. R.; Ludden, P. W., Redox-Dependent CO2 Reduction Activity of CO Dehydrogenase from Rhodospirillum rubrum. *Biochemistry* **2001**, *40*, 7604-7611.

(10) Koyanagi, G. K.; Bohme, D. K., Gas-Phase Reactions of Carbon Dioxide with Atomic Transition-Metal and Main-Group Cations: Room-Temperature Kinetics and Periodicities in Reactivity. *J. Phys. Chem. A* **2005**, *110*, 1232-1241.

(11) Sievers, M. R.; Armentrout, P. B., Gas phase activation of carbon dioxide by niobium and niobium monoxide cations. *Int. J. Mass spectrom.* **1998**, *179/180*, 103-115.

(12) Wang, Y.-C.; Yang, X.-y.; Geng, Z.-Y.; Lui, Z.-Y., Theoretical study of carbon dioxide-carbon monoxide convesion by La+, Hf+ and Ta+. *Chem. Phys. Lett.* **2006**, *431*, 39-44.

(13) Tommaso, S. D.; Marino, T.; Rondinelli, F.; Russo, N.; Toscano, M., CO2 Activation by Nb+ and NbO+ in the Gas Phase. A Case of Two-State Reactivity Process. *J. Chem. Theory Comput.* **2007**, *3*, 811-815.

(14) Han, D.-M.; Dai, G.-L.; Chen, H.; Wang, Y.; Zhong, A.-G.; Lin, C.-P.; Chen, D., Theoretical Study on the Reactions of Nb and Nb+ with CO2 in the Gas Phase. *Int. J. Quantum Chem* **2011**, *111*, 2898-2909.

(15) Herman, J.; Foutch, J. D.; Davico, G. E., Gas-Phase Reactivity of Selected Transition Metal Cations with CO and CO2 and the Formation of Metal Dications Using a Sputter Ion Source *J. Phys. Chem. A* **2007**, *111*, 2461-2468.

(16) Bierbaum, V. M.; DePuy, C. H.; Shapiro, R. H.; Stewart, J. H., Flowing afterglow studies of the reactions of hydroxide, amide, and methoxide ions with ethylene oxide and propylene oxide. *J. Am. Chem. Soc.* **1976**, *98*, 4229-4235.

(17) Ho, J.; Ervin, K. M.; Lineberger, W. C., Photoelectron spectroscopy of metal cluster anions: Cu/sub n//sup -/, Ag/sub n//sup -/, and Au/sub n//sup -/. *J. Chem. Phys.* **1990**, *93*, 6987-7002.

(18) Ho, J. Negative Ion Laser Photoelectron Spectroscopy of Mass Selected Small Metal Clusters. Ph.D. Thesis, University of Colorado, 1991.

(19) Valiev, M.; Bylaska, E. J.; Govind, N.; Kowalski, K.; Straatsma, T. P.; Van Dam, H. J. J.; Wang, D.; Nieplocha, J.; Apra, E.; Windus, T. L.; de Jong, W. A., NWChem: A comprehensive and scalable open-source solution for large scale molecular simulations. *Comput. Phys. Commun.* **2010**, *181*, 1477-1489.

(20) Becke, A. D., Density-functional thermochemistry. III. The role of exact exchange. *J. Chem. Phys.* **1993**, *98*, 5648-5652.

(21) Becke, A. D., Density-functional thermochemistry. I. The effect of the exchange-only gradient correction. *J. Chem. Phys.* **1992**, *96*, 2155-2160.

(22) Hay, P. J.; Wadt, W. R., Ab initio effective core potentials for molecular calculations. Potentials for the transition metal atoms scandium to mercury. *J. Chem. Phys.* **1985**, *82*, 270-283.

(23) Krishnan, R.; Binkley, J. S.; Seeger, R.; Pople, J. A., Self-consistent molecular orbital methods. XX. A basis set for correlated wave functions. *J. Chem. Phys.* **1980**, *72*, 650-654.

(24) Cheung, L. M.; Sundberg, K. R.; Ruedenberg, K., Dimerization of carbene to ethylene. *J. Am. Chem. Soc.* **1978**, *100*, 8024-8025.

(25) Cheung, L. M.; Sundberg, K. R.; Ruedenberg, K., Electronic rearrangements during chemical reactions. II. Planar dissociation of ethylene. *International Journal of Quantum Chemistry* **1979**, *16*, 1103-1139.

(26) Ruedenberg K, S. M., Gilbert MM, Elbert ST, Are Atoms Intrinsic to Molecular Electronic Wave Functions? I. The FORS Model. *Chem. Phys.* **1982**, *71*, 41–49.

(27) Ruedenberg, K.; Schmidt, M. W.; Gilbert, M. M., Are atoms sic to molecular electronic wavefunctions? II. Analysis of fors orbitals. *Chem. Phys.* **1982**, *71*, 51-64.

(28) Ruedenberg, K.; Schmidt, M. W.; Gilbert, M. M.; Elbert, S. T., Are atoms intrinsic to molecular electronic wavefunctions? III. Analysis of FORS configurations. *Chem. Phys.* **1982**, *71*, 65-78.

(29) Feller, D. F.; Schmidt, M. W.; Ruedenberg, K., Concerted dihydrogen exchange between ethane and ethylene. SCF and FORS calculations of the barrier. *J. Am. Chem. Soc.* **1982**, *104*, 960-967.

(30) Roos, B. O. The Complete Active Space Self-Consistent Field Method and its Applications in Electronic Structure Calculations. In *Advances in Chemical Physics*; John Wiley & Sons, Inc., 1987; Vol. 69; pp 399-445.

(31) Roos, B. O. *Lecture Notes in Quantum Chemistry*; Springer-Verlag: Berlin, 1992.

(32) Roos, B. O.; Taylor, P. R.; Si≐gbahn, P. E. M., A complete active space SCF method (CASSCF) using a density matrix formulated super-CI approach. *Chem. Phys.* **1980**, *48*, 157-173.

(33) Siegbahn PEM, A. f. J., Heiberg A, Roos BO, The complete active space SCF (CASSCF) method in a Newton–Raphson formulation with application to the HNO molecule. *J. Chem. Phys.* **1981**, *74*, 2384-2396.

(34) Andersson, K.; Malmqvist, P-A.; Roos, B. O.; Sadlej, A. J.; Wolinski, K., Second-order perturbation theory with a CASSCF reference function. *J. Phys. Chem.* **1990**, *94*, 5483-5488.

(35) Andersson, K.; Malmqvist, P-A.; Roos, B.O., Second-order perturbation theory with a complete active space self-consistent field reference function. *J. Chem. Phys.* **1992**, *96*, 1218-1226.

(36) Andersson, K., Different forms of the zeroth-order Hamiltonian in second-order perturbation theory with a complete active space self-consistent field reference function. *Theor. Chim. Acta* **1995**, *91*, 31-46.

(37) Werner, H.-J., Third-order multireference perturbation theory The CASPT3 method. *Mol. Phys.* **1996**, *89*, 645-661.

(38) Schmidt, M. W.; Baldridge, K. K.; Boatz, J. A.; Elbert, S. T.; Gordon, M. S.; Jensen, J. H.; Koseki, S.; Matsunaga, N.; Nguyen, K. A.; Su, S.; Windus, T. L.; Dupuis, M.; Jr, J. A. M., General atomic and molecular electronic structure system. *J. Comput. Chem.* **1993**, *14*, 1347−1363.

(39) Gordon, M. S.; Schmidt, M. W. *Theory and Applications of Computational Chemistry: The First Forty Years*; Elsevier: The Netherlands, 2005.

(40) Kendall, R. A.; Dunning, T. H.; Harrison, R. J., Electron affinities of the first-row atoms revisited. Systematic basis sets and wave functions. *J. Chem. Phys.* **1992**, *96*, 6796-6806.

(41) Su, T.; Chesnavich, W. J., Parametrization of the ion-polar molecule collision rate constant by trajectory calculations. *J. Chem. Phys.* **1982**, *76*, 5183-5185.

CHAPTER 4:REACTIONS OF TANTALUM MONO AND DICATIONS WITH CO AND CO_2

Emily Hull[*], Gustavo E. Davico[+], Theresa L. Windus[*]

[*]Department of Chemistry and Ames Laboratory USDOE, Iowa State University, Ames, Iowa 50011, USA

[+]Deceased

Abstract

Tantalum mono and dications were created and reacted with CO and CO_2 in a flowing afterglow instrument. Stationary points on the Potential Energy Surfaces (PES) for the reactions were calculated using Density Functional Theory (DFT) and Multi-Reference Perturbation Theory (MRPT2). Ta mono and dications react with CO in clustering reactions. Only the mono cluster, $Ta(CO)^+$, was observed for monocations, but higher order clusters with additional CO molecules were observed for dications. DFT calculations indicate no significant barrier to the formation of higher order products, and their absence in the monocation reactions may be more due to the relative inefficiency of the monocation reactions compared to the dication reactions. Reactions of Ta cations with CO_2 activate the C-O bond to form the metal oxide and carbon monoxide. DFT and MRPT2 calculated PES for these reactions show no significant barrier for activation of the C-O bond in CO_2 and the dication products are thermodynamically more stable than the monocation products, which is consistent with experimental reaction efficiencies. Charge transfer reactions were also noted for Ta^{2+} reactions with CO_2.

Introduction

Because of its increasing importance, artificial carbon sequestration is a field of active and ongoing research[1-3]. Due to transition metal's nature and ability to change electronic configuration, to "donate" electrons as an example, the study of C-O activation in CO_2 and its applications for carbon sequestration[4] would be incomplete without considering the possible applications of transition metal species to the problem.

The chemistry of transition metals and carbon monoxide is also interesting. Transition metals are curiously present at the active site of many metalloproteins, and are often required for enzymatic activity[5]. The Ni-Fe-S containing nitrogen dehydrogenase metalloprotein found in *Rhodospirillum Rubrum*[6] is an example of a metalloprotein that requires CO for activity. This molecule facilitates the reversible oxidation of CO to CO_2, which can then be used by the plant to produce simple sugars. This, and other metalloproteins that show CO activity, may be examples of something dubbed as "relic" chemistry, the absolute origin of which may be outer space. When supernovas spew heavy metal ions across space, the building blocks for life are produced and chemistry begins. Metal ions and organic molecules have been observed in interstellar dust clouds[7,8], and ion-molecule chemistry taking place there has been documented[9]. Studying gas-phase reactions of metals with CO could further our understanding of the presence of metals in organic systems and the possibility of finding these specific compounds in extraterrestrial bodies.

Previous experimental and computational studies on Ta^+ reactions with CO and CO_2 have been reported[10,11].. This paper adds to the body of knowledge by exploring these reactions with different experimental and computational methods than have previously been used, and examining the reactions of Ta^{2+}. A previously published study from this group[12] presented data

that V^+ reacting with CO and CO_2 resulted in clustering for both gases, but no activation of the C-O bond in CO_2. This paper furthers the understanding of the chemistry for group 5 elements by specifically focusing on tantalum.

Materials and Methods

A flowing afterglow instrument was used to study the gas-phase transition metal reactions presented below[13,14]. The experimental setup is nearly identical to that used in our previous study[12] and the purities of the argon, helium, carbon dioxide and tantalum used where 99.95%, 99.95%, 99.99%, 99.0% and 99.8% respectively. Pseudo first order conditions were maintained. The statistical methods used to determine the reaction rates at 298±2 K were previously reported[12]. The experiments were run in triplicate and the reported errors are either one standard deviation of the final rate constant value or the fitting procedure whichever is greater.

DFT calculations were performed with the NWChem[15] suite of programs using the UDFT methodology for open shell systems with the B3LYP[16,17] functional and corrects to obtain the Gibbs Free energy were calculated at a temperature of 298K. Basis sets used for the DFT calculations were the LANL2dz ECP[18] and associated valence basis set for Ta and 6-311+G* Pople[19] basis set was used for C and O. Tight grid converge criteria was used for the geometry optimization and Hessians were calculated to ascertain whether a structure was a minimum, a transition state, or a higher order saddle point.

For reactions of Ta^+ and CO_2 where DFT calculations were deemed insufficient to explain the experimental data, MCSCF[20-29] and MRPT2[30-33] calculations were performed using

the GAMESS[34,35] suite of computational chemistry programs. While all-electron basis sets would have been preferable for MCSCF and MRPT2 calculations, for the sake of computational efficiency LANL2TZf ECP[18] and the associated valence basis set was used for Ta and aug-cc-pVTZ[36] was used for the C and O atoms. DFT optimized geometries were re-optimized at the MCSCF level. If the size of the active space made calculating the Hessian prohibitively expensive, the active space was reduce for the sake of performing the computation and the zero-point-energy (ZPE) of the smaller active space was used. To ensure the validity of this approximation the zero-point energies of the MCSCF and DFT calculations were compared and found to be similar.

A consistent active space of 16 electrons in 15 orbitals was maintained for all reaction coordinates on the PES. On the reactant side (reactants and reaction side complex) this consisted of a complete 12 electron in 10 orbital complete valence space of CO_2, and 4 electrons in 5 d orbitals for the Ta^+. The products and product side complex active space contains the 6 orbital in 6 electron valence space of CO plus an additional carbon 2s orbital for a total of 8 electrons in 7 orbitals combined with a TaO^+ space which contained all Ta-O bonding and anti-bonding orbitals and Ta non-bonding singly occupied orbitals, an 8 electron in 8 orbital space, for a total of 16 electrons in 15 orbitals. The transition state active space is more difficult and was constructed from an ROHF calculation on the optimized DFT orbitals to contain all of the Ta-C bonding and anti-bonding, all Ta-O bonding and anti-bonding and any non-bonding Ta singly occupied orbitals and was also maintained at 16 electrons in 15 orbitals.

The process of complexation involves multiple reactants going to a single product. The overall entropy of the system is reducing and the magnitude of the change increases with the size of the complex. The Gibbs Free Energy of complexation, difined as $\Delta G_{complexation} = \Sigma \Delta G_{products}$ -

$\Sigma\Delta G_{reactants,}$ gives a better understanding whether or not and why complexation occurs. For bond breaking and forming reactions with a constant number of reactants going to a constant number of products, only enthalpy is calculated.

Results and Discussion

Reactions of Metals with CO

Reactions of Ta^{x+} (x = 1 or 2) with CO in the gas phase is a three body problem. In any collision between the Ta^{x+} and the CO there is a competition between the free energy of complexation and the kinetic energy of the collision. In order for the kinetic energy of collision to transfer to internal energy and allow complexation to occur, collision with a third body, such as the buffer gas, is needed for collisional deactivation and stabilization. For visualization purposes, imagine a Ta^{x+} colliding with a CO. If the two molecules were billiards on a table, the first inclination of colliding bodies is to continue moving in opposite directions of the collision. If a third billiard ball, the carrier gas, strikes nearly instantaneously with the Ta^{x+} and CO collision, the balls are much more likely to stick together so to speak. Once the mono-complex $Ta(CO)^{x+}$ has been formed in this way, additional collisions with CO can result in the formation of higher order complexes, $Ta(CO)_n^{x+}$. Gas-phase complexation reactions are therefore a stepwise process with the formation of the mono-complex being the primary reaction product and rate-limiting step. Because the sequential addition of each CO spreads the complexation energy over more degrees of freedom, it is expected that if the formation of the monocomplex is observed and favorable, higher order complexes ($n \geq 2$) should also be favorable. Limits to this sequential addition are determined by such factors as steric hindrance, or internal electronic

reorganizations needed to undergo a spin crossing, meaning that addition of CO to the Ta^{x+} is not infinite.

Monocations

Table 1: Experimental results of the reactions of Nb^{x+} with CO. NR = no reactions and NC = not calculated.

Metal	Rate[a]	Product	Eff[b]	Secondary product	Rate	kcol CO
Ta^+	$<8 \times 10^{-14}$	$TaCO^+$	<0.0001	NR	NC	6.86×10^{-10}
Ta^{2+}	$1.97 \pm 0.05 \times 10^{-12}$	$Ta(CO)_6^{2+}$ [40]	0.0014	$Ta(CO)_6^{2+}$	NC	1.37×10^{-9}
		Ta^+ [60]				

[a] Observed rate constant, k_{obs}, in units of cm^3 $molecules^{-1}s^{-1}$ [b] Reaction efficiency, k_{obs}/k_{col} where the rate of collision, k_{col} ,is calculated according to literature[37] Even though $Ta(CO)_6^{2+}$ was the only observed complexation product, as reported in the table, it is technically a secondary product and is also reported as such.

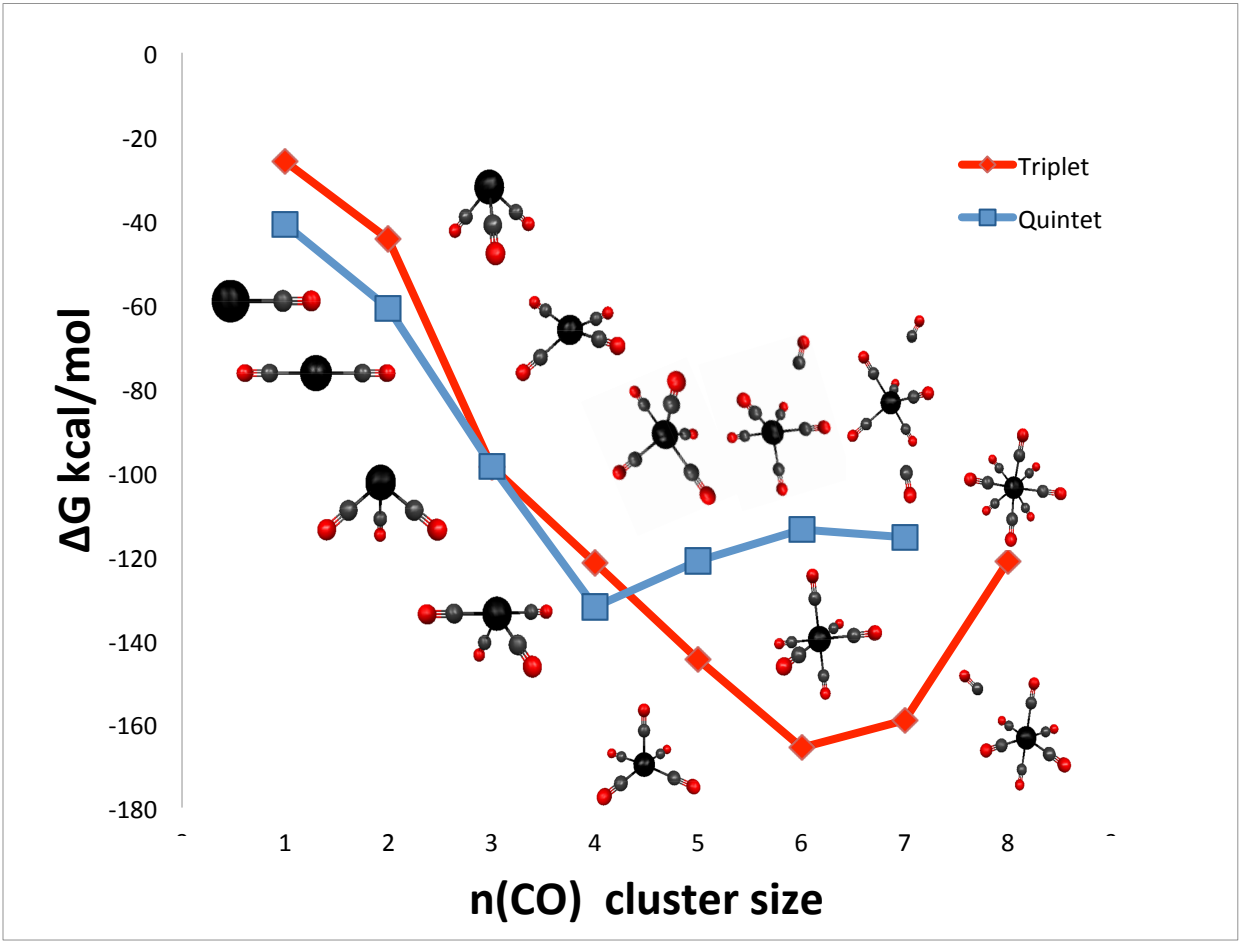

Figure 1: DFT calculated Gibbs Free Energy of complexation for each of the potential products of the reaction of Ta^+ and nCO. The red points represent the triplet spin states and the blue

(continued from previous page) points are the quintet spin states. The lowest energy structure is shown for each of the two electronic states with the lowest energy structure placed below the higher energy structure for each complex with n COs. The large black spheres are the Ta, small black spheres are C and the red spheres are O. The same coloring is used for all figures throughout this work. Structures are nearly identical for the quintet and triplet $Ta(CO)^+$ and $Ta(CO)_2^+$, so only the quintet structure is shown. The dissociated triplet $Ta(CO)_7^+$ structure is shown next to it's point on the PES and below the association triplet $Ta(CO)_8^+$.

Table 2: DFT calculated Gibbs Free Energy (ΔG) of complexation for the reactions of Ta^+ and CO where $\Delta G_{complexation} = \Sigma\Delta G_{products} - \Sigma\Delta G_{reactants}$ [a]per CO complexation energy defined as the free energy difference between $Ta^{x+}(CO)_n$ and $Ta^{x+}(CO)_{n-1}$ All Energies are in kcal/mol.

	ΔG_{rxn}		Complexation[a]	
Species	Quintet	Triplet	Quintet	Triplet
$Ta(CO)_1^+$	-40.9	-26.0	-40.9	-26.0
$Ta(CO)_2^+$	-60.9	-44.4	-20.0	-18.4
$Ta(CO)_3^+$	-98.6	-98.7	-37.8	-54.3
$Ta(CO)_4^+$	-132.1	-121.7	-33.5	-23.0
$Ta(CO)_5^+$	-121.1	-144.7	11.0	-23.0
$Ta(CO)_6^+$	-113.8	-165.7	7.4	-21.0
$Ta(CO)_7^+$	-115.5	-159.1	-1.7	6.6
$Ta(CO)_8^+$	***	-121.4	***	37.8

Experimental products observed for the reactions of Ta^+ and CO are given in Table 1 show that only the monocluster $Ta(CO)_n^+$ was found. The ground quintet and first excited state triplet Ta^+ for complexation reactions with CO were calculated with DFT. The results are plotted in Figure 1 and the numerical values shown in Table 2. The ΔG of the mono cluster is favorable with a calculated ΔG_{rxn} of -41 kcal/mol. The calculations also indicate that the formation of higher order complexes, while not observed experimentally, is favorable.

An interesting feature of the calculations reported in Figure 1 and table 2 is a probable spin crossing occurring around $Ta(CO)_3^+$. This indicates that should complexes of $Ta(CO)_3^+$ form, they are likely to be in the triplet spin state. On the quintet adiabatic surface, the limit of

complexation appears to be $Ta(CO)_5^+$ and any additional CO associates at a distance too great for bonding. The triplet adiabatic surface reaches a similar complexation limit at n=6. While an n=8 complex was found with all CO coordinated to the Ta^+ center, the complex is significantly higher in energy than the n=6 complex, and the n=7 complex shows dissociation of the 7th CO from the Ta^+ center. Since the reaction mechanism is stepwise, the n=8, while theoretically possible, is extremely unlikely.

Dications

The only experimentally observed complexation product, as reported in Table 1, for the reactions of Ta^{2+} with CO was $Ta(CO)_6^{2+}$. The formation of charge transfer product Ta^+ was also observed and, as shown by the branching ratios reported in Table 1, is the dominant overall reaction. Due to the nature of the previously explained collisional mechanism, $Ta(CO)_6^{2+}$ is, by definition, a secondary product. However, as it was the only complexation product detected, it is listed in Table 1 both as the primary and secondary product. DFT calculations on the quartet and doublet spin states of Ta^{2+} reacting with CO were performed and the results are reported in Table 3 and Figure 2. The quartet and double states are very close in energy and have fairly exoergic per-carbonyl complex energies. For the quartet adiabatic surface the limit of complexation appears to be $Ta(CO)_6^{2+}$ and calculations to find a $Ta(CO)_7^{2+}$ structure found that the 7th CO is added at too far a distance for direct coordination with the Ta center. The limit of complexation for the adiabatic doublet surface is predicted to be $Ta(CO)_7^{2+}$. While a $Ta(CO)_8^{2+}$ structure was fond with all COs coordinated to the Ta center, it was higher in energy than the n=7 cluster. The n=9 cluster is actually an n=7 cluster with 2 additional CO molecules interacting at too far a distance for direct complexation with the Ta center. The experimental results in Table 1 only observed formation of the $Ta(CO)_6^{2+}$. This is consistent with the computational data which

indicates that in addition to no significant energy gain going from $Ta(CO)_6^{2+}$ to $Ta(CO)_7^{2+}$ a spin crossing also occurs requiring internal electronic reorganization to go from a quartet $Ta(CO)_6^{2+}$ to a doublet $Ta(CO)_7^{2+}$.

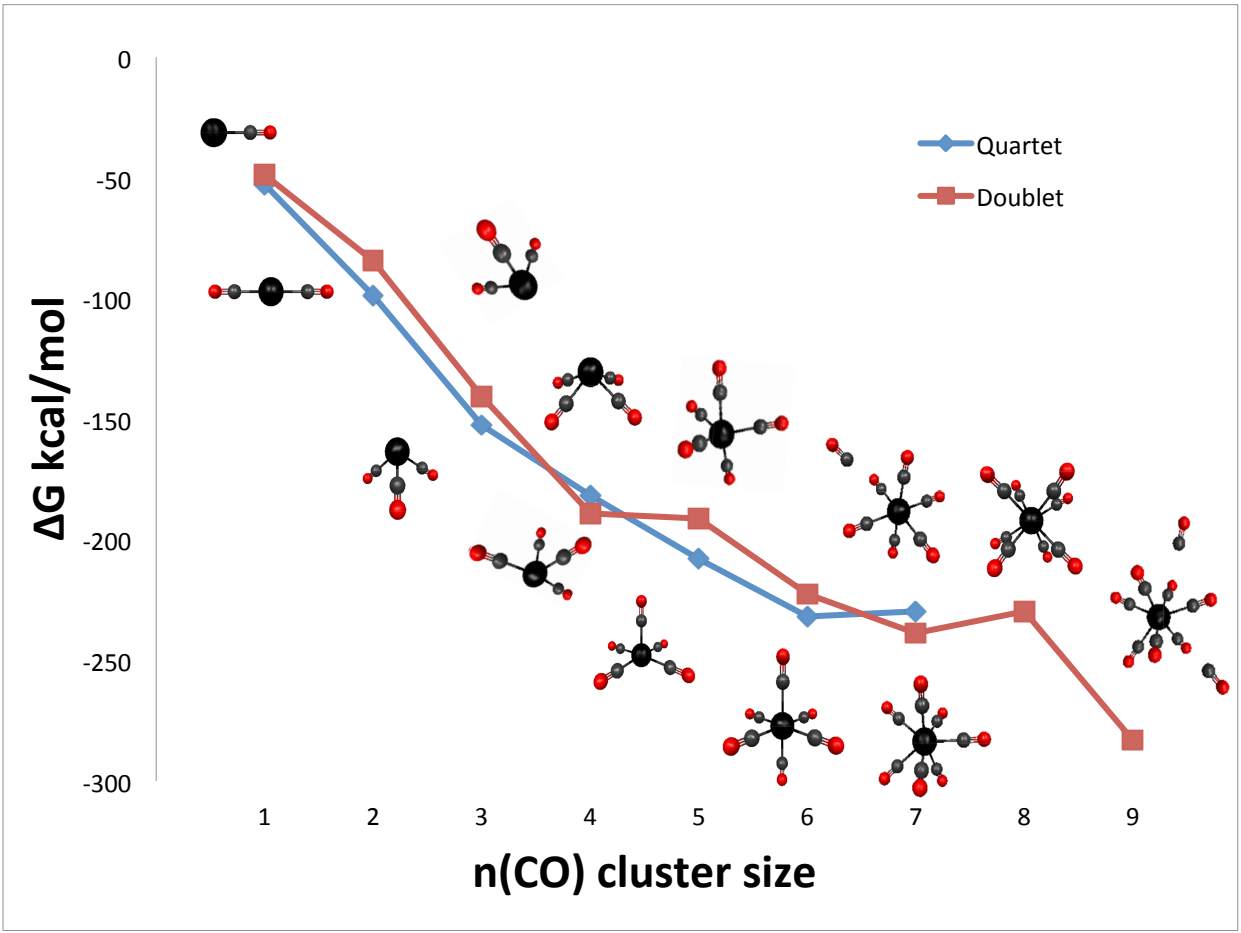

Figure 2: DFT calculated ΔG for each of the potential products of the reaction of Ta^{2+} and nCO. The red points represent the quartet spin states and the blue points the doublet spin states. The lowest energy structure is shown for each of the two electronic states with the lowest energy structure placed below the higher energy structure for each complex with n COs. Structures are nearly identical for the quartet and doublet $Ta(CO)^+$,$Ta(CO)_2^+$ and $Ta(CO)_6^+$ complexes, so only the quartet structure is shown. The dissociated quartet $Ta(CO)_7^+$ structure is shown above that of the doublet structure.

Table 3: DFT calculated Gibbs Free Energy (ΔG) of complexation for the reactions of Ta^{2+} and CO where $\Delta G_{complexation} = \Sigma\Delta G_{products} - \Sigma\Delta G_{reactants}$ [a]per CO complexation energy defined as the free energy difference between $Ta^{x+}(CO)_n$ and $Ta^{x+}(CO)_{n-1}$ All Energies are in kcal/mol

	ΔG_{rxn}		Complexation[a]	
Species	Quartet	Doublet	Quartet	Doublet
$Ta(CO)_1^{2+}$	-52.9	-48.8	-52.9	-48.8
$Ta(CO)_2^{2+}$	-98.7	-84.4	-45.8	-35.6
$Ta(CO)_3^{2+}$	-152.4	-140.6	-53.7	-56.1
$Ta(CO)_4^{2+}$	-181.6	-189.0	-29.2	-48.5
$Ta(CO)5^{2+}$	-208.0	-191.2	-26.3	-2.2
$Ta(CO)_6^{2+}$	-231.8	-222.6	-23.9	-31.4
$Ta(CO)_7^{2+}$	-229.7	-238.8	2.2	-16.2
$Ta(CO)_8^{2+}$	***	-229.6	***	9.2
$Ta(CO)_9^{2+}$	***	-282.9	***	-53.3

Overall the calculations reported above predict that the complexation limit should be $Ta(CO)_6^{x+}$ for both the mono and dication as no calculated impediment to forming these higher order complexes was found. Experimental results presented in Table 1 match this prediction for the dication, but only the mono complex was observed for reactions with Ta^+. As the addition of a second CO to $Ta\text{-}CO^+$ is predicted to be exothermic by an additional nearly 20 kcal/mol, the collisional mechanism itself should be no impediment as there would be significant energy gain for forming the n=2 complex in the event of a collisional event with the mono complex. The difference between the mono and dication reactions may have more to do with the overall reaction efficiency. The dication, by nature of it's double charge, showed more than an order of magnitude higher reaction rate than the monocation which means that overall more collisions were occurring with Ta^{2+} than Ta^+. It is therefore possible that while higher order complexes could form for reactions of Ta^+ with CO, they were not formed or observed on the timescale of the experiment.

Reactions with CO_2

Reactions of Ta^{x+} with CO_2 have the potential to either form simple complexes, as with CO, or to activate the C-O bond. Should the Ta^{x+} activate the C-O bond, there are several possible reaction products.

$Ta^{x+} + CO_2 \rightarrow TaO^{x+} + CO \quad x=1,2 \quad$ primary (1)

In the case of dication reaction,s another primary product can be charge transfer:

$Ta^{2+} + CO_2 \rightarrow Ta^{+} + CO_2^{+}$ primary (2)

$Ta^{2+} + CO_2 \rightarrow TaO^{+} + CO^{+}$ primary (3)

If Ta^{+} is formed in charge transfer, it can potentially go on to react with CO_2 to create TaO^{+} as a secondary product

$Ta^{+} + CO_2 \rightarrow TaO^{+} + CO$ secondary (4)

There are five main reaction coordinates for the Potential Energy Surface (PES) in an ion-neutral reaction. These coordinates are the reactants, reactant side complex, transition state, product side complex, and products. The reactants are obviously the individual reactants, in this case CO_2 and Ta^{x+} separated at infinite distance. As the neutral approaches the metal ion, electrostatic interactions begin to occur and the reaction-side complex forms (Ta^{x+} --- O-C-O). The reaction side complex is essentially the same as the complexation reported above for the reactions with CO. Those simple electrostatic interactions can be compelled into a full transition state (O-Ta-C-O). As that transition state dissociates towards the products, the product side complex where the charged products are electrostatically attracted, but not strongly bonded, appears $(O\text{-}Ta \text{ --- } C\text{-}O)^{x+}$.

In the case of charge transfer, this modeling of the reaction coordinates means charge transfer products can appear either on the reactant or product side of the reaction. On the reactant side, charge transfer occurs via reaction (2) and on the product side by reaction (3). Experimentally, there is no way to distinguish between primary reaction (3) and secondary reaction (4).

Breaking the charge transfer into its component pieces leads to the following set of reactions.

$$Ta^{2+} + e^- \rightarrow Ta^+ \quad (5)$$
$$CO_2 \rightarrow CO_2^+ + e^- \quad (6)$$
$$Ta^{2+} + CO_2 \rightarrow Ta^+ + CO_2^+ \quad (7)$$

To better understand the possibility of charge transfer reaction 7, DFT calculations were performed and compared for reactions 5 and 6, above. There is no experimental data for the ionization of Ta^+ to Ta^{2+}, so in this case only calculated data can be compared. The reduction potential of CO_2 was examined by using the orbital energy of the highest occupied molecular orbital as an estimate of ionization energy (Koopman's Theorem[38]) and by comparing the calculated enthalpy and free energy for the ionization of CO_2, and conversely the reduction of Ta^{2+}. The results are shown in the table 4.

Table 4: Comparison of calculated enthalpies, free energies and Koopman's Theorem (KT) energies for charge transfer reactions between Ta^{2+} and CO_2. All energies are in kcal/mol. Reactions 5 and 6 (row 1 and 2) sum to reaction 7, shown in row 3.

Reaction	ΔH	ΔG	KT
$Ta^{2+} + e^- \rightarrow Ta^+$	-352.0	-352.0	-307.4
$CO_2 \rightarrow CO_2^+ + e^-$	336.2	336.1	242.2
$Ta^{2+} + CO_2 \rightarrow Ta^+ + CO_2^+$	-15.8	-15.9	-65.1

It can be seen in table 4 that there is no impediment to charge transfer between these bodies. While the calculated enthalpies and free energies presented in table 4 are very similar, there is a large difference between those values and the Koopmans Theorem value. Application of Koopman's Theorem to DFT is problematic.[39-43] The difference between the true ionization energy and that estimated by the DFT extension of Koopman's theorem varies with the exchange correlation functional and has been found[44] to range between 0.3-30 eV. Examining the enthalpy, the energy required to go from CO_2 to CO_2^+ is less than the energy gained by reducing Ta^{2+} to Ta^+, which is a difference in favor of reducing the Ta^{2+}.

Monocations

Table 5: Experimental results of the reactions of Ta^{x+} with CO.

Metal	Rate[a]	Product	Eff[b]	Secondary product	rate	k_{col} CO_2
Ta^+	$2.47 \pm 0.03 \times 10^{-10}$	TaO^+	0.37	TaO_2^+	NC	6.72×10^{-10}
Ta^{2+}	$6.4 \pm 0.4 \times 10^{-10}$	TaO^{2+} [70]	0.48	$TaO(Ar)^{2+}$	NC	1.34×10^{-9}
		Ta^+ [30]		TaO^+, TaO_2^+		

[a] Observed rate constant, k_{obs}, in units cm^3 $molecules^{-1}s^{-1}$ [b] Reaction efficiency, k_{obs}/k_{col}.where the rate of collision, k_{col} ,is calculated according to the literature.[37]

The experimental results of the reactions of Ta^+ and CO_2 are given in Table 5. They show that Ta^+ activated the C-O bond to yield TaO^+ and CO as the major product with 37% collisional efficiency. This reaction efficiency is in agreement with that reported elsewhere[10]. DFT calculations were performed for the ground quintet and first excited triplet Ta^+ reacting with CO. Those results are presented in Table 6 and Figure 3.

The adiabatic quintet PES is calculated to have a transition state 25.9 kcal/mol above the reactants and the products are 86.3 kcal/mol higher in energy than the quintet reactants, as shown in Table 6. In contrast the triplet adiabatic transition state is -8.1 kcal/mol lower than the quintet

reactants. This suggests that a spin crossing exists for the formation of TaO^+. This crossing likely occurs around the triplet transition state and fits well with the high efficiency reported for this reaction. However, closer examination of the computational data reveals a problem after this transition state.

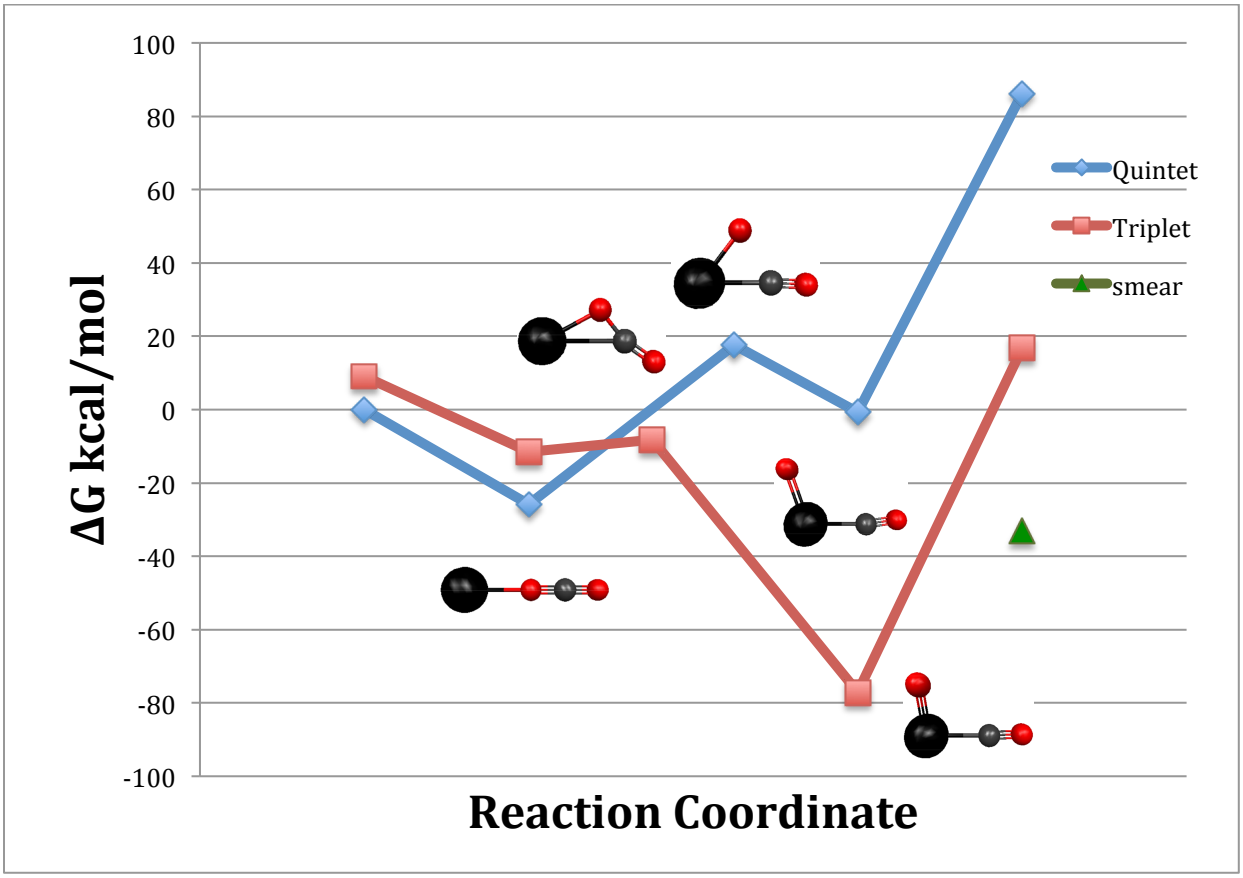

Figure 3: The DFT calculated stationary points on the PES for the reaction of Ta^+ and CO_2 The red line is the adiabatic surface of the triplet spin state and the blue line is the adiabatic surface of the quintet spin state. The triplet TaO^+ smear product appears as a green dot. The reaction side complex structure is nearly identical for both quintet and triplet spin states so only the lower energy quintet structure is shown. All other structures are inserted as closely as possible to their associated data point.

Table 6: DFT calculated free energies for the reaction of Ta^{x+} and CO_2 The energies are relative to the quintet (Ta^+) or quartet (Ta^{2+}) reactants. The charge transfer products are reported for the Ta^{2+} reactions and are taken to be quintet Ta^+ and CO^+ or triplet TaO^+ and CO_2^+.

ΔGrxn	Ta^+		Ta^{2+}	
Species	Quintet	Triplet	Quartet	Doublet
Reactants	0.0	9.1	0.0	21.0
Reaction Side Complex	-25.9	-11.5	-51.5	-42.9
Transition State	17.6	-8.1	-10.6	-25.4
Product Side Complex	-0.7	-77.1	-16.5	-88.6
Products	86.3	16.8	33.9	-41.3
Smear	***	-33.2	***	***

Charge Transfer	ΔG_{rxn}
Ta^+ and CO_2^+	-15.9
TaO^+ and CO^+	-7.9
smear TaO^+ and CO^+	-64.0

The adiabatic triplet product is calculated to be 16.8 kcal/mol higher in energy than the quintet reactants and is too high to explain the experimental results. Addition of the smear[45] technique, which allows partial occupation of orbitals in the DFT calculation, yielded a triplet TaO^+ product that is 33.2 kcal/mol lower in energy than the quintet reactants. Published DFT calculations on this reaction,[11] which differ from the methodology presented in this paper only in basis sets used, predicted a +52 kcal/mol barrier height. Those results would suggest that this reaction is impossible despite the overall calculated exothermic nature of the reaction.

MCSCF and MRPT2 calculations were undertaken for the reactions of Ta^+ monocations with CO_2 to explore the inconsistencies between the experiments and the calculations. For the reactants, bare Ta^+ was separated from CO_2 by a distance of 15 angstroms. A progressive energy scan of these complexes, taken by doing a single point energy calculation at various distances at the DFT level, deemed 15Å sufficient for eliminating interactions between the two species. Similarly the products TaO^+ were separated from CO by 15 Å. While the geometries were re-

optimized at the MCSCF level for each point on the PES using the DFT reference, very little deviation was found between the optimized DFT and optimized MCSCF geometries.

Modeling the reactants as 2 bodies in a single active space separated by 15 Å presented some obstacles unique to those points. Tantalum cations are unsaturated and there are multiple nearly degenerate orbitals. It was therefore difficult to maintain a consistent active space through the course of the MCSCF and MRPT2 calculations. It was necessary then to either reduce the active space, thereby reducing the number of determinants by eliminating some of the Ta d orbitals, or to run the reactants separately as two separate calculations (Ta and CO_2) and add the energies together after the fact. Because there was no systematic way of determining which Ta d orbital should be eliminated, creating two separate inputs gave more consistent results than reducing the active space. Doing the reactants in this fashion meant that no all-body Hessian could be performed for the reactant point on the PES. A similar issue was found for doing Hessians on the products point of the PES. The ZPE for those points where therefore taken to be the ZPE of CO_2 for the reactants, and for the products the sum of the zero point energies for TaO^+ and CO. These ZPEs were consistent with those found in the DFT calculations.

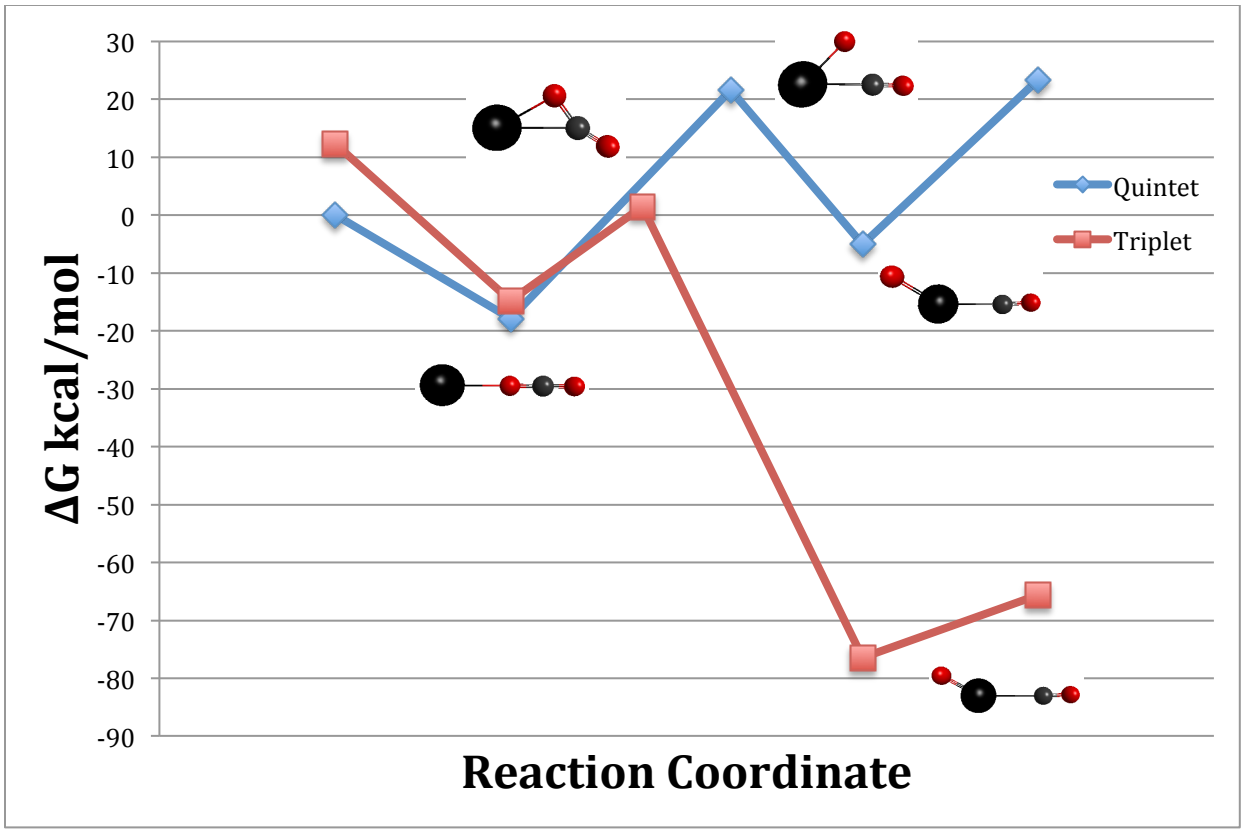

Figure 4: Calculated stationary points for the PES of the reaction of Ta^+ and CO_2 at the MRPT2 level. Energies are in kcal/mol relative to the quintet $Ta^+ + CO_2$ reactants. The reaction side complex structure is nearly identical for both quintet and triplet spin states so only the lower energy quintet structure is shown. All other structures are inserted as closely as possible to their associated data point.

Table 7: MRPT2 calculated free energy for the reaction of Ta^{2+} and CO_2 The charge transfer products are taken to be the triplet TaO^+ and CO^+ All energies are in kcal/mol

	ΔG_{rxn}	
Species	Quintet	Triplet
Reactants	0.0	12.3
Reactant Side Complex	-20.6	-16.7
Transition State	24.2	1.5
Product Side Complex	6.5	-76.0
Products	27.5	-63.5

For the $Ta^+ + CO_2$ reaction, the results shown in Figure 4 and Table 7 show that the use of multiconfigurational methods does seem to clarify the experimental data. The PES has the

same basic shape as the DFT calcualtions and shows the quintet reactants passing through a spin crossing around a possibly thermoneutral triplet transition state to form the triplet product. Even though geometries did not change significantly when reoptimized with MCSCF, the energetics are more favorable for the Ta^+ activating the C-O bond in CO_2 when explored with multiconfigurational methods compared to DFT. While the "smear" technique was employed with DFT to correct the product energies, MRPT2 calculations gives an energetically favorable product In fact, comparing the energies of the DFT and MRPT2 calculations, the MRPT2 relative energies are significantly lower even than that predicted using "smear". This, combined with the probable thermoneutral barrier, is sufficient to explain the relatively efficient activation of the CO bond in this reaction.

Dications

The experimental data for the reactions of Ta^{2+} and CO_2 reported in Table 5 show several interesting results. While Ta^{2+} activated the C-O bond with a collisional efficiency of 48%, charge transfer products were also observed. While the observation of Ta^+ is a primary charge transfer product, the observed TaO^+ could be either a primary or secondary reaction product as previously explained. DFT calculations were performed and reported in Table 6 and Figure 3.

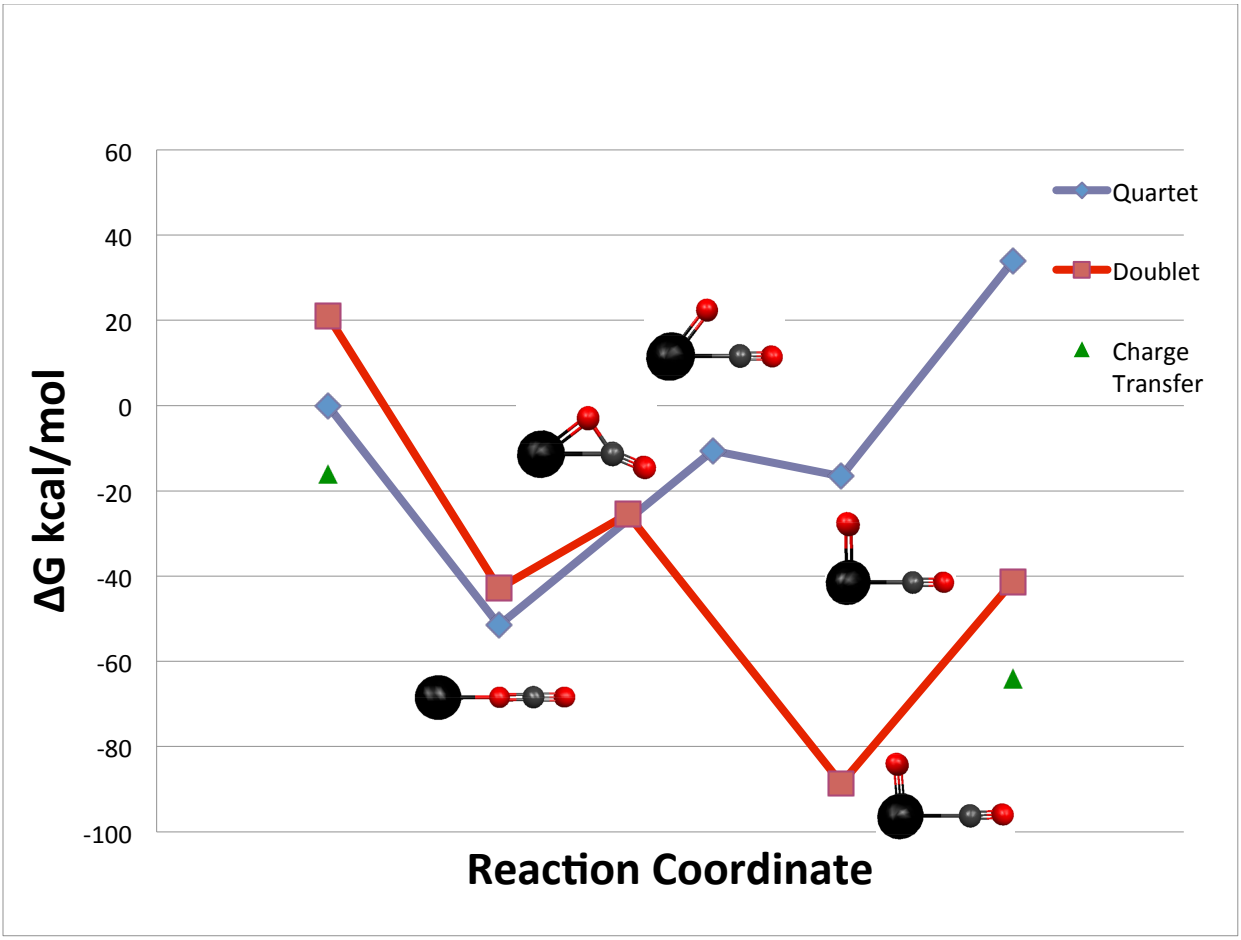

Figure 5: The DFT calculated stationary points on the PES for the reaction of Ta^{2+} and CO_2. The red line is the adiabatic surface of the triplet spin state and the blue line is the adiabatic surface of the quintet spin state. The green triangular points indicate the quintet Ta^{+} and triplet TaO^{+} charge transfer products. The reaction side complex structure is nearly identical for both quintet and triplet spin states so only the lower energy quintet structure is shown. All other structures are inserted as closely as possible to their associated data point.

As in the previous reactions, DFT calculations indicate a spin crossing between the ground quartet Ta^{2+} reactants and the doublet products. The crossing likely occurs around the doublet transition state, which is 20.3 kcal/mol lower in energy than the quartet ground state reactants. The doublet TaO^{2+} product is calculated to be 27.7 kcal/mol lower in energy than the quartet Ta^{2+} reactants. These results agree well with the experimentally observed 48% reaction efficiency. Charge transfer was also observed, in agreement with calculated data. Looking at the

charge transfer reactions, a simplistic thermodynamic examination of the charge transfer product side and reactant side energies, shown in Table 4, Table 6 and Figure 3, shows both charge transfer products to be favorable. Since reactions of Ta^+ with CO_2 are known to occur, as previously discussed, TaO^+ could form through either channel. Since both Ta^+ and TaO^+ were seen experimentally, the DFT calculations seem to adequately describe this reaction, though a more detailed examination of the charge transfer reactions is warranted. The MRPT2 results are very similar to those of the DFT calculations and so are not discussed in detail. Further information can be found in the supporting information.

Conclusions

A flowing afterglow instrument was used to react Ta^{x+} with CO and CO_2. Kinetic data was calculated for the experimental information and DFT, MCSCF and MRPT2 calculations were performed to gain insight into the reaction processes. While DFT calculations predicted a complexation limit of $Ta(CO)_6^{x+}$, experimentally only Ta^{2+} reached that limit, and the mono complex was the only observed complexation product for Ta^+. The experimental absence of these higher order complex may be due, in part, to the relative collisional inefficiency of the monocation compared to the dication. It would be interesting to see if higher order $Ta(CO)_n^+$ where n>1 complexes exist in a cosmic experiment of more infinite timescale such as those that exist in interstellar clouds.

Both Ta^+ and Ta^{2+} showed a relatively efficient ability for activating the C-O bond in CO_2, and metal oxide products were observed in both cases. Charge transfer products were also observed for the dication reactions. DFT calculations on the monocation were confusing but

MRPT2 calculations suggested a thermoneutral transition state and exothermic products which are in agreement with experimental results. DFT calculations on the dication similarly agree with the experiment, suggesting a very low barrier for reaction and exothermic products. Both DFT and MRPT2 calculations predict a spin crossing exists in the PES leading from the reactants to the products. Charge transfer was explored with DFT in a very rudimentary way and no barrier for the formation of charge transfer products was suggested. More studies are needed to better understand the mechanism of the charge transfer reactions.

Acknowledgements

This material is based upon work supported by the National Science Foundation under Grant No. OISE-0730114 for the Partnerships in International Research and Education (PIRE) and also by support to TLW by the U.S. Department of Energy, Office of Basic Energy Sciences, Division of Chemical Sciences, Geosciences, and Biosciences through the Ames Laboratory Chemical Physics project. The Ames Laboratory is operated for the U.S. Department of Energy by Iowa State University under Contract No. DE-AC02-07CH11358. This research was also supported by an allocation of advance computing resources provided by the National Science Foundation. The computations were performed on Kraken at the National Institute for Computational Sciences.

References

(1) D. Golomb , S. P., D . Ryan, E. Barry, P. Swett *Environ. Sci. Technol.* **2007**, *41*, 4698.

(2) Khoo, H. H. T., Reginald B. H *Energy Fuels* **2006**, *20*, 1914.

(3) Yu, H. Z., Guangzhu; Fan, Weitang; Ye, Jianping. *Int. J. Coal Geol.* **2007**, *71*, 345.

(4) Behr, A. *Carbon Dioxide Activation by Metal Complexes*; VCH: New York, 1998.

(5) Pickett, C. J.; Vincent, K. A.; Ibrahim, S. K.; Gormal, C. A.; Smith, B. E.; Fairhurst, S. A.; Best, S. P. *Chem. Eur. J.* **2004**, *10*, 4770.

(6) Heo, J. S., C. R.; Ludden, P. W. *Biochemistry* **2001**, *40*, 7604.

(7) Tielens, A. G. G. M.; Wooden, D. H.; Allamandola, L. J.; Bregman, J.; Witteborn, F. C. *ApJ* **1996**, *461*, 210.

(8) Winnewisser, G.; Herbst, E. *Top. Curr. Chem.* **1987**, *139*, 119.

(9) Herbst, E. *Advances in Gas Phase Ion Chemistry* **1998**, *3*, 1.

(10) Koyanagi, G. K.; Bohme, D. K. *J. Phys. Chem. A* **2005**, *110*, 1232.

(11) Wang, Y.-C.; Yang, X.-y.; Geng, Z.-Y.; Lui, Z.-Y. *Chem. Phys. Lett.* **2006**, *431*, 39.

(12) Herman, J.; Foutch, J. D.; Davico, G. E. *J. Phys. Chem. A* **2007**, *111*, 2461.

(13) Bierbaum, V. M.; DePuy, C. H.; Shapiro, R. H.; Stewart, J. H. *J. Am. Chem. Soc.* **1976**, *98*, 4229.

(14) Ferguson, E. E.; Fehsenfeld, F. C.; Schmeltekopf, A. L. *Advances in Atomic and Molecular Physics* **1969**, *5*, 1.

(15) Valiev, M.; Bylaska, E. J.; Govind, N.; Kowalski, K.; Straatsma, T. P.; Van Dam, H. J. J.; Wang, D.; Nieplocha, J.; Apra, E.; Windus, T. L.; de Jong, W. A. *Comput. Phys. Commun.* **2010**, *181*, 1477.

(16) Becke, A. D. *J. Chem. Phys.* **1992**, *96*, 2155.

(17) Becke, A. D. *J. Chem. Phys.* **1993**, *98*, 5648.

(18) Hay, P. J.; Wadt, W. R. *J. Chem. Phys.* **1985**, *82*, 270.

(19) Krishnan, R.; Binkley, J. S.; Seeger, R.; Pople, J. A. *J. Chem. Phys.* **1980**, *72*, 650.

(20) Cheung LM, S. K., Ruedenberg K *J. Am. Chem. Soc.* **1978**, *100*, 8024.

(21) Cheung LM; Sundberg KR; K, R. *Int. J. Quantum Chem* **1979**, *16*, 1103.

(22) Roos BO, T. P., Siegbahn PEM. *Chem. Phys.* **1980**, *48*, 157.

(23) Siegbahn PEM, A. f. J., Heiberg A, Roos, B.O. *J. Chem. Phys.* **1981**, *74*, 2384.

(24) Feller DF, S. M., Ruedenberg K. *J. Am. Chem. Soc.* **1982**, *104*, 960.

(25) K, R.; MW, S.; Gilbert MM, E. S. *Chem. Phys.* **1982**, *71*, 65.

(26) Ruedenberg K, S. M., Gilbert MM, Elbert ST *Chem. Phys.* **1982**, *71*, 41.

(27) Ruedenberg K, S. M., Gilbert MM *Chem. Phys.* **1982**, *71*, 51.

(28) Roos, B.O. *Adv. Chem. Phys.* **1987**, *69*, 399.

(29) Schmidt, M. W.; Gordon, M. S. *Annual Review of Physical Chemistry* **1998**, *49*, 233.

(30) Andersson K, M. P.-A., Roos BO, Sadlej AJ, Wolinksi K. *J. Phys. Chem. A* **1990**, *94*, 5482.

(31) Andersson K, M. P.-A., Roos BO. *J. Chem. Phys.* **1992**, *96*, 1218.

(32) K., A. *Theor. Chim. Acta* **1995**, *91*, 31.

(33) H-J., W. *Mol. Phys.* **1996**, *89*, 645.

(34) Schmidt, M. W.; Baldridge, K. K.; Boatz, J. A.; Elbert, S. T.; Gordon, M. S.; Jensen, J. H.; Koseki, S.; Matsunaga, N.; Nguyen, K. A.; Su, S. J.; Windus, T. L.; Dupuis, M. M., J. A. *J. Comput. Chem.* **1993**, *14*, 1347−1363.

(35) Gordon, M. S.; Schmidt, M. W. *Theory and Applications of Computational Chemistry: The First Forty Years*; Elsevier: The Netherlands, 2005.

(36) Kendall, R. A.; Dunning, T. H.; Harrison, R. J. *J. Chem. Phys.* **1992**, *96*, 6796.

(37) Su, T.; Chesnavich, W. J. *J. Chem. Phys.* **1982**, *76*, 5183.

(38) Koopmans, T. *Physica* **1934**, *1*, 104.

(39) Stein, T.; Eisenberg, H.; Kronik, L.; Baer, R. *Physical Review Letters* **2010**, *105*, 266802.

(40) Bartlett, R. J.; Schweigert, I. V.; Lotrich, V. F. *Journal of Molecular Structure: THEOCHEM* **2006**, *771*, 1.

(41) Tsuneda, T.; Song, J.-W.; Suzuki, S.; Hirao, K. *The Journal of Chemical Physics* **2010**, *133*.

(42) Zhang, G.; Musgrave, C. B. *The Journal of Physical Chemistry A* **2007**, *111*, 1554.

(43) Luo, J.; Xue, Z. Q.; Liu, W. M.; Wu, J. L.; Yang, Z. Q. *The Journal of Physical Chemistry A* **2006**, *110*, 12005.

(44) Salzner, U.; Baer, R. *J. Chem. Phys.* **2009**, *131*, 231101.

(45) Warren, R. W.; Dunlap, B. I. *Chem. Phys. Lett.* **1996**, *262*, 384.

CHAPTER 5: MAKING VIRTUAL ORBITALS WORK FOR YOU

Emily Hull, Theresa L. Windus, Mike Schmidt

Department of Chemistry, Iowa State University, Ames, Iowa 50011, USA

Abstract

The method, previously published[1-5], for recasting molecular orbitals in terms of intrinsic minimal bases of quasiatomic orbitals, is expanded to include first and second row transition metals. Calculations were performed on several organic compounds and compared with analogous transition metal species to show the validity of the extension. New applications for this method include MCSCF approximation by doing CI excitations in the virtual valence space, qualitative assessment of CIS/TDDFT interactions without the computational cost of doing CIS/TDDFT and analysis of basis set effects. This paper focuses on the extension of the QUAMBO method to molecules containing any atoms from H-Xe, especially first and second row transition metals.

Introduction

The QUasi Atomic Minimal Basis Orbital (QUAMBO) method was recently introduced[1-5], and its methodology has several underlying principles which are universal to quantum chemistry. These principles are: that molecules are composed of atoms; atomic orbitals deform to combine into molecular orbitals; and extended basis set solutions contain minimal basis set

(MBS) information which is molecule-intrinsic and independent of the actual basis set used for the molecular calculation.

In order to extract the minimal basis set of information, a simple algorithm was devised. In simple terms, the QUAMBO method takes the best possible minimal-basis set solution for the atoms, and projects it onto the full basis set space. The free-atom minimal basis space A_j^* is defined as

$$A_j^* = \sum_n \emptyset_n \, a_{nj}^* + \sum_v \emptyset_v \, a_{vj}^*$$

Using the projections:

$$a_{nj}^* = \langle \emptyset_n | A_j^* \rangle$$

and

$$a_{vj}^* = \langle \emptyset_v | A_j^* \rangle$$

where A_j^* = Valence orbitals of the free atomΨ_ps, $j = 1,2,....M$ where M is the total number of minimal-basis-set valence atomic orbitals, and $\emptyset_n$ and $\emptyset_v$ are the occupied and valence molecular orbitals.

The quasiatomic molecular orbitals, i.e. QUAMBOS, A_j are defined as

$$A_j = \sum_n \emptyset_n a_{nj} + \sum_v \emptyset_v a_{vj}$$

where j= 1,2,…., $M = N + P$, $n = 1,2,.....N$ and v= N+1, N+2, ... N+V . These limits are due to the fact that there are fewer minimal basis orbitals (M) than the number of extended basis molecular orbitals. N+P, then is the number of N occupied minimal basis orbitals (the number of occupied orbitals N is the same for the minimal and extended basis spaces) plus P minimal basis valence orbitals. Similarly, N+V is the total number of extended basis molecular orbitals (N

occupied plus V valence). The goal is then to create an algorithm to deduce a_{nj} from $a^*_{nj}$and and a_{vj} from a^*_{vj}. Details of this algorithm can be read in previously published work.[1-5]

The end result of the QUAMBO calculation is a set of orbitals that are intrinsically localized and basis set independent. Canonicalization of the QUAMBOS recovers the occupied molecular orbitals,. Applying the QUAMBO algorithm to doesn't change the orbital energies, basic shape, or ordering of the occupied orbitals relative to the base RHF molecular orbitals. QUAMBO occupied orbitals are, therefore, easy to compare with occupied orbitals of any other method. Analyzing the difference between the QUAMBO and the canonical molecular orbital (MO) solution gives interesting information on the nature of chemical bonds and such phenomenon as ring strain.[1,2] Since the MBS valence orbitals are projected onto the full MO valence space, virtual-valence orbitals (VVOs) are found which closely resemble the orbitals of simple MO theory. Together these QUAMBO and VVOS can give qualitative information about molecular bonding, interactions between the occupied and virtual spaces, and the algorithm itself generates the best set of starting orbitals for a Complete Active Space-Self Consistent Field[6-8] (CAS-SCF) calculation.[1-5]

The application of atomic minimal basis orbitals to deduce qualitative information from molecular orbitals has been proposed before and the QUAMBO method has many similarities with previously published methods.[9-11] Atomic minimal basis orbital projections into molecular orbital spaces have previous been used to partition and localize the valence space. The extended virtual orbitals of the QUAMBO method, obtained through the application of singular value decomposition, are analogous to the hard virtual orbitals of Subotnik et.al.[12] Another method combined minimal basis projections with Cholesky decomposition for local multi-reference configuration-interaction.[13,14] Differences between the QUAMBO method and those previously

proposed include the treatment of the extended virtual orbitals and the minimal basis set used. This work focuses on the minimal basis. Details of the treatment of the extended virtual orbitals can be found in the preceding paper.[5]

The QUAMBO algorithm requires the minimal basis set that represents the best possible self-consistent field (SCF) solution for the individual atoms in the molecule. This can be accomplished by taking the best SCF solution for the atoms and performing a minimal basis contraction. In the original QUAMBO formulation, the best SCF solution is that obtained using an SCF basis set which itself converges to the SCF limit for any given atom. In the case of H-Ar, the Even-Tempered basis sets of Ruedenberg and Schmidt[15] were employed for this purpose. This paper expands the applications of the QUAMBO method and explores the use of the QUAMBO method for those molecules containing atoms K-Xe, including transition metals. For main group elements it was deemed that an unmodified Well-Tempered Basis Set[16] (WTBS) of was sufficient for this purpose. The WTBS used in this current work to create the free-atom SCF solutions in the projections were optimized for the ground electronic state configurations

Transition metals contain an electronic configuration conundrum. An analysis of experimental data[17] shows that in unsaturated transition metals, the ground and first excited state configurations are energetically close at room temperature. Considering the reaction conditions of many inorganic and organometallic synthesis, this small separation may mean that excited states could be involved in the course of a given chemical reaction. For example, the ground state s^1d^4 ^6D configuration of neutral niobium is only 6 kcal/mol below the excited state s^2d^3 ^4F configuration.[18] The ground state ^4F configuration for cobalt is s^2d^7. The first excited configuration is s^1d^8 and also has a ^4F term symbol. The two configurations are only separated by about 10 kcal/mol[18]. The SCF solution for cobalt is intrinsically multi-configurational. As

another example, platinum has a ground state ^{1}S electronic configuration of s^0d^{10}, and basis sets optimized to that configuration could be inaccurate in modeling s^1d^9 first excited configuration which lies 18kcal/mol above the ground configuration[18]. Therefore, the form of the minimal basis solution for transition metals requires a more nuanced approach than that of non-metal species.

Computational Methodology

Calculations were performed using the GAMESS[19,20] computational chemistry package. The atomic transition-metal orbitals were generated from a weighted-state averaged MCSCF atomic calculation using the WTBS[16] in order to account for the ground and first excited configurations, which were deemed chemically accessible for unsaturated transition metals when the states were separated by 20 kcal/mol or less. Nickel, for example, has a ground ^{3}F configuration of $4s^23d^8$ and an excited ^{3}D configuration of $4s^13d^9$. The terms are given a 50/50 weighting, and for nickel this means 7(5/70) for the ground and 5(7/70) for the first excited configuration. This has the effect of slightly raising the energy of the ground state and slightly reducing the energy of the first excited configuration relative to reference values when the new basis is used to explicitly solve for those atomic configurations. The weighted state-averaging was restricted to the ground and first excited configuration and only for those atoms where those configurations were separated by 20 kcal/mol or less.

For palladium, which lies between rhodium and silver, the WTBS is optimized only to the ground s0d9 configuration and modifications were necessary to the basis set itself. Rather than re-optimize the basis set for paladium, the N, Ns, Np, Nd (number of primitive Gaussian basis functions) basis set configuration for silver was combined with WTBS α β γ δ formula

values that were derived by averaging the values of rhodium and silver. The change in the basis set for platinum resulted in an increase of the ground state energy from the reference WTBS ground state optimized value by just $7x10^{-5}$ kcal/mol. This very small difference indicated that the approximation was reasonable and a re-optimization of the basis set was not necessary for the purposes of this method. The atomic orbitals were then stored in GAMESS so that they would not have to be regenerated for each new molecular computation.

Orbitals were visualized using the MacMolPlot[21] visualization program. For diborane and indigo, structures were based on previously published structures[22] that were re-optimized at the RHF/aug-cc-pVTZ[23] level for this study. The structure of ferrocene was taken from crystal structure data[24-26] and re-optimized at the B3LYP[27,28]/6-31G*[29,30] level and the rhodium complex was optimized at the B3LYP[27,28] level using the Stuttgart small core ECP[31,32] for the rhodium and cc-pVDZ[23] for all other atoms with the length of the Rh-water bond shortened to match the experimental crystal structure. Since the purpose of this work is to look at the orbitals, the exact structures are not of specific interest in this study. However, they are available in the supporting information.

While the main purpose of this paper is the introduction of transition metals to the QUAMBO algorithm, it is important to include main group compounds to ensure the same types of interactions that QUAMBO explores in min group compounds can also apply to inorganic or organometallic systems. To that end diborane was chosen as the main group molecule to model electron deficient bonding, reproducibility of well known molecular orbital interactions, and basis set independence. Ferrocene, with its well studied bonding interactions, is an inorganic analog of diborane. Indigo was chosen because it is relatively small and the interactions between

the occupied and virtual orbitals give rise to its characteristic color. An experimental rhodium complex is an inorganic analog of indigo.

Results and Discussion

Indigo

Indigo, 2,2'-Bis(2,3-dihydro-3- oxoindolyliden), is a commonly used dye that has been derived from plant sources such as *indigofera tinctoria* and *isatis tinctoria*[33] or more commonly chemically synthesized. Garments dyed with indigo have a characteristic deep blue color depending on the quantity of dye used in the vat. A previously published paper examined indigo and similar molecules in detail[22]. This study looks at how the virtual valence orbitals of the QUAMBO/VVO method compared with Hartree-Fock, and TD-HF (CIS).

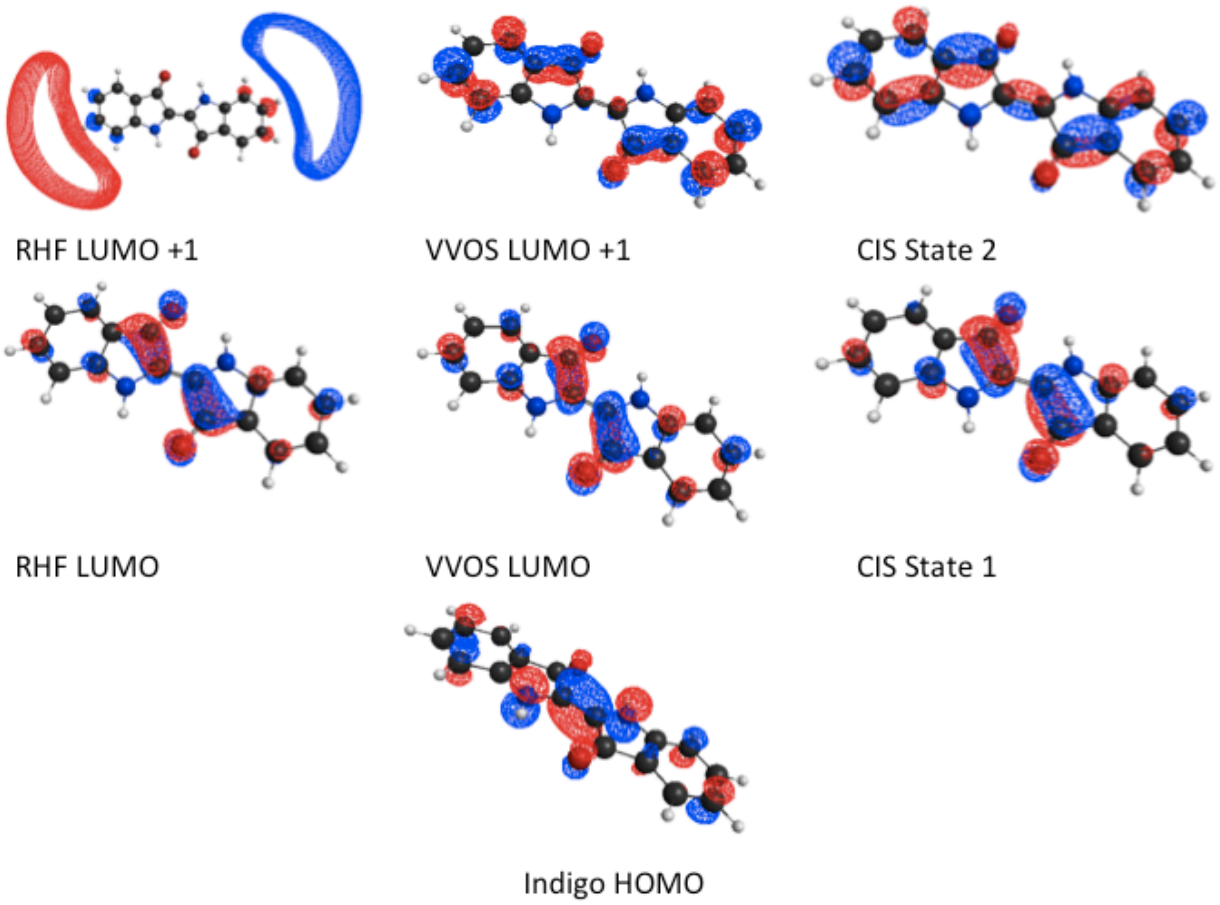

Figure 1: Comparison of RHF, VVOS and CIS calculated orbitals using CIS/TD-HF, VVOs, and RHF with an aug-cc-pvTZ basis sets

Chemists like to visualize and justify observable characteristics with orbital explanations. Most often these are explanations involving the Highest Occupied Molecular Orbital (HOMO) and the Lowest Unoccupied Molecular Orbital (LUMO) interactions, but sometimes other orbitals are considered as well. Figure 1 shows the difficulty in using orbitals generated from a typical computational chemistry calculation for these purposes. Figure 1 shows the HOMO and first two unoccupied orbitals (or CIS state 1 and 2) from RHF, CIS/TDHF and VVOs methods. The HF LUMO +1 is very strange looking from a simple molecular orbital standpoint and reflects the use of the large basis set with many diffuse functions, although it can be common for

the HF LUMO or LUMO+1 to not have valence character. On the other hand, the VVOs and CIS calculations are in very good agreement. This gives the potential for VVOs as a screening technique to check which orbitals are interacting before going to a more expensive excited state technique.

Diborane

Interest in the electronic and geometric configuration of diborane (B_2H_6) goes far back in the history of chemistry. As a 12 electron system it is clearly electron poor, but somehow is stabilized by an usual pair of 2 electron, 3 center bonds. Due to its similarities with ethane (C_2H_6), the two have long been compared. Before 1920, the two molecules were considered to have identical geometry and bonding, and it wasn't until 1921 that a bridging structure was proposed, and not until the 1940's that a bridging structure for diborane was taken seriously[34]. The first spectroscopic evidence for a bridging structure also appeared in the 1940's[35-37] and a single crystal structure firmly establishing the bridging geometry was published and defended in the 1960's[38,39] though discussion about the electronic structure has continued all through this period and beyond[34,40-46]

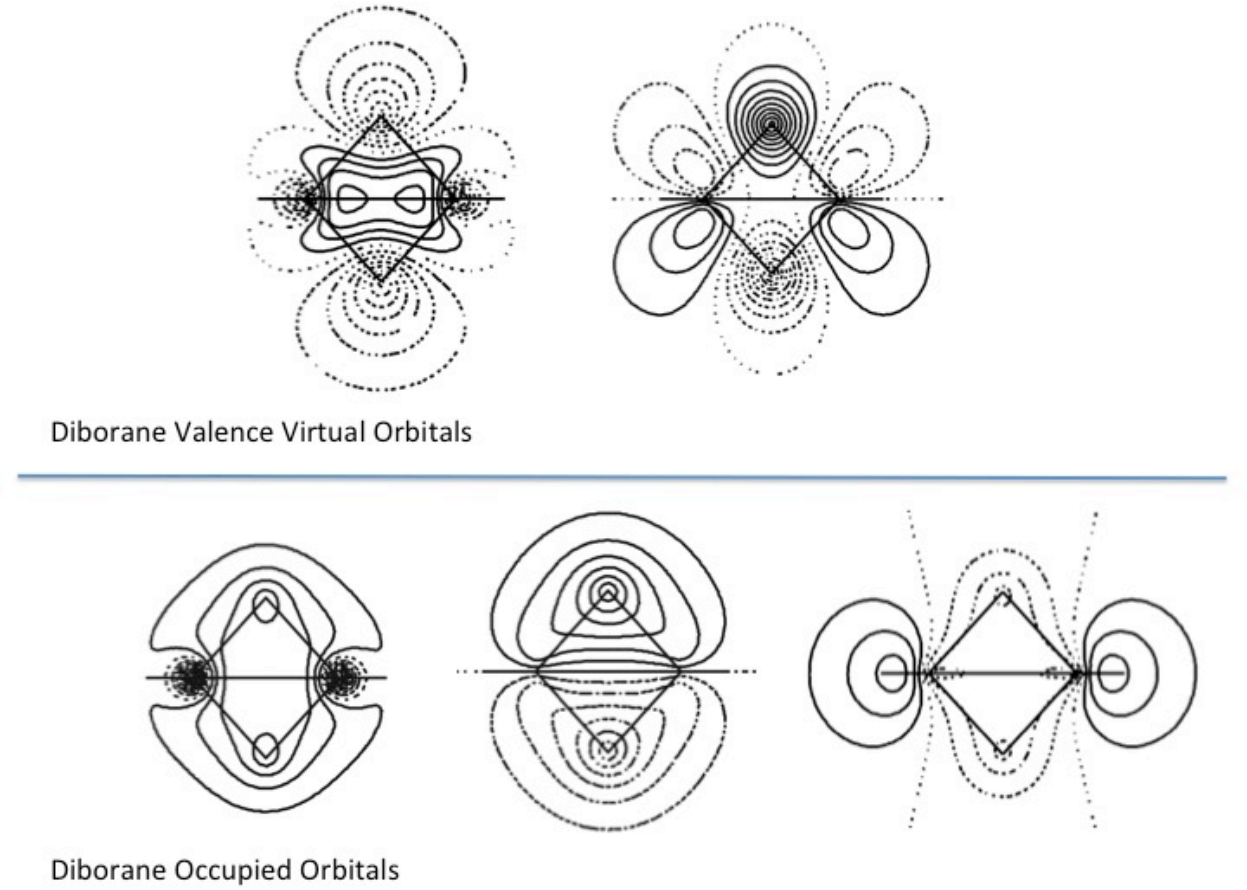

Figure 2: Diborane B-H-B bonding and anti-bonding orbitals represented by 2-D molecular contour diagrams.

It is clear from Figure 2 that the expected molecular orbital theory orbitals for B-H-B bonding in diborane are well represented by the VVO model. This is interesting because it also shows that the 2-electron, 3-center bond can be represented by the simple QUAMBO model. This shows promise for modeling other electron poor bonds, such as agostic interactions in inorganic chemistry.

Since the QUAMBO/VVOs model generates those orbitals in the virtual space directly related to the valence atomic orbitals, this makes it an excellent tool for selecting orbitals for

CAS-SCF. Diborane was chosen to test this due to its small molecular structure and complete active space size.

Table 1: Comparisons of energy calculations done with VVOS orbitals. [a]Difference is the incremental energy gained by doing the higher order calculation, for example E(CISDT)-E(CISD). The CI(1-12) and CAS-SCF energies are compared to the CIS energy. [b]Difference is the difference between the level of excitation and the CI(1-12), for example E[CI(1-12)]-E(CISD) All energies are reported in Hartree, A.U.

Excitations	Total Energy	Difference[a]	Difference[b]
CIS	-52.835438	0.000000	0.103652
CISD	-52.932970	-0.097532	0.006119
CISDT	-52.934229	-0.001259	0.004860
CISDTQ	-52.938910	-0.004681	0.000179
CI(1-5)	-52.938994	-0.000084	0.000096
CI(1-6)	-52.939087	-0.000093	0.000002
CI(1-7)	-52.939089	-0.000002	0.000001
CI(1-8)	-52.939090	-0.000001	0.000000
~	~	~	~
CI(1-12)	-52.939090	0.000000	0.000000
CAS-SCF	-52.955492	-0.120621	0.016403

A series of sequentially higher-order CI calculations were performed from the occupied valence orbitals into the VVO space. These calculations were then compared to a CAS-SCF calculation in the same space. Diborane has 6 occupied valence and 8 virtual valence orbitals for a CAS-SCF size of 12 electrons in 14 orbitals. A sequential calculation is then a CIS, CISD, CISDT, CISDTQ, then a CI(1-5) which adds the five fold excitation and on to CI(1-12) which represents the full twelve-fold excitation of the occupied electrons into the entire VVO space. The results of this test are seen in Table 1. There are several interesting features of Table 1. Looking at the 1st and 3rd columns in table 1 it can be seen that by the eightfold excitation the calculation has essentially converted (to six decimal places) to the full twelve fold CI(1-12) value. It can be also seen, by comparing the incremental energy correction due to higher order

excitations in column 2, that the largest corrections to the CIS are achieved by adding second order or fourth order excitations with very little energy correction to be gained by anything higher than fourth order. It is further found that a CISD or better still a CISDTQ excitation from the occupied into the VVOS space is a very good approximation of the MCSCF energy at a fraction of the computational cost.

To show the basis set independence and better visualize the effect of basis set choice on a calculation, RHF and QUAMBO/VVOS calculations were done with diborane using a small set of sequentially larger and more complicated basis sets, and the results compared. The first basis set is Huzinaga's MINI[47] basis set. Since the QUAMBO method is already a minimal basis set method, the number of orbitals generated by QUAMBO/VVOS is the same as an RHF/MINI calculation. Calculations were then done using 6-31G[29], a larger basis set than the MINI basis set, but one without polarization or diffuse function, cc-pVTZ[23] which is larger than 6-31G and has polarization functions, and finally aug-cc-pVTZ[23] which adds diffuse functions. Generally speaking, for a given method (HF or DFT for example) the occupied orbitals change very little with different basis sets. The major difference in basis sets is the way they act in the virtual space. The results are shown in Figures 4 and 5.

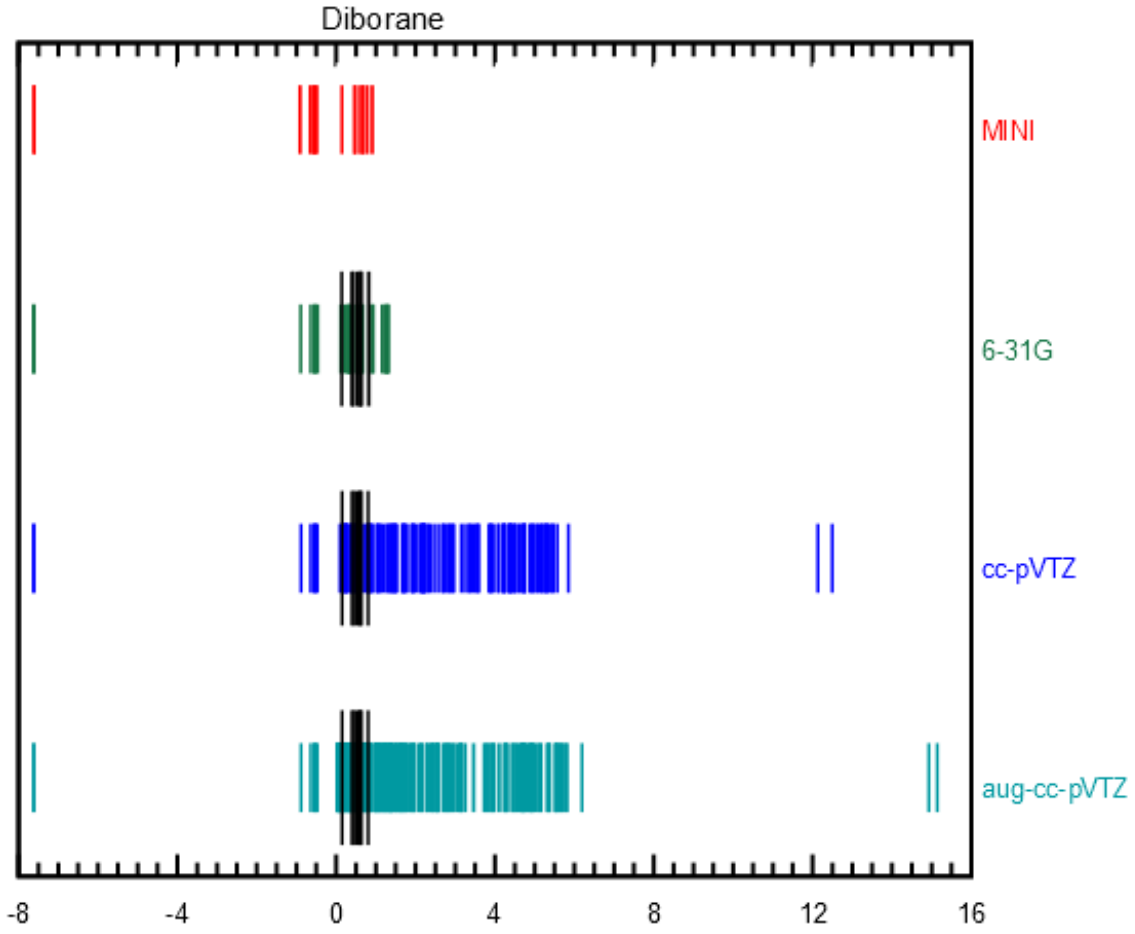

Figure 4: A plot of the orbital energies for multiple basis sets starting with smaller basis sets on the top and more extensive basis sets on the bottom. The thicker overlays are the virtual valence orbitals generated by the QUAMBO algorithm. The bottom axis is energy in hartrees.

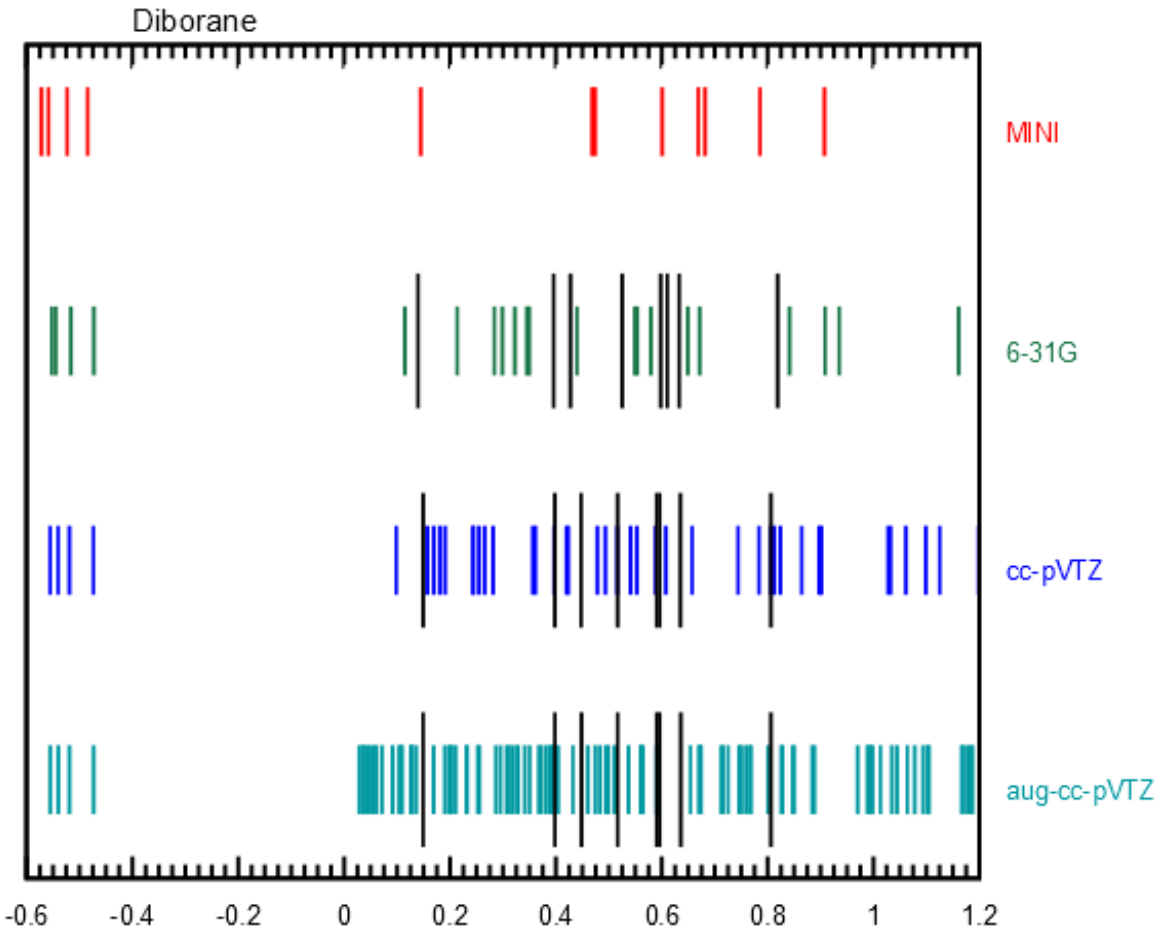

Figure 5: Detailed basis set plot of each orbital energy within the range of only a few of the highest occupied orbitals and the highest energy VVO for a given basis set. The comparison of the VVOs to the canonical Hartree Fock virtual orbitals to show the basis set independence of the method. The bottom axis is energy in hartrees.

Figure 4 shows the entire energy range of every generated orbital, from orbital 1 all the way to the end of the virtual space. Figure 5 is truncated and shows only the highest occupied levels and the virtual levels covered by the QUAMBO/VVO orbitals. An interesting characteristic from these plots is that it clearly visualizes how different basis sets behave. Due to the fact that there are a finite number of occupied orbitals, basis sets with more functions will necessarily generate more orbitals in the virtual space than the occupied space. This is clearly shown in Figure 4: the number of orbitals generated by 6-31G is greater than that for the MINI

basis set which only covers the virtual valence space, but are still less than the cc-pVTZ set. Another interesting observation, as seen in Figure 4 but even more clearly in Figure 5, is that the addition of diffuse functions in the aug-cc-pVTZ set shifts the virtual orbital energies towards the occupied space, reducing the size of the HOMO-LUMP gap, compared to the cc-pVTZ. These are qualitative observations; the quantitative nature of the band gap itself isn't of interest to this study. It is also clear that while the RHF orbitals belonging to each basis set spans a different set of states, especially obvious when comparing 6-31G to aug-cc-pVTZ in Figure 4, the orbitals generated by the VVOS in the virtual space are strikingly similar, as seen in Figure 5. This shows that the VVOs are virtually independent of the basis set.

Transition Metals

Ferrocene is a model inorganic molecule for many chemists. Once its synthesis was reported[48], debate began on the nature of the structure[49], and later on the nature of the bonding[50]. Crystal structure analysis[25], while confirming the sandwich shape, did not lessen the enthusiasm for chemists excited about whether it was eclipsed or staggered, and what was the barrier to internal rotation between the two configurations. The well studied crystal structure of the molecule makes it a good benchmark for computational chemists, and its complex chemistry makes it a wonderful base for many inorganic compounds. Interest in this molecule continues to the present time.

An excellent review of ferrocene chemistry explains the bonding of ferrocene and gives an MO diagram in terms of the staggered D_{5d} conformation[26], but the interactions and bonding is essentially the same for both D_{5d} and D_{5h} structures. Explanations of the iron-cyclopentadiene (Cp) bonding in ferrocene lead to the expectation of two bonding Fe-Cp orbitals, two non-bonding Fe orbitals, and two orbitals where the d_{z2} has a very small interaction with the Cp to

form a weakly interacting Fe-Cp a_{1g} orbital and a mostly metal a_{2g} orbital.[26] The virtual orbital counterparts of the bonding orbitals would have the anti-bonding orbitals be mostly metal in character instead of mixed. Non-bonding orbitals won't show up in the virtual space represented by a traditional MO diagram.

A VVOs calculation was done on ferrocene and the bonding and anti-bonding orbitals examined. The D_{5h} form was used for computational simplicity.

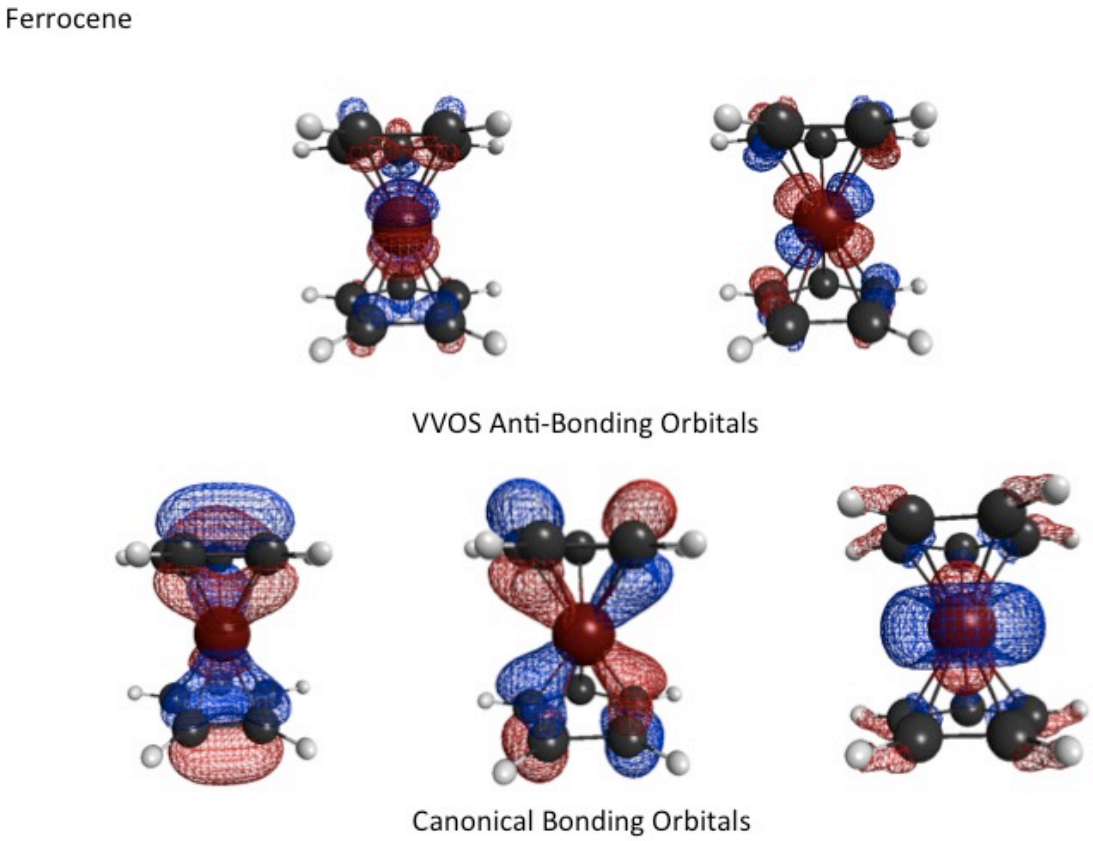

Figure 6: Occupied and virtual orbitals from a QUAMBO calculation of ferrocene in the D_{5h} point group using the cc-pVTZ basis set.

As discussed in the previous paragraph, a calculation should generate 2 strongly bonding orbitals and a weakly interacting, though not necessarily bonding d_{z2} orbital, and 2 associated anti-

bonding orbitals. These are clearly seen in Figure 6 and correspond well to the inorganic chemistry bonding arguments for ferrocene.

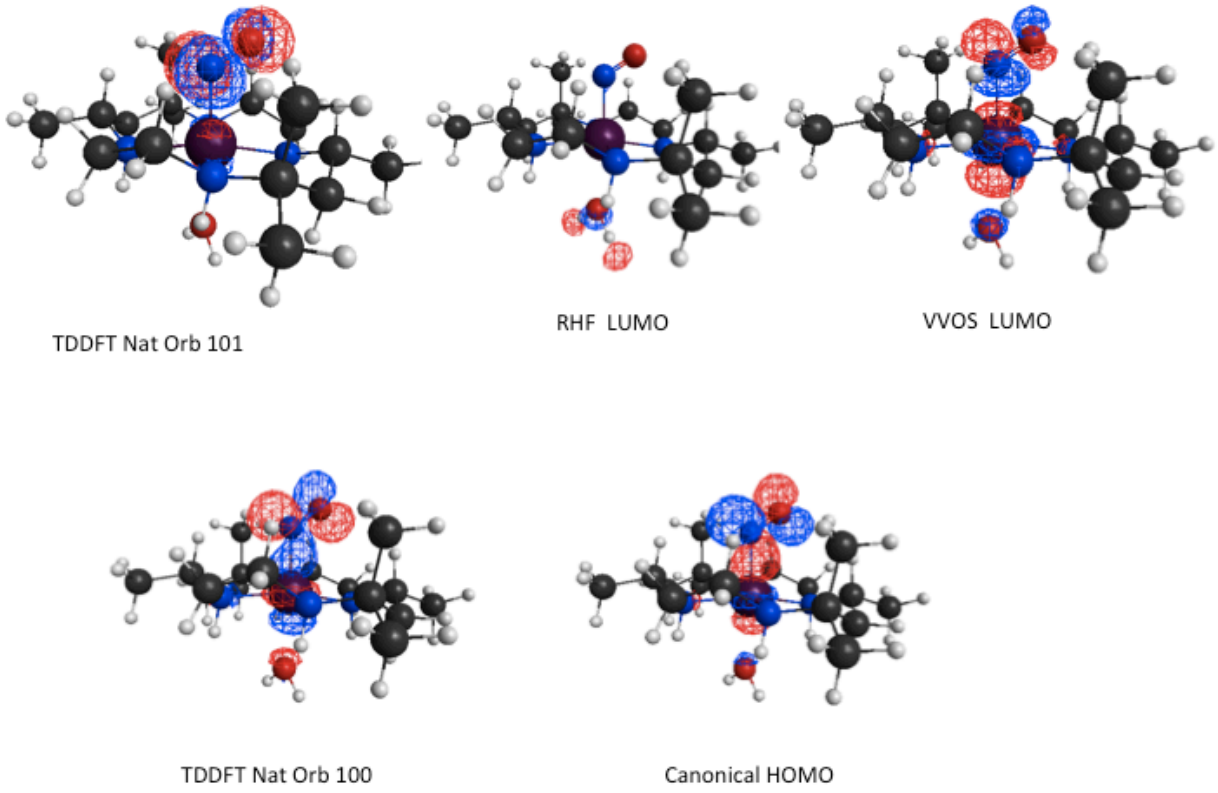

Figure 7: Comparison of TDDFT, RFH and VVO molecular orbital calculations on $L^2RhNO(H_2O)^{2+}$.

Calculations were performed on another molecule, $L^2RhNO(H_2O)^{2+}$, which experimentally interesting due to its photochemistry where NO is released upon UV irradiation. TDDFT calculations[51] on this system indicated that this photochemistry is mostly due to interactions between TDDFT natural orbitals 100 and 101. Those TDDFT calculations were previously performed[51] with GAMESS[19,20] and NWCHEM[52] using the Stuttgart small core ECP[31,32,53] for the rhodium, and the cc-pVDZ[23] basis set for the remaining atoms. Currently

VVO calculations require all-electron basis sets, so for the VVO calculation, the all electron Sapporo[54-56] augmented double zeta basis sets were chosen for computational efficiency.

The results in Figure 7 show that for this molecule, like indigo, the LUMO VVO is more similar to the TDDFT natural orbital than it is to the RHF virtual orbital. This result is despite the fact that two different basis sets were used, further showing the basis set independence of the method. This also shows that VVOS, unlike canonical RHF orbitals, are predictive of valence excited states.

Conclusions

The QUAMBO algorithm previously devised and published[1-5] was tested on several different molecules and the model was extended to transition metals. The algorithm is now available in GAMESS[19,20] for molecules containing any atom up to xenon. The model provides insight into fundamental bonding interactions, including electron poor multi-centered bonding interactions including agostic interactions. In addition VVOS orbitals, by nature of generating the simple molecular orbital theory virtual orbital counterparts of the occupied space, are naturally suited for use in further calculations like MCSCF or CI. Higher order CI excitation calculation within the VVOS space (CISD or higher) can give a good estimate of the MCSCF energy at a fraction of the computational cost. The valence virtual orbitals are closer in character to the virtual orbitals of excited state method orbitals, like TD-HF, than canonical RHF virtual orbitals, giving qualitatively useful information on interactions without the expense of an excited state method. Further expansions of the QUAMBO method would involve making it compatible with ECP/MCP basis sets and relativistic basis sets.

Acknowledgments

This material is based upon work supported by the National Science Foundation under Grant No. OISE-0730114 for the Partnerships in International Research and Education (PIRE). A portion of the computations were performed on Kraken at the National Institute for Computational Sciences.

References

(1) Lu, W. C.; Wang, C. Z.; Schmidt, M. W.; Bytautas, L.; Ho, K. M.; Ruedenberg, K. *The Journal of Chemical Physics* **2004**, *120*, 2638.

(2) Lu, W. C.; Wang, C. Z.; Schmidt, M. W.; Bytautas, L.; Ho, K. M.; Ruedenberg, K. *The Journal of Chemical Physics* **2004**, *120*, 2629.

(3) Ivanic, J.; Atchity, G.; Ruedenberg, K. *Theor Chem Acc* **2008**, *120*, 281.

(4) Ivanic, J.; Ruedenberg, K. *Theor Chem Acc* **2008**, *120*, 295.

(5) West, A. C.; Schmidt, M. W.; Gordon, M. S.; Ruedenberg, K. *The Journal of Chemical Physics* **2013**, *139*, 234107.

(6) Roos BO, T. P., Siegbahn PEM. *Chem. Phys.* **1980**, *48*, 157.

(7) Siegbahn PEM, A. f. J., Heiberg A, Roos BO *J. Chem. Phys.* **1981**, *74*, 2384.

(8) BO, R. *Adv. Chem. Phys.* **1987**, *69*, 399.

(9) Iwata, S. *Chemical Physics Letters* **1981**, *83*, 134.

(10) Knizia, G. *Journal of Chemical Theory and Computation* **2013**, *9*, 4834.

(11) Laikov, D. N. *International Journal of Quantum Chemistry* **2011**, *111*, 2851.

(12) Subotnik, J. E.; Dutoi, A. D.; Head-Gordon, M. *The Journal of Chemical Physics* **2005**, *123*, 114108.

(13) Chwee, T. S.; Carter, E. A. *The Journal of Chemical Physics* **2010**, *132*, 074104.

(14) Krisiloff, D. B.; Carter, E. A. *Physical Chemistry Chemical Physics* **2012**, *14*, 7710.

(15) Schmidt, M. W.; Ruedenberg, K. *The Journal of Chemical Physics* **1979**, *71*, 3951.

(16) Huzinaga, S.; Klobukowski, M. *Chem. Phys. Lett.* **1993**, *212*.

(17) Sansonetti, J. E.; Martin, W. C.; Young, S. L.; National Institute of Standards and Technology, Gaithersburg, MD: 2005.

(18) J.E. Sansonetti, W. C. M., and S.L. Young In *Handbook of Basic Atomic Spectroscopic Data* National Institute of Standards and Technology, Gaithersburg, MD: 2005; Vol. version 1.1.2.

(19) Schmidt, M. W.; Baldridge, K. K.; Boatz, J. A.; Elbert, S. T.; Gordon, M. S.; Jensen, J. H.; Koseki, S.; Matsunaga, N.; Nguyen, K. A.; Su, S. J.; Windus, T. L.; Dupuis, M. M., J. A. *J. Comput. Chem.* **1993**, *14*, 1347−1363.

(20) Gordon, M. S.; Schmidt, M. W. *Theory and Applications of Computational Chemistry: The First Forty Years*; Elsevier: The Netherlands, 2005.

(21) Bode, B. M.; Gordon, M. S. *J. Mol. Graphics Modell* **1998**, *16*, 133−138.

(22) Jacquemin, D.; Preat, J.; Wathelet, V.; Perpète, E. A. *The Journal of Chemical Physics* **2006**, *124*, 074104

(23) T.H. Dunning, J. *J. Chem. Phys.* **1989**, *90*.

(24) Haaland, A.; Lusztyk, J.; Novak, D. P.; Brunvoll, J.; Starowieyski, K. B. *Journal of the Chemical Society, Chemical Communications* **1974**, 54.

(25) Seibold, E. A.; Sutton, L. E. *The Journal of Chemical Physics* **1955**, *23*, 1967.

(26) Yamaguchi, Y.; Ding, W.; Sanderson, C. T.; Borden, M. L.; Morgan, M. J.; Kutal, C. *Coordination Chemistry Reviews* **2007**, *251*, 515.

(27) Becke, A. D. *J. Chem. Phys.* **1992**, *96*, 2155.

(28) Becke, A. D. *J. Chem. Phys.* **1993**, *98*, 5648.

(29) M.M. Francl, W. J. P., W.J. Hehre, J.S. Binkley, M.S. Gordon, D.J. DeFrees and J.A. Pople *J. Chem. Phys.* **1982**, *77*.

(30) V. Rassolov, J. A. P., M. Ratner and T.L. Windus, *J. Chem. Phys.* **1998**, *109*.

(31) Kaupp, M.; Schleyer, P. v. R.; Stoll, H.; Preuss, H. *J. Chem. Phys.* **1991**, *94*.

(32) Bergner, A.; Dolg, M.; Kuechle, W.; Stoll, H.; Preuss, H. *Mol. Phys.* **1993**, *80*.

(33) Balfour-Paul, J. *Indigo*; British Museum Press: London, 1998.

(34) Mulliken, R. S. *Chem Rev* **1947**, *41*, 207.

(35) Stitt, F. *The Journal of Chemical Physics* **1941**, *9*, 780.

(36) Stitt, F. *The Journal of Chemical Physics* **1940**, *8*, 981.

(37) Price, W. C. *The Journal of Chemical Physics* **1947**, *15*, 614.

(38) Jones, D. S.; Lipscomb, W. N. *The Journal of Chemical Physics* **1969**, *51*, 3133.

(39) Smith, H. W.; Lipscomb, W. N. *The Journal of Chemical Physics* **1965**, *43*, 1060.

(40) Sironi, M.; Raimondi, M.; Cooper, D. L.; Gerratt, J. *The Journal of Physical Chemistry* **1991**, *95*, 10617.

(41) Brundle, C. R.; Robin, M. B.; Basch, H.; Pinsky, M.; Bond, A. *Journal of the American Chemical Society* **1970**, *92*, 3863.

(42) Hamilton, W. C. *Proceedings of the Royal Society A: Mathematical, Physical and Engineering Sciences* **1956**, *235*, 395.

(43) Burnelle, L.; Kaufman, J. J. *The Journal of Chemical Physics* **1965**, *43*, 3540.

(44) Gimarc, B. M. *Journal of the American Chemical Society* **1973**, *95*, 1417.

(45) Foster, J. P.; Weinhold, F. *Journal of the American Chemical Society* **1980**, *102*, 7211.

(46) Mohr, R. R.; Lipscomb, W. N. *Inorganic Chemistry* **1986**, *25*, 1053.

(47) S. Huzinaga, e., J. Andzelm, M. Klobukowski, E. Radzio-Andzelm, Y. Sakai, H. Tatewaki In *Gaussian Basis Sets for Molecular Calculations*; Elsevier: Amsterdam, 1984.

(48) Kealy, T. J.; Pauson, P. L. *Nature* **1951**, *168*, 1039.

(49) Wilkinson, G.; Rosenblum, M.; Whiting, M. C.; Woodward, R. B. *Journal of the American Chemical Society* **1952**, *74*, 2125.

(50) Yamazaki, M. *The Journal of Chemical Physics* **1956**, *24*, 1260.

(51) Hull, E.; West, A.; Bakac, A.; Windus, T. *Unpublished*.

(52) Valiev, M.; Bylaska, E. J.; Govind, N.; Kowalski, K.; Straatsma, T. P.; Van Dam, H. J. J.; Wang, D.; Nieplocha, J.; Apra, E.; Windus, T. L.; de Jong, W. A. *Computer Physics Communications* **2010**, *181*, 1477.

(53) Dolg, M.; Stoll, H.; Preuss, H.; Pitzer, R. M. *J. Phys. Chem.* **1993**, *97*.

(54) Osanai, Y. O. U.; Sekiya, M.; Noro, T.; Koga, T. *Molecular Physics* **2003**, *101*, 65.

(55) Noro, T.; Sekiya, M.; Koga, T. *Theor Chem Acc* **1997**, *98*, 25.

(56) Koga, T.; Yamamoto, S.; Shimazaki, T.; Tatewaki, H. *Theor Chem Acc* **2002**, *108*, 41.

CHAPTER 6: CONCLUSIONS

Experiment and computation agree that the dissociation of complexes of the form $L(H_2O)MX^{2+}$, where L = [14]aneN_4 or *meso*-Me_6-[14]aneN_4, M = Rh or Co and X is CH_3, H or NO involve a significant ligand to metal charge transfer. As suspected by experimental observations, computations show that these transitions involve an M-X bonding to antibonding transition, while similar complexes where X is Cl or NO_2 show these transitions at much shorter wavelengths of light. Additional substitution of L with four ammonia groups and M=Co shows that the UV spectra lines are not significantly depending on the structure of the equatorial ligands although the use of nitrogen containing groups is essential for the transitions.

Reactions of gas phase Nb^+, Nb^{2+} with CO and CO_2 using flowing afterglow were observed and kinetic data was calculated. DFT, MCSCF and MRPT2 calculations were performed to better understand possible pathways and reaction mechanisms. Experiments reveal that the reaction of Nb^+ with CO is slow, inefficient and yields only $Nb(CO)^+$ products. DFT calculations show that higher order clusters are very stable and and suggest their experimental absence may have to do with the inefficiency of the collisional mechanism relative to the timescale of the experiment. Higher order clusters were observed for Nb^{2+}. Reactions are faster for the metal dication than for the metal monocation, but not significantly. Computationally, while formation for higher order complexes is favorable for both mono and dications, it is much more so for dications. The combination of a higher reaction rate and the higher exothermicity may may explain why higher order complexes were seen with the dication but not the monocation.

Reactions of Nb^+ and Nb^{2+} with CO_2 effectively activate the C-O bond, resulting in metal oxide formation. Reactions of the monocation were more efficient and the DFT calculated PES predicts a near thermoneutral activation energy and exothermic products, which supports the observed experimental efficiency. The dication, while activating the C-O bond, was much less efficient. MRPT2 calculations indicated a near thermoneutral transition state and only slightly exothermic products. The difference in the energies of the products could explain the differences in efficiency for the mono and dication. No charge transfer was observed in the dication reaction. The question of charge transfer deserves further investigation.

A flowing afterglow instrument was used to react Ta^{x+} with CO and CO_2. Kinetic data was calculated for the experimental information and DFT, MCSCF and MRPT2 calculations were performed to gain insight into the reaction processes. While DFT calculations predicted a complexation limit of $Ta(CO)_6^{x+}$, experimentally only Ta^{2+} reached that limit, and the mono complex was the only observed complexation product for Ta^+. The experimental absence of these higher order complex may be due, in part, to the relative collisional inefficiency of the monocation compared to the dication. It would be interesting to see if higher order $Ta(CO)_n^+$ where n>1 complexes exist in a cosmic experiment of more infinite timescale such as those that exist in interstellar clouds.

Both Ta^+ and Ta^{2+} showed a relatively efficient ability for activating the C-O bond in CO_2, and metal oxide products were observed in both cases. Charge transfer products were also observed for the dication reactions. DFT calculations on the monocation were confusing but MRPT2 calculations suggested a thermoneutral transition state and exothermic products which are in agreement with experimental results. DFT calculations on the dication similarly agree with the experiment, suggesting a very low barrier for reaction and exothermic products. Both

DFT and MRPT2 calculations predict a spin crossing exists in the PES leading from the reactants to the products. Charge transfer was explored with DFT in a very rudimentary way and no barrier for the formation of charge transfer products was suggested. More studies are needed to better understand the mechanism of the charge transfer reactions.

The QUAMBO algorithm previously devised and published[1-5] was tested on several different molecules and the model was extended to transition metals. The algorithm is now available in GAMESS[6,7] for molecules containing any atom up to xenon. The model provides insight into fundamental bonding interactions, including electron poor multi-centered bonding interactions including agostic interactions. In addition VVOS orbitals, by nature of generating the simple molecular orbital theory virtual orbital counterparts of the occupied space, are naturally suited for use in further calculations like MCSCF or CI. Higher order CI excitation calculation within the VVOS space (CISD or higher) can give a good estimate of the MCSCF energy at a fraction of the computational cost. The valence virtual orbitals are closer in character to the virtual orbitals of excited state method orbitals, like TD-HF, than canonical RHF virtual orbitals, giving qualitatively useful information on interactions without the expense of an excited state method. Further expansions of the QUAMBO method would involve making it compatible with ECP/MCP basis sets and relativistic basis sets.

Overall the process of researching and writing this dissertation was a fruitful one. Many insights were gained into the fundamentals of chemistry, especially transition chemistry. A vast field of knowledge into basis sets, the nature of chemical bonding, computational methods were opened. The process of gaining knowledge and new understanding, a skill finely tuned in the course of graduate study, is expected to continue for the foreseeable future.

References

(1) Lu, W. C.; Wang, C. Z.; Schmidt, M. W.; Bytautas, L.; Ho, K. M.; Ruedenberg, K. *The Journal of Chemical Physics* **2004**, *120*, 2638.

(2) Lu, W. C.; Wang, C. Z.; Schmidt, M. W.; Bytautas, L.; Ho, K. M.; Ruedenberg, K. *The Journal of Chemical Physics* **2004**, *120*, 2629.

(3) Ivanic, J.; Atchity, G.; Ruedenberg, K. *Theor Chem Acc* **2008**, *120*, 281.

(4) Ivanic, J.; Ruedenberg, K. *Theor Chem Acc* **2008**, *120*, 295.

(5) West, A. C.; Schmidt, M. W.; Gordon, M. S.; Ruedenberg, K. *The Journal of Chemical Physics* **2013**, *139*.

(6) Schmidt, M. W.; Baldridge, K. K.; Boatz, J. A.; Elbert, S. T.; Gordon, M. S.; Jensen, J. H.; Koseki, S.; Matsunaga, N.; Nguyen, K. A.; Su, S. J.; Windus, T. L.; Dupuis, M. M., J. A. *J. Comput. Chem.* **1993**, *14*, 1347−1363.

(7) Gordon, M. S.; Schmidt, M. W. *Theory and Applications of Computational Chemistry: The First Forty Years*; Elsevier: The Netherlands, 2005.